Palacký University Olomouc

Reaction Mechanisms in on-Surface Synthesis by Computational Chemistry Methods

Ph.D. thesis by

Mgr. Adam Matěj

2023

Department of Physical Chemistry
Faculty of Science
Palacký University Olomouc, Czech Republic

Declaration of the author:

I hereby declare that this thesis is a result of my own work, and all the used sources are duly cited. I furthermore declare that no part of this thesis has been used for obtaining another degree.

In Olomouc: …………………………   Handwritten signature: …………………………

Acknowledgment

My biggest thanks belong to my supervisor and mentor, Pavel Jelínek, who guided me through my Ph.D. degree, allowed me to work on interesting and challenging projects, and helped me to grow as a young scientist. With that, I would like to thank all my colleagues and friends at the Nanosurf lab at FZU AV CR, dept. of Physical Chemistry and also the RCPTM division.

I am forever grateful for the support from my love Ilona and my family for their love and support throughout my studies.

<div align="center">

Thank you!

</div>

Bibliographical identification:

Author	Mgr. Adam Matěj
Topic	Theoretical Study of Material Properties of Molecular Nanostructures on Surfaces of Solids
Title	Reaction Mechanisms in on-Surface Synthesis by Computational Chemistry Methods
Type of thesis	Dissertation
Department	Department of Physical Chemistry
Supervisor	doc. Ing. Pavel Jelínek, Ph.D.
Year	2023
Keywords	On-surface synthesis, quantum mechanics, molecular dynamics, adatom, surface, conjugation, reaction mechanism
Number of pages	85
Language	English

Abstract

On-surface synthesis has revolutionized the field of synthetic chemistry by enabling the synthesis and characterization of large, conjugated hydrocarbons that were previously inaccessible through conventional wet chemistry methods. This young physicochemical field takes advantage of the catalytic properties of metallic surfaces under an ultra-high vacuum environment to reduce the reaction space to two dimensions and introduce reactive metal adatoms, leading to novel and unexpected synthetic pathways. To fully utilize these synthetic routes, a deep understanding of the underlying reaction mechanisms is essential. In this thesis, we present the current state of on-surface synthesis and explore the application of computational chemistry methods in studying reaction mechanisms, directly connected to scanning probe microscopy experiments.

The thesis focuses on three main research projects that highlight the author's contributions to the field. Firstly, the influence of vibrational modes on reaction pathways is investigated. It is discovered that changes in π-conjugation can activate specific vibrations, facilitating certain reaction steps with similar energy barriers. Secondly, the interplay and cooperation of metallic adatoms from different elements are explored. Co-deposited sodium cations are found to increase the temperature threshold for precursor desorption, while noncovalent organometallic dimers catalyzed by silver adatoms promote one-dimensional polymerization with high regioselectivity. The dissociation process exhibits regioselective behavior consistent with experimental observations. Lastly, the combination of gold adatoms with an Ag(111) surface demonstrates regiospecific activation of aromatic C-H bonds at room temperature. The adatoms attack the edges of molecular self-assembly, forming organometallic dimers and resulting in high regioselectivity.

A comprehensive and reliable description of the studied properties and processes is achieved through the use of various theoretical methods, providing explanations for the experimentally observed products. By combining computational chemistry approaches with scanning probe microscopy experiments, this thesis contributes to understanding reaction mechanisms in on-surface synthesis. The findings enhance our knowledge of the field and pave the way for the design and synthesis of tailored conjugated hydrocarbons with desired properties.

Bibliografická identifikace:

Autor	Mgr. Adam Matěj
Téma	Teoretické studium materiálových vlastností molekulárních nanostruktur na površích pevných látek
Název	Reakční mechanismy v syntéze na površích pomocí metod výpočetní chemie
Typ práce	Disertační
Katedra	Katedra fyzikální chemie
Vedoucí	doc. Ing. Pavel Jelínek, Ph.D.
Rok	2023
Klíčová slova	Syntéza na povrchu, kvantová mechanika, molekulová dynamika, adatom, povrch, konjugace, reakční mechanismus
Počet stran	85
Jazyk	Angličtina

Abstrakt

Syntéza na površích způsobila revoluci v oblasti syntetické chemie tím, že umožňuje syntézu a charakterizaci velkých konjugovaných uhlovodíků, které byly dříve nedostupné konvenčními metodami chemie v roztoku. Tento mladý fyzikálně-chemický obor využívá katalytických vlastností kovových povrchů v prostředí ultravysokého vakua ke zmenšení reakčního prostoru do dvou rozměrů a zavedení reaktivních kovových adatomů, což vede k novým a nečekaným syntetickým cestám. Pro plné využití těchto syntetických cest je nezbytné hluboké pochopení základních reakčních mechanismů. V této práci představujeme současný stav syntézy na površích a zkoumáme využití metod výpočetní chemie při studiu reakčních mechanismů, přímo propojených s experimenty mikroskopie skenovací sondou.

Práce se zaměřuje na tři hlavní výzkumné projekty, které zdůrazňují autorův přínos v této oblasti. Za prvé je zkoumán vliv vibračních módů na reakční dráhy. Bylo zjištěno, že změny v π-konjugaci mohou aktivovat specifické vibrace, které usnadňují určité reakční kroky s podobnými energetickými bariérami. Za druhé je zkoumána souhra a spolupráce kovových adatomů různých prvků. Bylo zjištěno, že kodeponované sodíkové kationty zvyšují teplotní práh pro desorpci prekurzorů, zatímco nekovalentní organokovové dimery katalyzované adatomy stříbra podporují jednodimenzionální polymeraci s vysokou regioselektivitou. Proces disociace vykazuje regioselektivní chování v souladu s experimentálními pozorováními. A konečně, kombinace adatomů zlata s povrchem Ag(111) vykazuje regiospecifickou aktivaci aromatických C-H vazeb při pokojové teplotě. Adatomy napadají okraje molekulárního samouspořádání, vytvářejí organokovové dimery a vedou k vysoké regioselektivitě.

Komplexní a spolehlivý popis studovaných vlastností a procesů je dosažen pomocí různých teoretických metod, které poskytují vysvětlení pro experimentálně pozorované produkty. Kombinací přístupů výpočetní chemie s experimenty mikroskopie skenovací sondou přispívá tato práce k pochopení reakčních mechanismů při syntéze na povrchu. Získané poznatky rozšiřují naše znalosti v této oblasti a připravují půdu pro návrh a syntézu konjugovaných uhlovodíků s požadovanými vlastnostmi.

Table of Contents

List of Abbreviations

AFM	Atomic force microscopy
BDE	Bond dissociation energy
CASSCF	Complete active space, self-consistent field
DCA	Dicyanoanthracene
DFT	Density functional theory
FEP	Free energy profile
FF	Force field
FS	Final state
FT-DFT	Finite-temperature DFT
GGA	generalized gradient approximation
HAT	Hexaazatriphenylene
HF	Hartree-Fock
IM	Intermediate
IS	Initial state
LDA	Local density approximation
MD	Molecular dynamics
MM	Molecular mechanics
MO	Molecular orbital
NO	Natural orbital
OSS	On-surface synthesis
QM	Quantum mechanics
RT	Room temperature
SCF	Self-consistent field
SPM	Scanning probe microscopy
STM	Scanning tunneling microscopy
TS	Transition state
UHV	Ultra-high vacuum
vdW	van der Waals
WHAM	Weighted histogram analysis method
XC	Exchange-correlation

List of Publications

1.   Rascon, E. C. *et al.* On-Surface Synthesis of Square-Type Porphyrin Tetramers with Central Antiaromatic Cyclooctatetraene Moiety. *J. Am. Chem. Soc.* **145**, 967–977 (2023).

2.   Jiménez-Martín, A. *et al.* On-surface synthesis of non-benzenoid conjugated polymers by selective atomic rearrangement of ethynylarenes. *Chem. Sci.* **14**, 1403–1412 (2023).

3.   Lawrence, J. *et al.* Circumventing the stability problems of graphene nanoribbon zigzag edges. *Nat. Chem.* **14**, 1451–1458 (2022).

4.   Liu, X. *et al.* Exploiting Cooperative Catalysis for the On-Surface Synthesis of Linear Heteroaromatic Polymers via Selective C–H Activation. *Angew Chem Int Ed* **61**, (2022).
        (**Chapter 4.3.**)

5.   Zeng, Z. *et al.* Chemisorption-Induced Formation of Biphenylene Dimer on Ag(111). *J. Am. Chem. Soc.* **144**, 723–732 (2022).

6.   Lowe, B. *et al.* Selective Activation of Aromatic C–H Bonds Catalyzed by Single Gold Atoms at Room Temperature. *J. Am. Chem. Soc.* **144**, 21389–21397 (2022).
        (**Chapter 4.4.**)

7.   Biswas, K. *et al.* Interplay between π-Conjugation and Exchange Magnetism in One-Dimensional Porphyrinoid Polymers. *J. Am. Chem. Soc.* **144**, 12725–12731 (2022).

8.   Mallada, B. *et al.* On-Surface Strain-Driven Synthesis of Nonalternant Non-Benzenoid Aromatic Compounds Containing Four- to Eight-Membered Rings. *J. Am. Chem. Soc.* **143**, 14694–14702 (2021).

9.   Biswas, K. *et al.* On-Surface Synthesis of a Dicationic Diazahexabenzocoronene Derivative on the Au(111) Surface. *Angew Chem Int Ed* **60**, 25551–25556 (2021).

10.   Santhini, V. M. *et al.* 1D Coordination π–d Conjugated Polymers with Distinct Structures Defined by the Choice of the Transition Metal: Towards a New Class of Antiaromatic Macrocycles. *Angew. Chem. Int. Ed.* **60**, 439–445 (2021).

11.   De La Torre, B. *et al.* Tailoring π-conjugation and vibrational modes to steer on-surface synthesis of pentalene-bridged ladder polymers. *Nat Commun* **11**, 4567 (2020).
        (**Chapter 4.2.**)

List of Figures

1. Preface

Conjugated hydrocarbons constitute a rich playground for technological applications via modification of the electronic structure.[1-6] The possibility to tune the bandgap[7-9] from insulator to semiconductor or even a metal renders hydrocarbons suitable for nanoelectronics, solar energy conversion, and spintronics. In special cases, the molecules exhibit an open-shell electronic structure exhibiting π-magnetism.[10-12] These radical molecules are potentially applicable for data storage, catalysis, and solar cells. The research of conjugated molecules and nanomaterials, i.e., conjugated polymers, is an active and dynamic field with a shared objective of achieving tailored electronic structures. In this pursuit, computational chemistry emerges as an indispensable tool providing atomistic insight into the structure and a detailed description of the electronic structure. Theoretical calculations and simulations enable us to investigate chemical reactions and predict the properties of molecules and materials that have not yet been synthesized, expanding the boundaries of scientific knowledge and guiding experimental efforts. The interplay between computational chemistry and experimental research is crucial for advancing the field of conjugated molecules and nanomaterials. The insights gained from computational studies inform and guide experimental investigations, leading to the development of new materials with tailored electronic structures and enhanced performance.

Although the synthesis and characterization of conjugated hydrocarbons is the subject of mainly organic chemistry, there is one key issue impeding the preparation of larger hydrocarbons, solubility. In the case of conjugated nanomaterials such as one-dimensional polymers and nanoribbons, the desired properties emerge with increasing length,[7-9] which renders such materials inaccessible via conventional in-solution chemistry. One solution to the synthetic issue is offered by the on-surface synthesis (OSS) methodology. This innovative approach takes advantage of processes unique to surfaces and simultaneously circumvents solubility and stability issues by deposition under ultra-high vacuum (UHV) conditions.[13-16] This approach takes advantage of various effects inherent to OSS. Firstly, it resolves the solubility issue, enabling the growth of products into ribbons and chains that can reach dimensions of hundreds of nanometers.[17-20] Additionally, the molecular precursors can form non-covalent self-assemblies,[21,22] further expanding the potential for tailored structures and properties. The UHV conditions ensure the absence of side reactions of reactive intermediates or products with the atmosphere, solvents, or contaminants. This controlled environment allows for precise control over the reaction processes and eliminates unwanted interference. Moreover, the surfaces on which the OSS is performed play a crucial role in the process. The choice of surface, whether metallic, insulating, or featuring specific terminations, influences the interactions between the molecules and the substrate and dictates the nature and behavior of reactive adatoms during the reactions. Additionally, surfaces induce planarization of the molecular precursors, promoting the

formation of well-defined structures and enhancing the desired properties of the synthesized materials.

While the OSS can be coupled with various experimental analysis techniques, in this thesis we will focus on the field using scanning probe microscopy (SPM) instrumentation.[23,24] The atomically flat surfaces under UHV are an optimal playground for SPM which allows for accurate structural and electronic analyses with submolecular resolution.[25–27] Various operating modes are available, addressing the properties of interest. For conducting structural analysis of planar molecules with bond-resolving precision, we use atomic force microscopy (AFM). This technique allows for the visualization of the surface topography and can provide atomic-scale details of the molecular structure. By precisely scanning the probe tip across the surface, AFM generates high-resolution images that reveal the arrangement and spatial relationships of the atoms within the molecules. On the other hand, scanning tunneling microscopy (STM) is used when we require information about the electronic structure of the probed molecule. Within this measurement, we can visualize a real-space distribution of voltage-dependent tunneling current intensity, which is proportional to the density of states at the probed region of the molecule. By measuring the current flowing between the sharp probe tip and the surface, STM offers insights into the electronic properties of the molecules, such as the distribution of electronic orbitals and energy levels.

One significant advantage of utilizing AFM and STM techniques in conjunction with OSS is the ability to compare experimental images with theoretical simulations. Through theoretical calculations based on optimized molecular structures and calculated electron density, we can generate simulated images that closely resemble the experimental results.[28,29] This direct comparison between experimental and simulated images serves as a straightforward evaluation of the theoretical model, allowing for validation and refinement of the computational methods employed.

By combining experimental observations obtained through SPM with theoretical simulations, we can gain a comprehensive understanding of the structural and electronic properties of the synthesized materials. This integrated approach enhances the accuracy and reliability of the results, providing valuable insights into the relationship between molecular structure and function. Through the careful analysis and comparison of experimental and simulated data, we can refine our theoretical models and optimize the design and synthesis of conjugated hydrocarbons and nanomaterials with desired properties and functionalities.

Computational chemistry has become an integral component of numerous chemical disciplines, including material science and nanomaterial chemistry, complementing the efforts of experimentalists. In this thesis, we aim to provide a comprehensive understanding of the theoretical methods employed in our research, as well as the specific techniques utilized for calculations,

simulations, and various analyses. The field of OSS, particularly within the SPM community, heavily relies on theoretical calculations to gain deeper insights into the electronic structure and the underlying processes that occur between experimental measurements, particularly at elevated temperatures. Theoretical calculations serve as a valuable tool to elucidate the intricate details of the molecular systems under investigation and provide a more comprehensive understanding of their behavior.

In the following two chapters, we will focus on the theoretical background of the calculations employed, elucidating the principles, methodologies, and limitations associated with these computational approaches. We will explore how these methods contribute to the description of the systems under study, allowing us to make informed interpretations and predictions. Furthermore, we will emphasize the crucial aspect of comparing theoretical results with experimental data, as this provides validation for the theoretical models employed and strengthens the reliability of the findings. Through this integrated theoretical-experimental approach, we aim to validate our theoretical models by comparing the predictions with experimental observations. The agreement between theory and experiment enhances our confidence in the reliability and accuracy of the theoretical methods employed. It also serves as a solid foundation for drawing meaningful conclusions and expanding our knowledge in the field of on-surface synthesis.

Chapter 4 focuses on the research projects, each including an introduction to the project, the role of the author within the project, and his contribution to the presented results. Copies of the publications are then included at the end of the subchapters. This chapter focuses on the on-surface synthesis protocols, the importance of computational chemistry in elucidating reaction mechanisms, and the complexity of such studies. The role of the surface, as well as adatoms, is discussed, and possible limitations of used calculations are presented.

The conclusion of the author's research presented in this thesis, together with the contribution to the knowledge is presented in Chapter 5. A concise and brief overview is given, and special attention is paid to the novelty and limitations of the presented research. An outlook on the scientific future of the author as well as the direction of OSS research is presented in the 7th chapter. Then a complete list of used literature follows, stating all sources used during the research and writing of this thesis. The author's publication list is included above, highlighting the scientific achievements during his starting career. The closing chapter includes a short summary of the author's broad scientific focus, achievements, and training.

2. Computational chemistry methods

Computational chemistry is a rapidly growing field that has revolutionized the way we approach chemistry and physics. It involves the use of physical models interpreted by mathematical apparatus and computational techniques to simulate chemical and physical phenomena. These computational methods have become increasingly important in physicochemical fields as they allow us to study complex systems that would often be impossible to investigate experimentally. Furthermore, computational chemistry methods have become more accessible due to advances in computer science, which has enabled us to tackle problems that were previously beyond the reach of traditional experimental methods. As a result, computational chemistry has become an essential tool for scientists in fields such as materials science, drug discovery, and catalysis. The choice of computational chemistry method depends on various factors, such as the size of the system, the property of interest, and the level of accuracy required. For small molecules and accurate electronic structure calculations, quantum mechanics-based methods can be employed but less computationally demanding methods are required for large systems of hundreds and thousands of atoms. Quantum chemistry methods from the post-Hartree-Fock (HF) family, such as configuration interaction, complete active space self-consistent field (CASSCF), and coupled cluster are commonly used. However, these methods are computationally expensive and are limited to small systems. For larger systems, density functional theory (DFT) is often used. DFT is a more efficient approach that calculates the electronic structure of molecules by integrating the electron density rather than explicitly solving the wave function. DFT is widely used for studying large systems and is particularly useful for calculating molecular geometries, vibrational frequencies, and spectroscopic properties. Beyond the size limits of quantum mechanical (QM) methods, calculations based on classical physics can be employed to study certain properties of interest. Molecular mechanics (MM) is a method that models the motion and interactions of atoms and molecules by classical physics. The use of classical physical equations in comparison to QM allows for studying large systems. Due to the design of the terms in MM, this method cannot describe bond breaking and is thus not suitable for studying chemical reactions. In some cases, a hybrid approach that combines both quantum and classical mechanics is used. This approach, known as QM/MM (quantum mechanics/molecular mechanics), allows for studying complex chemical systems such as enzymatic reactions. While the more precise QM part describes the core of the problem, e.g., a chemical reaction or a molecular spectrum, the MM part generates the surrounding environment to account for its influence on the conformation and/or electrostatics of the QM part. Finally, molecular dynamics (MD) simulations can be used to study the motion and behavior of molecules over time. This approach is commonly used to study the dynamics of large biological molecules and materials. Ultimately, the choice of computational method depends on the specific system and property of interest, as well as the computational resources available. It is often necessary to use a combination of methods to gain

enough information for a correct description of the studied system. This work describes the author's research employing various methods, which will be briefly described in the following subchapters.

2.1. Density Functional Theory

During the 20th century, there were numerous groundbreaking achievements in science. The ones that are directly linked to this work are the development of quantum mechanics, a remarkable technological advancement in computers, and the development of DFT. Now with the proper theory and methodology, we can model, study, and describe systems from atoms to nanomaterials with atomistic insight and high accuracy.

This great success of DFT is built on Hohenberg and Kohn's theorems,[30] a series of approximations, and the feasibility of numerical solving.[31,32] Starting from the basics, the first theorem states that the electron density determines the wavefunction uniquely and, therefore can be calculated in the place of the complex wavefunction. This means a significant speed-up since the electron density depends on only three spatial coordinates, while the wavefunction is a function of $3N$ with N electrons. The second theorem shows that the ground state electron density minimizes the total energy. This fact allows for numerical solving of the total electron density through the variational principle.

At this point, the basics of DFT are still a many-body problem with a limitation to a small number of electrons. The important approximation that allowed DFT to become the workhorse of computational chemistry was presented by Kohn and Sham.[33] They introduced the Kohn-Sham equations (eq. 1 and 2), which reduce the many-body problem to a set of non-interacting one-electron functions, represented by one-electron orbitals (Kohn-Sham orbitals).[34]

$$F_{KS}\varphi_i = \varepsilon_i\varphi_i \tag{1}$$

$$F_{KS} = -\frac{1}{2}\Delta_i + V_S(r) \tag{2}$$

Here, F_{KS} is the Kohn-Sham functional, φ_i are the one-electron orbitals, and V_S is the effective potential of the system. In such form, each electron is treated separately as it interacts with an effective average electron density. By optimizing the Kohn-Sham orbitals and applying the Kohn-Sham functional with known V_S, we obtain the ground state electron density and energy. The problem lies in the form of the effective potential.

Through a series of expressions of total energy contributions and beneficial separations, the following form for the total electronic energy is given:

$$E[\rho(r)] = T_S[\rho] + J[\rho] + E_{Ne}[\rho] + E_{XC}[\rho] \qquad (3)$$

The terms describing the kinetic energy (T_S), Coulomb's interaction between electrons (J), and interaction between electrons and nuclei (E_{Ne}) are known and easily calculated. The last term, E_{XC} is the energy component defined by the so-called exchange-correlation (XC) functional (V_{XC}), and its form is unknown. The electrons interact with the nuclei at a given geometry via Coulomb's interaction and this part of the potential energy is system dependent. Other parts of the total energy are system independent and as such are generally applicable to every system. These system-independent contributions include the electron-electron interactions and the kinetic energy of electrons. A classical part of the electron-electron interaction is described again by Coulomb's interaction, but the missing non-classical part has an unknown form. After calculating the exact kinetic energy of the non-interacting system, there are two missing terms from the independent total energy terms. Since they are unknown, the missing part is approximated by using the exchange-correlation functional in eq. 3, which aims at restoring most of the missing energy. After expressing the terms in eq. 3 and their derivation, we obtain a form of the V_S (see eq. 4), which we can insert into equation 2, and with the one-electron orbitals, we obtain the total energy.

$$V_S(r) = \int \frac{\rho(r_2)}{r_{12}} dr_2 + V_{XC}(r_1) - \sum_A^M \frac{Z_A}{r_{1A}} \qquad (4)$$

We see that V_S depends on the electron density and so depends on the orbitals. Therefore, the solution can be found only iteratively.

The numerical process of finding the ground state electron density starts with a trial density which is generated by different approaches from some initial set of orbitals. It can be for example a set of atomic orbitals on individual atoms or a precalculated initial set of molecular orbitals (MOs). The MOs are obtained by a linear combination of atomic orbitals, represented by basis functions in a basis set. During the iterative solution of the total electron density, the linear combination of all basis functions is adjusted via expansion coefficients to minimize the total energy of a system. Therefore, the size of the basis set strongly influences the precision but also the calculation time.

There is a plethora of variations in the form of the exchange-correlation functional. On the ladder of complexity (accuracy) exist various approximations to the V_{XC}, namely local density approximation (LDA), generalized gradient approximation (GGA), meta-GGA, hybrid functionals using a fraction of exact exchange from HF, and more. Within each of these families of functionals, there are numerous individual functionals, that were developed by different groups and for various systems. It is always important to use a suitable functional for a given problem for accurate and reliable results. Throughout this research, we employed a few different functionals, which will be

named in Chapter 3.5. together with their use in specific investigations. They belong to families of GGA, hybrids, and range-separated hybrids.

GGA functionals improve the treatment of the missing correlation energy with respect to LDA by taking into account also the gradient of the charge density, not only the density at a given point.[35] GGA functionals describe molecules sufficiently well, becoming the workhorse within DFT. Often within GGA, the functional form was separated into correlation and exchange parts, which are then developed individually. Further improvements were introduced by combining the GGA functionals with a fraction of an exact exchange obtained from a HF calculation.[36,37] This approximation to V_{XC} is called hybrid functional. It was found that a fruitful cancelation of errors is present in the various F_{XC} and that the inclusion of 100 % of the exact exchange instead of the approximate one from GGA worsens the results.[38,39] For that reason, only a fraction of Hartree-Fock's exchange, usually between 10 and 50 %, is added to the DFT. A third approximation used in this work is termed range-separated hybrid.[40] It is an expansion of the previously described hybrid functionals, with range-separated spatial regimes in which a mixture of the approximate and exact exchange contribution varies.

2.2. Molecular Mechanics

Classical physics based on Newtonian equations is not only easily understood thanks to our everyday perception but also easily defined and evaluated in molecular systems. This reason makes MM computationally very efficient and allows us to study large systems of thousands of atoms, such as proteins, nucleic acids, and biological membranes. The set of equations describing various potentials is defined by so-called force fields (FF) and each potential is described by a discrete term. The evaluation of all included terms yields the total potential energy of the system in each molecular structure. Various types of FF were developed for specific uses, e.g., for nucleic acids, proteins, lipids, solid interfaces, and many others.

$$E_{total} = \sum_{bonds} K_r (r - r_0)^2 + \sum_{angles} K_\theta (\theta - \theta_0)^2$$
$$+ \sum_{dihedrals} \frac{V_n}{2} [1 + \cos(n\emptyset - \gamma)] + \sum_{i<j} \left[\frac{A_{ij}}{R_{ij}^{12}} - \frac{B_{ij}}{R_{ij}^6} + \frac{q_i q_j}{\epsilon R_{ij}} \right]$$

$$(5)$$

Each FF then differs in the potential terms and various parameters for different atom types. Equation 5 shows the simple Amber force field,[41] consisting of three bonding and two nonbonding terms. Firstly, let us briefly describe the FF terms. The construction of the FF via the potential functions is aimed at the description of important and easily evaluated interactions between individual atoms. First, there is a bonding term that has a harmonic oscillator form that defines the potential energy of all covalently bound atoms. Two parameters are needed for this term, the

equilibrium distance between the two atoms and the spring constant. The next terms define the potential energy of angles and torsions. These terms depend on three and four atomic centers, respectively, and as such define the potential energy with respect to hybridization, molecular orbital overlaps, and twists along bonds. Non-bonding terms describe weak non-covalent interactions, i.e., van der Waals (vdW) interactions and stronger electrostatics. Both terms iterate over all pairs of atoms (unless a cutoff range is defined), and evaluate the potential energy based on the atomic distance, well-depth and equilibrium distance. The general progress of the vdW term in the Lennard-Jones form is illustrated in Figure 1. The last-mentioned term describes electrostatics and is derived from Coulomb's law, depending on the two atomic charges and their distance. Various other terms may be included to describe missing interactions, but this brief description is sufficient for the methodology used herein, as we will show in later chapters.
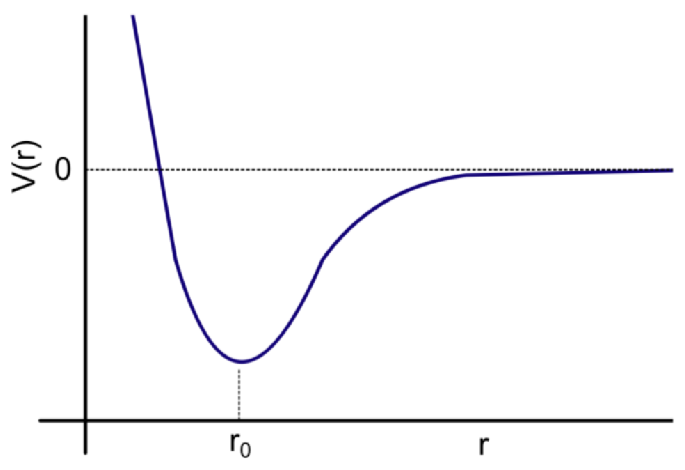

Figure 1: Lennard-Jones potential of the van der Waals interaction between two atoms with the equilibrium distance at r_0.

As mentioned above, FFs are defined not only by the potential terms but also by a set of parameters that enter these functions. For a specific FF, each atom has its atom type defined based on its chemical surroundings, giving rise to certain properties in connection to the defined terms. Then for each potential term, there is a set of parameters that defines the equilibrium properties of all the possible combinations in the defined system. That is, for bonding term, there will be all possible pairs of atom types present in the system and so on. The file that contains all these parameters for the molecular system in each calculation is called the topology file. The topology file is irrespective of the structural changes, it is defined for an initial structure and stays fixed throughout the whole calculation. Therefore, MM is unable to describe chemical changes throughout reactions.

2.3. QM/MM

The two computational methods described in previous chapters, DFT and MM, illustrate the two poles of underlying physics that describe the chemical properties. In some cases, it is beneficial to use their combination in a single calculation,[42] i.e., combine quantum mechanics with high accuracy on the small area of interest, and molecular mechanics to simulate an environment, or QM/MM for short. This methodology is commonly used for many various cases, be it molecules in a solvent, active sites in enzymes, and in our case, molecules on surfaces. QM/MM is an important method for our study of reaction mechanisms and the electronic structure of conjugated molecules, as it allows us to simulate a flat substrate for molecules without the need for expensive DFT calculations on hundreds and thousands of heavy atoms. The studied system is divided into layers, and each layer is described by different levels of theory (see Figure 2).
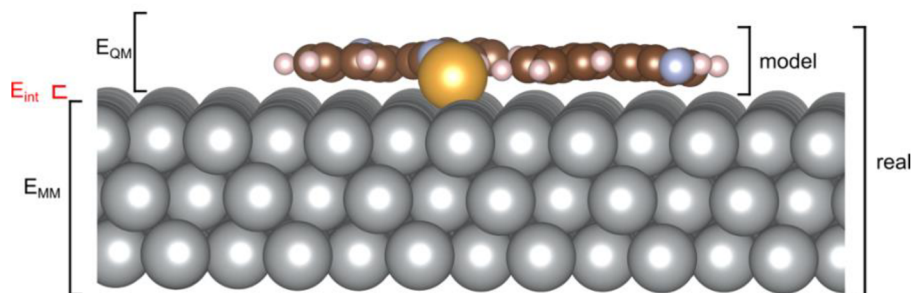

Figure 2: Illustration of QM/MM partitions in a real system. Left-hand side partitions correspond to the additive scheme with three terms evaluating corresponding energy values. The partition on the right illustrates the subtractive scheme.

The QM/MM method comes in two flavors, additive and subtractive (extrapolative) schemes. The first one defines total energy as the addition of three energy terms: the energy of the MM part (E_{MM}), the energy of the QM part (E_{QM}), and their interactions ($E_{MM\text{-}QM}$) (see Equation 6).

$$E_{tot} = E_{MM} + E_{QM} + E_{MM-QM} \tag{6}$$

The layer in the MM region is the environment (surface) and the total energy of this layer is calculated with the chosen FF and parameters from the topology. The second layer, the QM part, is evaluated using our DFT method of choice. In the additive scheme, the interactions between the two layers are the tricky part but with only non-covalent interactions is simple to define. The second scheme is called subtractive or sometimes extrapolative. It takes a simpler approach to the total energy evaluation. The system is still divided into two layers (can be more, but we keep two for simplicity), the real system and the model, which is the smaller part of interest. Equation 7 shows the energy decomposition:

$$E_{tot} = E_{real}^{MM} + E_{model}^{QM} - E_{model}^{MM} \qquad (7)$$

In this scheme, we still have the high-level calculation on the model system as previously, but the MM calculations are now two and differ. First, a calculation of the real system with all atoms calculates the MM energy of the low layer (surface) and the interactions between the layers. The second MM calculation is carried out only for the model system and subtracted from the other two energies. This ensures the omission of the MM energy on the model and thus double evaluation. This scheme is easier to implement since the MM-QM interactions are solved solely within the chosen FF.

In our case, we describe the molecules using DFT, and we model the surfaces using MM. Since we work with homogeneous metallic substrates, we neglect the partial charges in the MM region, and the only interactions are described by vdW. In the case of adatoms, these are included in the QM partition. In some instances, the isolated adatom in the QM region shows incorrect properties, and a wider QM region, including several metal atoms in the surface layer, must be used.

2.4. Molecular Dynamics

In order to be able to simulate the studied system as it evolves in time at a certain temperature, we carry out MD calculations. Like MM, this method is based on Newton's equations of motion from classical physics. The most important parameter which we must define for each MD simulation is the time step, which must be short enough to capture the fastest motion in the system. For the duration of the chosen time step, the atoms are acted upon with forces calculated from MM or QM. Due to the continuous force, we obtain the velocity of each atom in each time window and the acceleration. The initial velocities of the starting structure are randomly assigned by Maxwell-Boltzmann distribution depending on the temperature of the simulation.

In our work, we carried out MD simulations for the description of the behavior of the studied molecules at the experimental conditions, namely on-surface reactions at elevated temperatures. During the evolution at the final temperature, the molecular system explores the conformational space of accessible states but a spontaneous transition across the reaction barrier is unlikely. This process happening during the simulation of one molecule has such a low probability that it is called a rare event. For us to observe these changes, we need to apply a suitable methodology and push the system across the barrier. There are various methods how to achieve this. Herein we will discuss the method called umbrella sampling (see Chapter 3.4.), which can describe the process along a defined reaction coordinate, and what is more, the results can be interpreted as free energy profiles, which bare a high experimental significance.

3. Reaction Mechanisms - Theory

In the previous chapter, we introduced the employed methods of computational chemistry, laying the foundation for the current chapter, where we will focus on the physicochemical properties and connection of the calculations with experiments that we can study using the abovementioned methods. First, we will focus on the comprehensive study of reaction mechanisms, the information obtained from experiments, the systematic procedure, and finally specific techniques with details of the calculations themselves. Then, we will introduce the technical information about the calculations, such as quantum chemistry codes, concrete force fields, exchange-correlation functionals, and so on.

Understanding the mechanisms by which reactions occur is crucial for advancing fields such as organic chemistry, biochemistry, and materials science. By deciphering the underlying molecular interactions, we can unlock the potential for developing novel compounds and controlling chemical processes. Within the context of OSS using SPM techniques, chemical reactions can be driven by temperature and light or be induced by the SPM tip by applying voltage bias between the tip and the surface. Herein we will describe the theoretical methods used for studying the reaction mechanisms of thermally driven reactions.

In the subsequent sections, we will provide detailed descriptions of the theoretical methods utilized in our study of reaction mechanisms. This includes a listing of utilized quantum chemistry codes, force fields, exchange-correlation functionals, and other technical aspects relevant to our calculations. Herein, we aim to establish a comprehensive understanding of the computational tools and methodologies that enable us to explore and comprehend the intricacies of chemical reactions.

3.1. Bond dissociation energy

In the initial phase of every investigation, it is optimal to carry out quick and simple analyses to obtain the first information about the studied problem. Often this original inquiry will give a hint on how to proceed in the next steps with more time and/or resource-demanding techniques. In computational chemistry, studying changes in properties before and during chemical reactions, the first analysis that comes to mind is the evaluation of bond dissociation energy (BDE). BDE simply quantifies the bond energy of investigated chemical bonds, both covalent and non-covalent. As such, the calculations consist of three separate jobs, which are simple and quick, depending on the size of the system and the method used.

In the case of dissociation, the first calculation is a relaxation of the initial state molecule, and the obtained total energy can be noted as E_A. After that, two other calculations are needed, specifically relaxations of the created fragments following the dissociation step. The two obtained energies will

then be E_B and E_C. With these energies obtained at a sufficient level of theory, the simple evaluation of BDE is obtained through equation 8:

$$BDE = E_B + E_C - E_A \qquad (8)$$

This simple evaluation of various bond energies can show an initial trend in regioselectivity. In the sense of comparison within a system, the BDEs of different bonds, e.g., C-H bond dissociation, with the same reference (B and C fragments) can be directly compared for trends. Once we are interested in the energetics during the reaction, the references to B and C fragments play a significant role. Gas-phase calculations would neglect any stabilizing interactions of the reactive species and thus, the energetic profile would be greatly overestimated. It is important to note here, that such calculations only compare energies of the stable states along the reaction path, i.e., minima on the energy profile. As such, we obtain no information about the energy barrier along the investigated reaction pathway.

It is possible to increase the accuracy and relatability of the calculated energies with experiments by calculating the vibrational modes of each molecular fragment (A-C) and obtaining total enthalpies (*H*) instead of energies through thermal corrections. Although in our experience, the differences between *E* and *H* in these primary analyses are marginal.

3.2. Biradical character

Another quick description of the electronic structure connected to reactivity along the reaction pathway is available with the analysis of biradical character. While open-shell molecules are highly reactive due to their singly occupied orbitals, the case of closed-shell molecules is not so straightforward. In a perfect closed-shell system, each valence orbital is exactly doubly occupied, and each virtual orbital is thus empty. In the real world, the situation changes. The occupation numbers vary from exactly 0 and 2 due to either the thermal occupation of higher electronic states or the multireference character of the ground state wavefunction. Therefore, we see that we can define a range for biradical character, where 0 means a perfect closed-shell system, and 1 means a perfect diradical, with two exactly singly occupied orbitals. This relationship can be evaluated by a well-known Yamaguchi formula, which quantifies the amount of open-shell character of the frontier natural orbitals (NOs).[43]

$$y_i = 1 - \frac{2T_i}{1 + T_i^2} \qquad (9)$$

$$T_i = \frac{n_{HONO-i} - n_{LUNO+i}}{2} \qquad (10)$$

In eq. 10, n stand for occupation numbers of respective NOs specified in subscripts. The natural occupation numbers are accessible from a DFT calculation after transforming the canonical MOs into NOs. Due to the simplicity of this method, it can be applied to high-level calculations such as CASSCF and other multireference methods.

The biradical character is a quick measure of the "openness" of the electronic structure with respect to the frontier orbitals. On one hand, we obtain a number that defines the molecule on the merits of unpaired electron density without giving further information about this density difference. On the other hand, we can visually analyze the frontier orbitals and judge by their occupation numbers the approximate effect of the induced biradical character. For example, with HOMO being a bonding orbital on a bond of interest and LUMO being the corresponding antibonding orbital, then the higher the biradical character is, the weaker the bond will be. Nonetheless, this indirect analysis is tedious in larger systems with highly delocalized orbitals.

A method developed directly for this purpose called finite temperature DFT (FT-DFT) uses a method of thermal smearing of electron occupation to obtain fractional orbital occupations.[44] The difference here is, that the calculation is not suitable for the evaluation of y_0, but for an integration of the unpaired electron density and plotting of its spatial distribution. What one gets from this calculation is the effective number of unpaired electrons and the real-space distribution of this unpaired density. This cost-effective calculation can be presented either stand-alone with the integrated unpaired electron density and its real space imaging or together with Yamaguchi's measure of biradical character. The plotting of the real-space unpaired electron density quickly shows which part of the molecule is the most affected by the mixing of the frontier orbitals. Figure 3 shows the plots of the fractional electron density of anthracene, pentacene, and triangulene, and one can easily see the middle rings in linear acenes bearing the largest unpaired electron density.
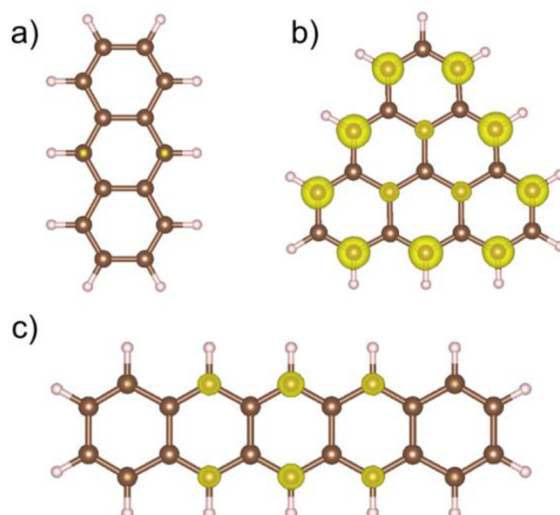
Figure 3: Plots of integrated fractional occupation density for anthracene (a), triangulene (b), and pentacene (c). Isosurface level is 0.005 a.u.

As mentioned above, y_0 can be easily calculated on various computational methods regardless of the QM program used. The FT-DFT on the other hand is implemented in only some codes, from which Orca was used during this work. For the calculation itself, one DFT job is required, assuming we already have a relaxed structure at an appropriate level of theory. During this job, one must include a keyword telling the program to enter the FT-DFT routine after the SCF cycle has converged and the temperature for the electronic smearing. The temperature is not chosen by the theoretician, as a relationship between the temperature and the XC functional was established by the authors of the method. The established dependence for reliable and comparable results is given in eq. 11,

$$T_{el} = 20{,}000\ K \times a_x + 5{,}000\ K \tag{11}$$

where T_{el} is the electronic temperature in K, and a_x is the exact HF exchange in the used functional. One can see from this relation that a wide range of DFT methods can be used, except for range-separated hybrid functionals, for which there is no formula developed. In the end, this is not necessarily a problem, as the FT-DFT method with the T_{el} defined in eq. 11 gives qualitatively similar results regardless of the employed functional. An important note is that the compared functionals must give qualitatively similar solutions to the MOs.

3.3. Transition state

The previous subchapters described a few options on how to gather initial information about the investigated system in the context of reactivity and energetics related to the initial state. Once we gather the information, we are faced with a decision on how to proceed further. Either way, if the primary investigation resulted in successful differentiation of reaction steps or not, the following calculations should focus on energetics along possible reaction pathways with a focus on reaction

16

barriers. The advantage of at least rough differences from BDE or radical character calculations makes the search for relevant reaction pathways more efficient.

In this chapter, we will discuss the methods of locating transition states (TS) along defined reaction steps. Reiterating back to the beginning, the information from experiments includes the initial state (IS), the product, a.k.a. final state (FS), and the reaction conditions. Based on the number of possible elementary steps connecting the IS with the FS the number of possible reaction pathways rises quickly. By obtaining BDE and the total energies of all the intermediates, we can form a complete picture of energy profiles along all pathways. But as mentioned above, these profiles lack any information regarding the reaction barriers. For this purpose, we want to locate the TS connecting two intermediate states (IM) and obtain the total energy at the saddle point. This task is often easier said than done and the success of these calculations strongly depends on our ability to define and predict the changes from IS to IM_1 and so on. There exist various options for how to relax the structure toward the first-order saddle point instead of the local minimum. First, as we mentioned here, the TS is a saddle point, to be precise, a first-order saddle point on the many-dimensional potential energy surface. This means that on a two-dimensional surface (variation of two bond lengths, for example), the TS will be a point at which the first derivation of energy is zero, and the system has exactly one imaginary vibration mode. Along this vibration, the energy of the system lowers, while along with any other vibration, the energy rises. The imaginary harmonic vibration is such that it moves the molecular structure to reactants and products, depending on the phase of the vibration. It is the difference from an equilibrium molecular structure in a local minimum, where every vibrational mode leads to an increase in energy.

From a practical point of view, various algorithms for relaxation toward the TS exist, yet the main challenge persists in the design of the calculation and the insight into the reaction by the theoretician. It is apparent that the calculation with a task to find a TS cannot start from an ambiguous molecular structure in its local minimum. There would be no guarantee that the algorithm follows the desired TS toward the relevant chemical change. Therefore, an approximate TS must be provided as the starting geometry. This task is the key input and the experience and chemical intuition of the investigator are the deciding factors for the success of the calculation.

Once TS was located and verified by frequency calculation for an imaginary vibration, the total energy of the TS can be plotted in the energy profile graph. This is our first attempt to describe the kinetics of a reaction by analyzing the reaction barriers along the studied pathways. The obtained energy is an important improvement, yet very crude and lacks a direct connection to experimental data. The total energies obtained from QM calculations are at 0 K and do not include any thermodynamical corrections. For this reason, the only valid practice is to locate TS along various reaction steps and compare the energy profiles along competing reaction pathways.

In our cases, we are mostly interested in intra- or intermolecular reactions involving cyclodehydrogenation steps. It is important to realize the limitations and advantages of the OSS conditions. On the one hand, the substrate induces planarization in molecules that would seek 3D conformation in gas-phase (or solution) to minimize the steric hindrance. The reactions are thus constrained to mostly only two dimensions, with exceptions being certain out-of-plane distortions and the aforementioned planarization. This quasi-2D reaction space can lead to structurally similar conformers leading to different TS along one reaction step. An example of this may be the dissociation of hydrogen on a gold adatom, where two TS were found with different barrier heights. One is where the C-H bond distorts out-of-plane above the adatom, and the H atom binds to the catalyst from above. In the second, the C-H distorts in-plane and the H atom binds to the adatom from the side.

3.4. Umbrella sampling

The aforementioned methods are static and describe various properties offering a basic insight into the chemical behavior of the system under investigation, but unfortunately, they lack direct connectivity to experimental observations. For this reason, we expanded our portfolio of theoretical methods with molecular dynamics simulations. By letting the prepared system, be it reactants, evolve in time at some final temperature with MD, the molecular structure will sample the conformational space accessible at a given temperature. Our calculations are unfortunately limited by the duration of such simulations and also memory requirements and therefore, we are able to study only relatively short time periods. During this short simulation, it is highly improbable that the reactants will undergo chemical changes even if thermally accessible during the simulation. Processes with a significant barrier along the energy profile are called rare events and for us to obtain the sampling during the reaction itself, we need to carry out simulations designed for rare events MD.

One such methodology is called umbrella sampling. In this type of simulation, we need to precisely define our reaction coordinate, ζ, along which we will perform the analysis. Along this chosen reaction coordinate, e.g., bond length, we will create windows for separate simulations in which we apply a harmonic bias potential (see Figure 4). The potential will be centered at the window position with a force constant large enough to overcome the expected (predicted) rare event but small enough to allow for conformational sampling around the minimum of the potential. By applying this harmonic potential in each window of the defined ζ, we enforce the sampling of the available space along the defined reaction path. It is expected that the procedure of choosing the force constant k and the spacing between windows will not be universal for different processes. They are tightly connected and there exist requirements that must be met for the simulations to be correct. First, the k must be higher than the energy barrier, which the system must overcome during the simulation. Second, the overlap of sampling between windows must be sufficient and the whole reaction coordinate must be

18

properly sampled. This is checked by plotting the histogram of sampled distances (depends on the definition of ζ, can also be angles, etc.) in each window and their overlap is controlled. It is clear that too high k will make sampling of values further from the center of the bias potential much more difficult, and the overlap will be poor. Therefore, the window spacing is dependent on the chosen k. It is worth noting that the window spacing and k do not have to be uniform along the ζ, they can differ around the critical points, especially the TS. Around the TS, high distortive forces are pushing the system away from the TS and it can be challenging to sample the space around this value properly. If this is encountered, additional windows with a higher k can be added for better sampling around this point on the ζ. On the other hand, in a rather shallow area of the ζ, the k can be small and fewer windows may be required for a sufficient sampling of the available space, although a longer simulation time may be required. All this comes down to a tradeoff between the number of separate simulations and the simulation time. Once all simulations are performed, data collected and overlaps checked, we can move further for the analysis itself.
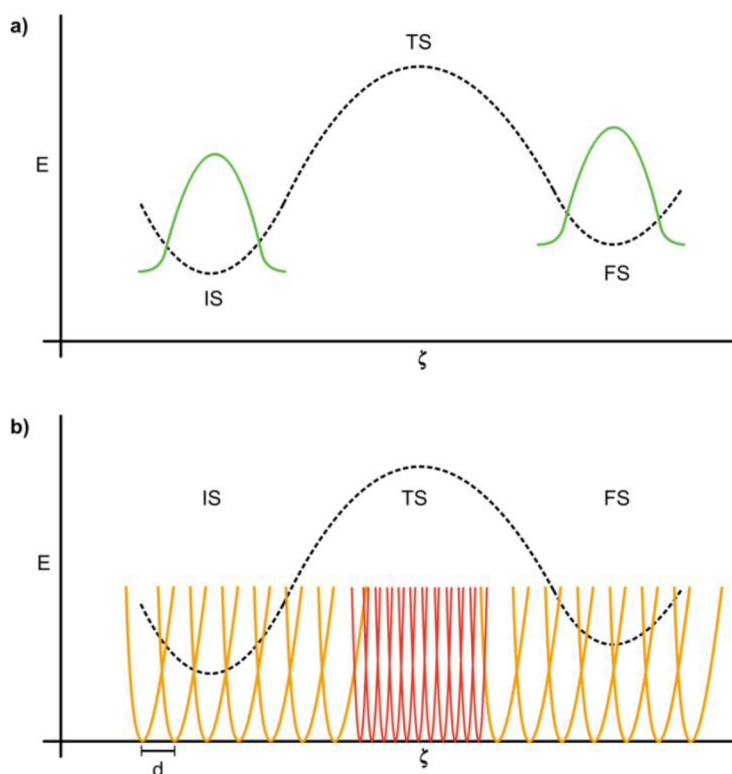

Figure 4: Illustration of the umbrella sampling method. The graphs represent energy profiles (black dashed curve) along a reaction coordinate ζ. (a) a sampling of free MD is marked by green curves, illustrating the inability to sample along the whole reaction coordinate. (b) parabolas illustrate the harmonic bias potential applied in each window and the higher the force constant k, the narrower the parabola. Spacing between windows is also highlighted as d. Red parabolas have tighter potential around the transition state to sample this region sufficiently.

During the simulations in each window, we collect the relevant data for the postprocessing analysis that leads to free energy profiles along the studied ζ. The data points are nothing else than the values along the defined ζ, in the present case bond length stretching. This means that for each time step of the MD run, the bond length on which we act with the bias potential is measured and printed. After collecting this data, we analyze them using the weighted histogram analysis method (WHAM),[45,46] which iteratively restores the free energy profile (FEP) from the molecular partition function in each window. For this, we need to know the temperature of the simulation, the harmonic bias potential force constant, and the values from the MD run itself.

Once the FEP is obtained, we can quantitatively evaluate the reaction's thermodynamics and kinetics at the experimental conditions. This method offers a direct link to the experimental measurements. In the case of agreement between theory and experiment, we can dial in on the changes in properties in specific parts along the reaction. It is important to note here that the qualitative accuracy of the described simulations is dependent on the underlying theory used. Although we use a QM/MM scheme using hybrid functionals with MM describing the metallic surface, a cautious approach when interpreting the calculated FEP is recommended. To avoid the presentation of absolute quantitative results, we calculate various similar reaction pathways which could either form the same product via another sequence or mechanism or form a different product by e.g., following similar reaction pathways in different positions of the reactant. This way, the resulting FEP of the proposed reaction pathway is put into the context of the molecule's possible reactions leading to various products.

3.5. Methods

Throughout the research on this thesis, three QM programs were used, and one for MM and MD simulations. For MD, the Amber package was utilized, specifically the free part known as Amber Tools, from which the Sander code was used as the MD engine.[47] This allows for the application of constraints required for the umbrella sampling simulations. Throughout this work, no calculations were using only standalone MM calculations and they were always coupled within QM/MM methodology. The QM/MM scheme was used in two QM codes, Gaussian,[48] and FIREBALL.[49]

The Gaussian suite is a well-established commercial program offering a wide range of DFT methods together with high-level post-HF techniques. This program was the main software used throughout the author's research presented herein. Routine calculations including geometry relaxations, BDE, and locations of TS were carried out in this program. It offers a versatile QM/MM environment ONIOM[50] belonging to the subtractive (extrapolative) scheme which allows for the inclusion of surface. The metallic surface was built with three atomic layers and the atoms were fixed. The vdW parameters for the metals in MM were obtained from the Interface FF.[51] The

inclusion of the vdW parameters was done by including `amber=softfirst` in the input line, and `VDW Au0 1.4755 5.2900` specifying the parameters for gold. In the case of silver, the parameters are `VDW Ag0 1.4775 4.5600`. In the calculations locating TS, an approximate geometry was first generated by hand, and then relaxation toward the first-order saddle point was performed. Once the algorithm successfully located the TS, it was confirmed by frequency analysis. BDE calculations were performed in three separate calculations, first, the reactant molecule was relaxed. Then, the total energies of the dissociated products were calculated at their relaxed geometries. The BDE was then calculated according to eq. 8. Concerning the level of theory, the go-to method was ωB97X-D[52] long-range separated functional with the def2-SVP[53] basis for relaxations and def2-TZVP[54] for single-point calculations. Other functionals used throughout the research presented herein include B3LYP,[37,55,56] PBE,[35] and PBE0.[35,57] In the case of performing umbrella sampling with Gaussian (Gaussian called for QM by Sander), the Sander routine had to be slightly modified to accommodate single-point calculations of wavefunction stability. Throughout the reaction coordinate of a reaction, the electronic structure of the reactants will change drastically. An issue may arise if the DFT calculation follows a solution that is unstable and another, lower energy solution exists. For this reason, stability optimization was performed at the beginning. After confirming a stable solution at a given geometry, corresponding to each window in umbrella sampling, the simulations were performed.

The second main QM program was FIREBALL. It is a fast DFT code, which allows efficient calculations of larger systems or longer simulations. Its main principle consists of precalculating the interaction integrals of all elements of interest on a fine grid at the desired level of theory. The resulting values are stored in a file and accessed by the code during the calculation itself. This way, the DFT calculations avoid the most expensive step and the jobs do not require parallelization. By including FIREBALL in Sander, it can be used to solve the QM part in QM/MM scheme within the MD simulations.

The third QM program used was Orca,[58,59] which includes the method of FT-DFT for calculations of integrated fractional occupation densities. The main details of the calculations are included in Chapter 3.2. The level of theory for the NFOD calculations includes the abovementioned GGA and hybrid functionals at the def2-TZVP basis set.

For the MD simulations, the Sander engine from AmberTools (part of the Amber program) was employed. The details of the umbrella sampling calculations as well as the protocol are described here. First, the reaction coordinate of investigated reaction must be well-defined. After that, various options are available. First, starting from the IS, we drive the structure along the reaction coordinate

by minimizing it in each window with given restraint and force constant k. Second, if we have TS located, we can start from there and drive the structure in both directions, toward IS and FS by applying the restraints in each window again. The best option in our case has proven to be to perform a minimization at 0 K in the initial steps. After obtaining the set of N structures for N windows, we start MD simulation runs. First, we must temper the system to a finite temperature, and finally, perform a simulation with constant temperature for data collection. In our case, since we are interested in C-H dissociation and/or C-C bond formation, the time step must include the shortest vibrations, which are C-H stretching modes. Therefore, the selected time step for our MD simulations is 0.5 fs, and the simulation time was set up to 10 ns. This ensures sufficient sampling along the reaction coordinate. Another important parameter of each MD simulation is the harmonic bias potential applied in each window. We have acquired a set of default values that are generally applicable to cyclodehydrogenation reactions with great success. The window spacing is usually set to 0.1 Å and the force constant k is set to 300 kcal·mol^{-1}·Å^{-2}. After the successful simulations, we plot the histogram of sampling in each window and check the overlap of all windows. If the TS is too steep, the sampling is usually poor around the high-energy points and the overlap is poor. In this case, additional windows with higher k are added to properly sample the whole conformational space along the reaction coordinate. After ensuring a sufficient overlap, we perform the final analysis using the weighted histogram analysis method (WHAM).[45]

4. Reaction mechanisms in on-surface synthesis protocols

4.1. Introduction

Traditional solution-based organic chemistry suffers from challenges such as poor regioselectivity and solubility issues due to the complex three-dimensional nature of reactions and the use of solvents. Additionally, the presence of a non-inert environment hinders the isolation of highly reactive species like radicals. However, a promising field has emerged that focuses on organic synthesis catalyzed by atomically flat surfaces under ultra-high vacuum (UHV) conditions.[13–15,60,61] This innovative approach allows for the preparation and isolation of new molecules and materials that were previously unattainable through conventional synthesis routes.[62–67] By utilizing this bottom-up strategy, the surface-based synthesis capitalizes on the unique properties of reactions occurring on a flat surface,[68,69] effectively reducing the reaction space to two or even one dimension.[70,71] This reduction offers numerous advantages, including enhanced control over reaction outcomes and the ability to induce planarization in deposited molecular precursors, depending on their structure and steric hindrance.[72]

The planarization induced by the surface interactions serves two principal purposes. Firstly, it catalyzes intramolecular cyclodehydrogenation reactions in non-planar precursors, effectively transforming them into planar structures.[73–76] Secondly, polymerization reactions occur exclusively within the molecular plane, enabling the formation of one- or two-dimensional polymer chains.[77–79] Such precise control over surface reaction processes opens up exciting possibilities for tailoring the properties and structures of synthesized molecules and materials. Furthermore, metallic surfaces, which are commonly used in this field, exhibit unique catalytic properties due to the presence of natively occurring metallic single adatoms at elevated temperatures.[69,80,81] Reactions on surfaces can be driven by various means, including temperature, light, or SPM tip, although only the first case was utilized within this research.

In summary, surface-based synthesis offers a novel strategy in organic chemistry by providing a controlled and versatile platform for the creation of novel molecules and materials. The ability to manipulate reactions on atomically flat surfaces under UHV conditions opens up new possibilities for achieving previously unattainable regioselectivity, isolation of reactive species, and precise control over polymerization processes. Computational chemistry is an important tool in this emerging field with advanced simulations and modeling techniques, contributing to an understanding of processes happening and allowing the design and development of future surface-based synthesis strategies.

Computational chemistry methods offer great insight into the studied problems, which in this case are reaction mechanisms. With an insight on the atomic level and an accurate description of electronic structure throughout the critical steps of reactions, the effects governing the studied reactions on a surface can be described in detail. One must ensure that the key aspects of OSS are properly described by the methodology used. The most apparent is the modeling of the surface. In most cases, the molecules interact with the metallic surfaces only weakly, which permits the use of cheaper techniques for modeling the surfaces. By describing the metallic surfaces with MM and all interactions being only non-covalent van der Waals forces, we are no longer limited by the size of the surface structure. This method is only justified in physisorbed molecules on metallic surfaces with small and homogeneous partial charges on the surface atoms. Another key feature of OSS is the adatoms, which play crucial roles by interacting with the deposited molecules and catalyzing chemical reactions. Since the adatoms are part of the reaction itself, they must be included in the QM partition. In some cases, a part of the surface below the reaction site needs to be treated by QM as well to capture the interactions and changes in electronic structure throughout the reaction. The third main aspect which needs to be taken into account when analyzing reactions is temperature and the evolution of the reaction system in time. By running MD simulations, we sample the molecular motion at finite temperatures throughout the reaction pathway and obtain two main results. One, we can analyze the trajectories in the sense of structures, involvement of individual atoms in the reaction, deformations, etc. Two, by applying the appropriate method, we can obtain free energy profiles of individual reaction pathways and compare their kinetics and thermodynamics, which we can relate to experimentally observed products.

In this chapter, we will present three projects on OSS with unusual reaction outcomes. The role and importance of theoretical calculations in each project will be discussed as well as the author's contribution to the project. The resulting publications in peer-reviewed scientific journals will be attached. Project number one is focused on 1D conjugated molecular chains of similar chemical structures but strikingly different products after on-surface cyclodehydrogenation reactions. Project two studies the cooperation effect of adatoms of different elements in the formation of colinear polymers. The last project discussed herein, focusing on OSS, investigates the mechanism of highly selective activation of aromatic C-H bond at room temperature by a single gold atom.

4.2. Intrapolymeric cyclization

When starting from two chemically similar reactants, they are expected to undergo nearly identical reactions. Here we discuss our findings on the reactivity of two seemingly equivalent molecular chains. Two polymers built from either anthracene or bisanthene moieties linked by ethynylene bridges (see Figure 5) were previously synthesized and characterized.[72]
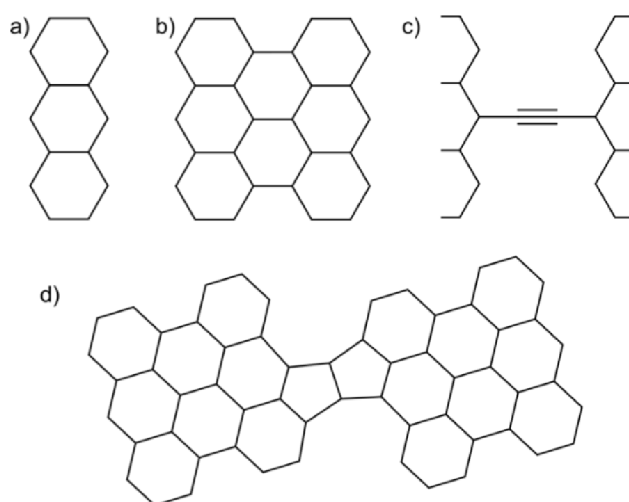
Figure 5: Chemical structures of anthracene (a), bisanthene (b), ethynylene linker (c), and pentalene linker (d). Hydrogens and double bonds were omitted for clarity.

However, after further thermal treatment, it was found that they undergo severely different reactions, leading to well-defined pentalene-bridged polymers in the case of bisanthene, and a plethora of defects in the case of anthracene. Theoretical analyses and simulations of reaction pathways were required to understand the processes leading to different products and uncover the driving forces for this behavior. The clues provided before and during the investigation included apparent differences in bond lengths along the bridges and theoretical calculations of the polymer's resonance structure.

4.2.1. Author's contribution to the published results

The author was tasked to propose various reaction pathways, calculate relevant properties, carry out simulations along proposed pathways, and propose a possible mechanism based on results. The straightforward way of proposing reaction pathways is by connecting start and finish with the least number of individual consecutive reaction steps. Due to irregular products from the anthracene polymer, our reference pathway follows the bisanthene transformation. For one linker to form a pentalene bridge, two dehydrogenation steps of the bisanthene (anthracene) units must occur, and one step of cyclization. It is important to note that the cyclization process closes both rings (of pentalene) concurrently and thus is regarded as one step. Then, from permutations of the proposed sequential steps, we obtain three reaction pathways along which we carry out our calculations and MD simulations. First, the location of transition states along each reaction step was done, and from these TS appropriate reaction coordinates for umbrella sampling simulations were defined. After the collection and analysis of the obtained free energy profiles, marginal differences were found between the two polymers, leaving the question of mechanism unanswered. The author then carried out calculations of the vibrational modes of the polymers in structures before the defining reaction step,

25

designed a methodology for analyzing the importance of each vibration, and analyzed the results. The analysis of the contribution of individual vibrations is shown in Figure 6.
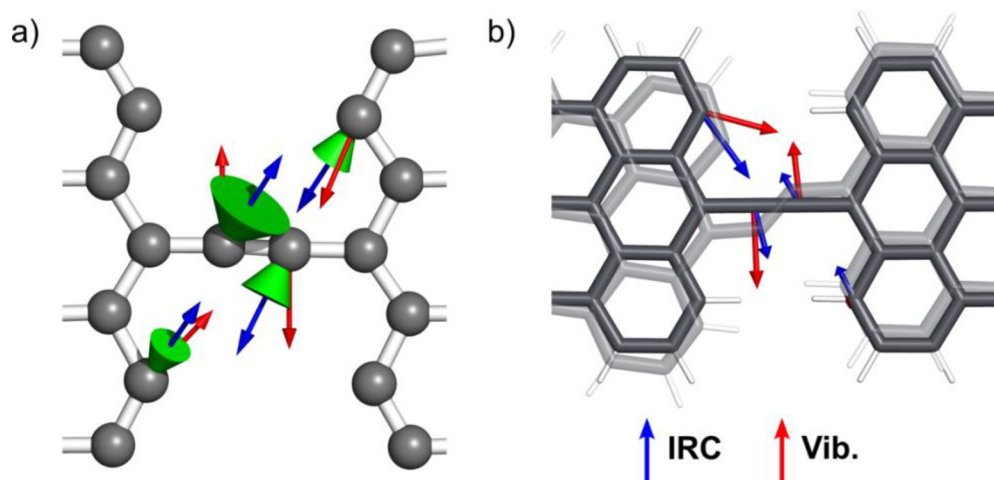

Figure 5: Visual comparison of relevant atomic movements within individual vibrational modes (red vectors) and atomic movements along the reaction coordinate from IS to TS (blue vectors). (a) an initial working version of visualization utilizing green cones as a guide for the angle difference between blue and red vectors. A cosine similarity can be presented in the accompanying table. (b) final visualization version from the published manuscript. IS is modeled with a solid backbone, and the TS structure is translucent.

It was found that the two polymers have distinctly different altered conjugation, which results in unlocking vibrations promoting the desired reaction steps in bisanthene. This conclusion could be drawn considering the clues provided by other calculations and experimental images hinting at the conjugation differences.

4.2.2. Article

Tailoring π-conjugation and vibrational modes to steer on-surface synthesis of pentalene-bridged ladder polymers

Bruno de la Torre [1,2,6], Adam Matěj [1,2,6], Ana Sánchez-Grande[3,6], Borja Cirera[3], Benjamin Mallada [1,2], Eider Rodríguez-Sánchez [3], José Santos [3,4], Jesús I. Mendieta-Moreno[2], Shayan Edalatmanesh [1,2], Koen Lauwaet[3], Michal Otyepka [1], Miroslav Medveď [1], Álvaro Buendía[5], Rodolfo Miranda[3,5], Nazario Martín [3,4 ✉], Pavel Jelínek [1,2 ✉] & David Écija[3 ✉]

The development of synthetic strategies to engineer π-conjugated polymers is of paramount importance in modern chemistry and materials science. Here we introduce a synthetic protocol based on the search for specific vibrational modes through an appropriate tailoring of the π-conjugation of the precursors, in order to increase the attempt frequency of a chemical reaction. First, we design a 1D π-conjugated polymer on Au(111), which is based on bisanthene monomers linked by cumulene bridges that tune specific vibrational modes. In a second step, upon further annealing, such vibrational modes steer the twofold cyclization reaction between adjacent bisanthene moieties, which gives rise to a long pentalene-bridged conjugated ladder polymer featuring a low bandgap. In addition, high resolution atomic force microscopy allows us to identify by atomistic insights the resonance form of the polymer, thus confirming the validity of the Glidewell and Lloyd′s rules for aromaticity. This on-surface synthetic strategy may stimulate exploiting previously precluded reactions towards π-conjugated polymers with specific structures and properties.

[1] Regional Centre of Advanced Technologies and Materials, Palacký University, Šlechtitelů 27, 783 71 Olomouc, Czech Republic. [2] Institute of Physics, The Czech Academy of Sciences, Cukrovarnická 10, 162 00, Prague 6, Czech Republic. [3] IMDEA Nanociencia, C/ Faraday 9, Ciudad Universitaria de Cantoblanco, 28049 Madrid, Spain. [4] Departamento de Química Orgánica, Facultad de Ciencias Químicas, Universidad Complutense, 28040 Madrid, Spain. [5] Departamento de Física de la Materia Condensada, Universidad Autónoma de Madrid, Cantoblanco, Madrid, Spain. [6] These authors contributed equally: Bruno de la Torre, Adam Matěj, Ana Sánchez-Grande. ✉email: nazmar@ucm.es; jelinekp@fzu.cz; david.ecija@imdea.org

he design and synthesis of π-conjugated polymers is a very active area of research with great potential for applications in organic field-effect transistors (OFETs), photovoltaics (OPVs), and light emitting diodes (OLEDs)[1–3].

However, the advance in the synthesis of π-conjugated polymers is hampered by concomitant limitations of solubility during the chemical synthesis[2,3]. This drawback is even enhanced in the design of π-conjugated ladder polymers, a singular type of polymers in which all the backbone is π-conjugated and fused[4]. These conjugated ladder polymers are of great appeal for materials science and optoelectronics due to their exceptional stability and optimum electron delocalization thanks to the restriction of free torsional motion in between monomers[4].

In the field of π-conjugated polymers, the topology of the π-electron network is crucial since it determines the ground state electronic structure of such materials. Polymers incorporating non-benzenoid polycyclic hydrocarbons are of increasing interest due their specific electronic properties[5]. In non-benzenoid systems, molecular orbital levels and π-electron density distribution are uneven compared to benzenoid systems, thereby polarizing the ground state and leading to unique behavior in excited states[5]. π-Extended non-benzenoid polycyclic hydrocarbons, such as pentalene, indacene or indenofluorene, have recently propelled rich insights into the electronic properties of antiaromaticity and/ or open-shell character[6–12]. On the one hand, antiaromatic compounds show better conducting properties than their aromatic counterparts[13]. On the other hand, non-benzenoid species are prone to express open-shell character in solution[6,7] and on surfaces[9–12].

Taking into account the aforementioned unique properties, it is of timely relevance to engineer conjugated ladder polymers incorporating non-benzenoid components, targeting to design chemically robust and low bandgap polymers. Such synthesis in wet chemistry must contend with structural defects and low solubility that prevent complete control over the synthesis and structural characterization at the atomic scale. To overcome these synthetic challenges, on-surface synthesis has emerged as a disruptive paradigm to develop chemical reactions on surfaces, while simultaneously monitoring and elucidating the precursors, intermediates and reaction products by means of scanning probe microscopy[14–18]. Despite the recent progress in on-surface synthesis, there are still very limited strategies to synthesize complex π-conjugated polymers with specific properties[14–27].

The electronic and chemical properties of π-conjugated polymers are driven by the inherent topology of their π-electrons. Here, we present a chemical strategy to allow unconventional synthetic pathways by exploiting the relation between π-conjugation and specific vibrational modes, being able to steer a desired chemical transformation. Our strategy is based on two sequential steps, i.e., a polymerization expressing specifically tailored π-topology, and a subsequent complex chemical ladderization involving a twofold cyclization by taking advantage of the unique vibrational capabilities of the inherent π-topology. In the first step, the on-surface formation of a one-dimensional polymeric precursor featuring cumulene bridges takes place, allowing bending vibrational modes of the polymer with a desired directionality. In the second and final steps, subsequent thermal annealing drives intrapolymeric cyclization reactions, triggered by such specific vibrational modes, giving rise to ladderization of the polymer and the expression within the polymeric main-chain of non-benzenoid fused pentalene bridges.

Results

Synthesis of pentalene-bridged bisanthene. Following this chemical strategy, we report the synthesis and detailed atomistic

characterization by a comprehensive scanning tunneling microscopy (STM) and non-contact atomic force microscopy (nc-AFM) supported by density functional theory (DFT) study of the on-surface reactions of two distinct molecular precursors, **4BrBiA** [10,10′-bis(dibromomethylene)-10H,10′H-9,9′-bianthracenylidene] and **4BrAn** [9,10-bis(dibromomethylene)-9,10-dihydroanthracene]. The precursors are endowed with = CBr$_2$ functionalities to allow homocoupling[23,27]. The deposition of **4BrAn** and **4BrBiA** on Au(111) and subsequent annealing at 500 K results in the formation of anthracene (**1**, Fig. 1a) and bisanthene (**2**, Fig. 1b) polymers, respectively[23,27]. Both polymers exhibit repeating moieties linked by linear bridges, but with distinct π-conjugation. While the anthracene polymer adopts aromatic ethynylene π-conjugation character[23], the bisanthene polymer results in the promotion of the quinoid cumulene-like character[27].

Further annealing at 650 K leads to distinct behavior of the formed polymers despite their chemical similarity. Our theoretical calculations (see later) reveal that, as a result of this different π-topology, the cumulene-like bridge (with a weakened triple bond) in the bisanthene polymer (**2**) allows the amplification of two bending vibrational modes of the bridging unit (see Fig. 2a), which promotes a distinct reaction mechanism with respect to the anthracene polymer (**1**) (see Fig. 1a and Supplementary Fig. 1). In the case of the cumulene-bridged bisanthene polymer (**2**) (see Fig. 1c) these vibrational modes substantially overlap with the intrapolymeric reaction coordinate. Their thermal excitation upon annealing at 650 K promotes the formation of fused pentalene bridges, which gives rise to a long and defect-free π-conjugated ladder polymer (**3**), as shown in Fig. 1d. High-resolution nc-AFM images acquired with CO-tip reveal that the fused bridging units are formed by pentalene moieties. Notably, this intrapolymeric ladderization reaction is highly selective and only minority concomitant defects are detected for submonolayer coverage. On the one hand, for the case of the anthracene polymer (**1**), annealing above 700 K results in distinct side reactions giving rise to irregular polymers with variety of defects (see Supplementary Fig. 1). Thus, the annealing of cumulene-linked bisanthene polymers allows chemical reactions that are precluded for the ethynylene-bridged anthracene wires.

Reaction mechanism of the on-surface synthesis of pentalene-bridged bisanthene. To get a deeper insight into these differences and the underlying reaction mechanism, we carried out quantum mechanical/molecular mechanics (QM/MM) simulations[28,29] with the aim of analyzing the optimal reaction pathways of the bridging units of both anthracene and bisanthene polymers towards the formation of pentalene links, for more details of computational model see section "Methods". In general, the feasibility of a chemical reaction is determined by two factors: (i) the Boltzmann exponential factor given by the activation energy barrier, and (ii) the attempt frequency ν expressing how often the system evolves towards the saddle point of the reaction pathway[30–33]. In the following, we will show that the π-conjugation form adopted by the polymer may also strongly influence the optimal reaction pathway by tuning both the activation energy and steering vibrational modes.

To find the most feasible reaction pathway towards the formation of the pentalene-bridged polymer (**3**), we attempted different reaction coordinates mimicking the first step of the reaction. Supplementary Fig. 2 displays two of the most relevant reaction coordinates. Namely, we have considered either a direct cyclization between the bridges and the rims of the monomers (see Fig. 2c) or a dissociation of the C–H bond at the zigzag edge of the bisanthene monomer mediated by an Au adatom (see
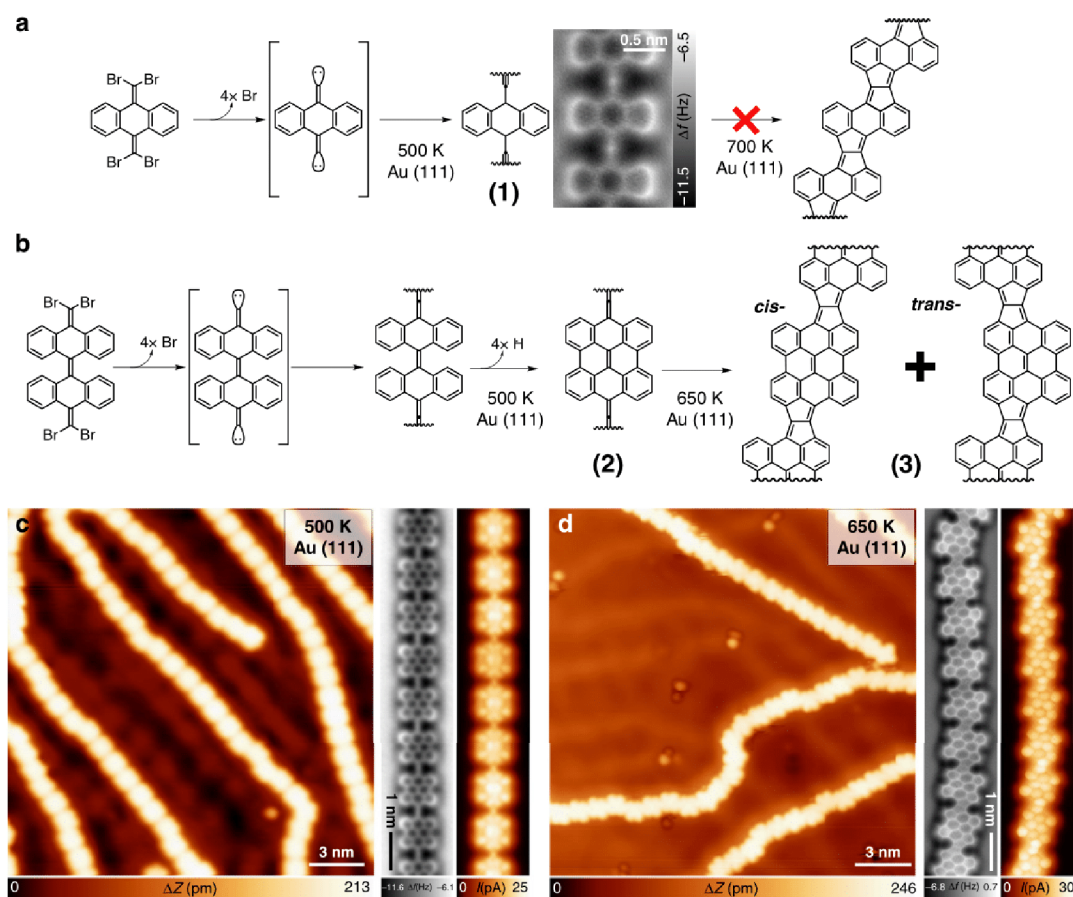
Fig. 1 On-surface synthesis of pentalene-bridged bisanthene polymers. a Scheme of the reaction sequence of **4BrAn** precursor after being deposited on Au(111), annealed to 500 K to obtain polymer **1**, and annealed up to 700 K to only produce irregular defective polymers (see Supplementary Fig. 1). **b** Scheme of the reaction sequence of **4BrBiA** precursor after being deposited on Au(111), annealed to 500 K to obtain polymer **2**, and annealed to 650 K to result in polymer **3**. **c** STM topographic overview (left panel; 0.03 V, 0.1 nA) and detailed nc-AFM/STM constant height images (right panels) of cumulene-linked bisanthene polymers (**2**). **d** STM topographic overview (left panel; 0.05 V, 0.1 nA) and detailed nc-AFM/STM constant height images (right panels) of pentalene-bridged bisanthene polymers (**3**).
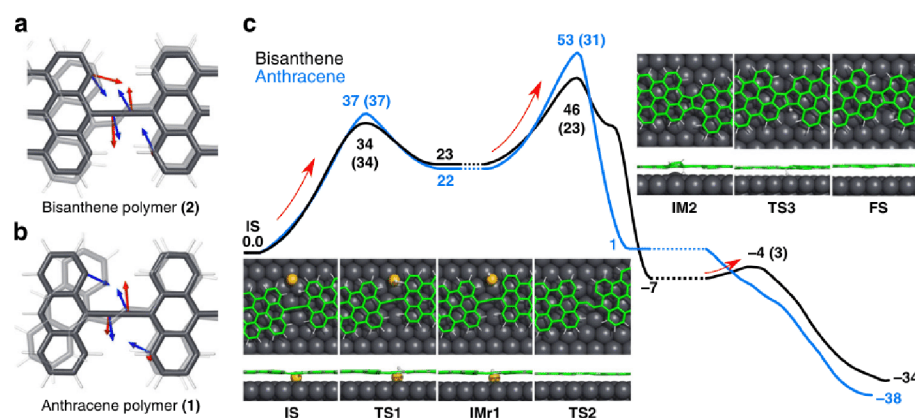

Fig. 2 Calculated vibrational modes and reaction pathways of polymers (1) and (2) on Au(111). a, b Comparison of calculated vibrational mode (red arrows) with reaction coordinates (blue arrows) for **a**, cumulene-like bridged bisanthene polymer (**2**) and for **b**, ethynylene-linked anthracene polymer (**1**). The atomic arrangement of the transition state (**TS2**) is showed in transparent mode. Reaction coordinates are defined as the displacement from the initial (**IMr1**) to the transition state (**TS2**) for the cyclization reaction pathway from **IMr1** to **IM2**. **c** Free energy barriers (in kcal mol^{-1}) for the optimal reaction pathway calculated for anthracene (**1**, blue) and bisanthene (**2**, black) polymers at 650 K. Values of the activation energies are presented in brackets. Inset figures show top and side views of the initial state (**IS**), transition states (**TS**), intermediates (**IM**) and final states (**FS**) of bisanthene polymer (**2**) optimal reaction pathway towards pentalene-bridged bisanthene polymer (**3**).

Supplementary Fig. 2d). The QM/MM calculations at 650 K show that the activation free energy for hydrogen abstraction (34 and 37 kcal mol^{-1}) is much lower than that of the direct cyclization (82 and 110 kcal mol^{-1}) for both bisanthene (2) and anthracene (1) polymers, respectively (see Supplementary Figs. 3 and 4). Thus, we assume that the first step of the reaction pathway is a hydrogen abstraction in both cases.

In the second step of the reaction, the cyclization process for both polymers (1 and 2) have slightly lower activation barrier than a second dehydrogenation by a few kcal mol^{-1} (see Supplementary Figs. 3 and 4). The calculated activation free energy of cyclization for the bisanthene polymer (2) is significantly smaller (23 kcal mol^{-1}) than that for the anthracene polymer (1, 31 kcal mol^{-1}). As the activation barriers of the cyclization process in the second reaction step are lower than those corresponding to the second hydrogen abstraction, the dehydrogenation-cyclization-dehydrogenation scenario (shown in Fig. 2 and also denoted by yellow lines in Supplementary Figs. 3 and 4) seems to be the optimal reaction pathway among the explored reaction pathways for both polymers. Nevertheless, experimentally we only observe the formation of the long and defect-free pentalene-bridged polymers from the bisanthene (2), but not from the anthracene (1) polymers. Thus, the activation energies cannot explain by themselves the experimental evidence.

However, the reaction rate also depends on the v prefactor, which is determined by available steering vibrational eigenmodes strongly overlapping with the reaction coordinates. Figure 2a, b shows the atomic arrangement in the transition state (shown in translucent color) of the cyclization reaction, which involves a bending distortion of the cumulene bridge. Thus, we carried out the dynamical matrix calculations of all vibrational modes of freestanding bisanthene/anthracene polymers, from which we selected only vibrational modes with dominant contribution of bending mode on the bridging linker adjacent to the periacene/acene unit with unsaturated carbon atom, see Supplementary Fig. 5. According to our analysis of the vibrational modes of bisanthene polymer (2), we can identify two bending vibrational modes that are coupled with the in-phase displacement of the unsaturated carbon atom of the bisanthene moiety (see red arrows in Fig. 2a). Such bending vibrational modes match very well with the cyclization reaction coordinate depicted by blue arrows in Fig. 2a (also see vibrational modes of bisanthene labeled 182 and 185 shown in Supplementary Fig. 5).

On the contrary, in the case of the anthracene polymer (1), all the vibrational modes consisting of the bending mode lack coupling with the in-phase movement of the unsaturated carbon atom (see Fig. 2b). Therefore, in the case of the cumulene-like bridged bisanthene polymer (2) the strong overlap of the bending vibrational modes with the cyclization reaction coordinates together with slightly higher vibrational frequencies provide larger attempt frequency v than in the case of ethynylene-linked anthracene polymer (1). Indeed, the bending modes of ethynylene-bridge of the anthracene polymer (1) are completely lack of the in-phase motion of the unsaturated carbon atoms, see Supplementary Fig. 5, which plays the important role in the formation of the pentalene bridge. As a result, the overlap between the cyclization reaction coordinate and the internal vibrational modes of the polymer is significantly reduced with respect to the bisanthene case. Consequently, this causes substantial drop of the corresponding attempt frequency v. Furthermore, the anthracene polymer (1) contains the ethynylene bridges, thus featuring a triple bond, which has distinct bonding character than the cumulene-like linkers of bisanthene polymer (2)[27]. Therefore, the frequencies of the steering bending modes of the ethynylene linkers in anthracene polymers (1) are lower by 50–100 cm^{-1} (i.e., a drop of ~10%) than those of cumulene-like

bridges in bisanthene polymers (2), as shown in Supplementary Fig. 5, leading to a further decrease of the attempt frequency.

In summary, the distinct π-conjugation of the bisanthene polymer (2) exhibiting the cumulene-like bridge is prone to the bending vibrational modes that steer the cyclization reaction. These bending vibrational modes coupled with the appropriated in-phase motion of bisanthene moiety enhance not only the attempt frequency v, but they also impose a lower energy cost of the bond distortion contributing to the activation energy than for the anthracene polymer (1). Altogether, these two factors facilitate the formation of the defect-free pentalene-bridged bisanthene polymers (3) as observed experimentally.

At this point, it is worth to point out that the hydrogenation abstraction is driven by the C–H stretching mode (~3100 cm^{-1}), which is approximately one order of magnitude larger than the frequencies of the C–C bending modes (~600 cm^{-1}), see Supplemental Fig. 5. Thus, the v prefactor and, consequently, the total rate of the dehydrogenation processes are enhanced. In the case of anthracene polymer (1), the energy barrier (36 kcal mol^{-1}) for the second dissociation is only slightly higher than that of the cyclization (31 kcal mol^{-1}) (see Supplementary Fig. 4). Consequently, considering that the steering C–H stretching mode is approximately one order of magnitude higher than the C–C bending modes, the reaction rates for the second dissociation or the cyclization at 700 K become similar. This opens a second reaction channel that includes a subsequent double dehydrogenation and cyclization reaction trajectory (denoted as a blue line in Supplementary Fig. 4). Notably, for this reaction trajectory of the anthracene polymer (1), the formation of the pentalene bridge occurs through quite distinct transition state (compare TS4 in Supplementary Fig. 4 with TS6 in Supplementary Fig. 3 for the bisanthene polymer) featuring very large activation energy (>100 kcal mol^{-1}), not shown in Supplementary Fig. 4. The QM/MM simulations indicate that unsaturated carbon atoms in the anthracene unit connect to the nearest carbon atoms on the ethynylene-bridge, which leads to a different atomic arrangement than in the bisanthene polymer. Such a process can be understood by the absence of the in-phase motion of the bending vibrational mode with the distant unsaturated carbon atoms of the anthracene unit as discussed previously. This result clearly demonstrates that the cyclization reaction coordinates forming the pentalene bridge from the ethynylene-bridged anthracene polymer (see Supplementary Fig. 2d) are no longer the optimal ones and other more favorable reaction mechanisms are presented. Thus, a formation of other defective structures is preferred, which is experimentally confirmed and illustrated in Supplementary Fig. 1. Such findings mean that other reaction pathways, including the double H-dissociation and cyclization, with lower activation energies and/or suitable active vibrational modes matching corresponding reaction coordinates, take place avoiding the formation of the pentalene-bridged anthracene polymers.

The discussion above points out the importance of the internal modes of the reactant on the chemical rate of a given reaction. From this perspective, it is worth to make a connection to well-established transition state theory[34], which is widely adopted to describe the chemical rates of diverse reaction mechanisms. Strictly speaking, in the transition state theory the rate of a reaction is determined by dynamics of the system at the transition state (i.e., dividing surface, which separates the phase space into a reactant and product region, placed at the lowest saddle point of potential energy surface). Importantly, one of the basic assumptions of the transition state theory is the existence of a quasi-equilibrium in the reactant region (i.e., between the reactants and the activated complex formed at the transition state). This assumption means that the reactants have sufficient kinetic

energy, which allows to reach the transition state (i.e., to form the activation complex) at certain frequency to establish the quasi-equilibrium. In the case of bimolecular reactions in gas phase, the required kinetic energy is often available through collision events of reactants. Therefore, such equilibrium can be reached depending on collision rates driven by temperature of system or kinetic energy of a molecular-beam. However, in the case of unimolecular reactions caused by an internal chemical transformation of the reactant, such as the one discussed above, the kinetic energy is driven mostly by internal vibrational modes of the reactant. Moreover, only vibrational modes with certain overlap with the reaction coordinates may contribute to the kinetic energy required to reach the transition state. Thus, it seems that not only the transition state, but also the internal vibrational modes of the reactant may play important role in such reaction mechanisms. We feel that our combined experimental and theoretical work provides a strong indication that, indeed, the vibrational modes of the initial state may play significant role on the rate. It is worth to point out that our rationalization roots back to early works from Polanyi introducing a concept of "early" and "late" reaction barriers[33], or, more recently, to control of reaction dynamics via excitations of reactant vibrational modes[31], and to modified versions of the transition state theory[35], including mode-specific reaction dynamics[32]. However, these recent theories have been tested to bimolecular reactions including reactants, much simpler than the polymers presented here.

Structural and the electronic properties of pentalene-bridged bisanthene polymers. Next, we focus on the structural and the electronic properties of pentalene-bridged bisanthene polymers (**3**), including the dominant resonance form. In general, the bisanthene-pentalene-bisanthene connections can feature *trans* or *cis* (Fig. 1b) configurations. A statistical analysis of the abundance of the covalent motifs reveals that both configurations are equally favorable. However, segments having repeating *trans* or *cis* motifs were found with a maximum length of twelve units.

Clar's π-sextet rule, an extension of Huckel's rule for polycyclic aromatic hydrocarbons (PAHs), states that the Kekulé resonance structure with the largest number of disjoint aromatic π-sextets, i.e., benzene-like moieties, is the most important resonance structure for the characterization of the PAHs properties. Since our pentalene-bridged polymers present non-benzenoid units, the rule to be used here is an extension of Clar's π-sextet rule, the one proposed by Glidewell and Lloyd[36,37]. This rule states that the total population of π-electrons in conjugated polycyclic systems tends to form the smallest $4n + 2$ groups and to avoid the formation of the smallest $4n$ groups. The pentalene bridge can show two types of resonance forms, i.e., the inner bond can be single or double. From this assumption, at least two distinct resonance forms can be plotted as illustrated in Fig. 3a. By applying the Glidewell and Lloyd's rule, it is evident that the conjugated structure associated with an inner single bond (black structure in Fig. 3a) should be the most stable, since the other option (gray structure in Fig. 3a) would imply the formation of four groups with 4π-electrons in the bisanthene moiety, which must be avoided according to the rule. Interestingly, by following the observed π-conjugation, the system stabilizes four Clar's sextets in the bisanthene (depicted in blue in Fig. 3a), the maximum number.

To assess the expression of the Glidewell and Lloyd's rule on surfaces, we take advantage of the capabilities of nc-AFM with functionalized CO-tip[38,39] to resolve the C–C bond order[40]. High-resolution nc-AFM images of the pentalene-bridged polymers (see Fig. 3b) clearly show distinct bond lengths within the

inner part of the polymer, whose statistically average value is plotted in the central panel of Fig. 3b (see Supplementary Fig. 6 for more details). The variation of bond distances is qualitatively confirmed by DFT calculations (right panel of Fig. 3b). The results reveal that the variation in the bond length of the polymer bonds matches the π-resonance form predicted by the Glidewell and Lloyd's rule, confirming its validity.

Next, the degree of aromaticity and antiaromaticity of the bisanthene polymer is characterized by performing nucleus-independent chemical shift calculations (NICS). Positive values of NICS indicate antiaromaticity, close-to-zero values reveals non-aromaticity, and negative figures correspond to aromaticity. Figure 3c shows that the five-membered rings are highly antiaromatic, whereas the outer six-membered rings of the bisanthene moieties are aromatic, thus corroborating the resonance form discussed above.

In order to elucidate the electronic structure of the π-conjugated polymers, we first calculated the electronic structure of freestanding polymer using B3LYP-DFT, which revealed the presence of dispersive valence (VB) and conduction (CB) bands separated by a bandgap of ~1 eV (Fig. 3d). Spatially resolved dI/dV scanning tunneling spectra were recorded over the molecular wires and the clean Au(111) surface. As illustrated in Fig. 3e, one frontier resonance is distinguished at −0.6 eV, assigned to the valence band (VB) edge and a broad peak with an elbow at 0.5 eV, interpreted as the conduction band (CB) edge, displaying a maximum at 0.9 eV. This results in a low bandgap of ~1.1 eV. We should note that the bandgap value obtained from STS measurements is typically reduced by an additional electron screening imposed by the proximity of a metallic surface with respect to the intrinsic bandgap of the gas phase polymer[41,42]. Within the bandgap the downshifted surface state convoluted with tip states is observed. The dI/dV map at the VB edge shows maxima over lateral termini of the bisanthene moiety, without charge density over the pentalene bridge (see Fig. 3f). The dI/dV map of CB edge exhibits states over the armchair region of the bisanthene units and on the void spaces adjacent to the pentalene bridges (see Fig. 3f). Despite the fact that DFT simulations cannot predict correctly the magnitude of the intrinsic bandgap of the polymer[43], they describe the character of frontier orbitals of the VB and CB edges of the bisanthene polymer very well. Indeed, the agreement between experimental and simulated dI/dV maps is excellent, validating the character of the frontier orbitals predicted by DFT. Thus, the fused pentalene-bridged bisanthene polymers are low bandgap polymers, featuring antiaromatic bridging units, heralding potential for near-infrared activity, high conductivity, and ambipolar charge transport[44–46].

Discussion

Our results introduce the importance of tailoring π-conjugation and vibrational modes on surfaces to promote otherwise precluded chemical reaction pathways. Following this strategy, we reveal that a cumulene-like bridged bisanthene polymer is prone to undergo ladderization into a fused pentalene-linked bisanthene polymer through a twofold cyclization process, thanks to specific steering vibrational modes. The absence of such modes in an ethynylene-linked anthracene polymer featuring similar coordination environment, but very distinct π-topology of the linker, blocks the ladderization reaction and reveals the hidden and relevant influence of the resonance form of the bridge in the chemical reaction. Moreover, the presented study indicates that not only the transition state, but also the internal vibrational modes of the reactant may play important role in reaction
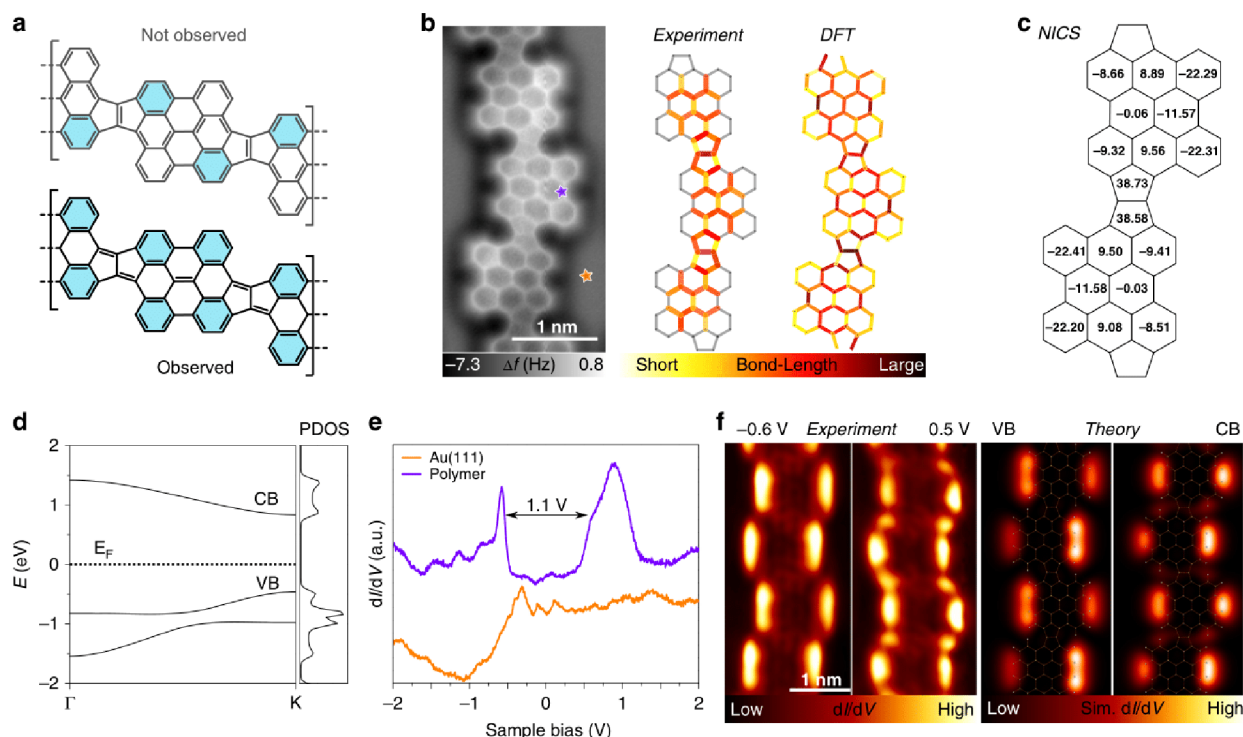
Fig. 3 Resonance and electronic structure of the pentalene-bridged bisanthene polymer (3). a Not observed and observed resonance forms of polymer **3**, featuring *cis* configuration. **b** High-resolution nc-AFM image of a section of the pentalene-bridged bisanthene polymer (left panel) and sketch illustrating the average bond lengths statistically measured from experimental nc-AFM images (central panel) and DFT calculation (right panel) of the bond lengths of a *trans*- section of the polymer. **c** NICS calculations of a pentalene-linked bisanthene dimer at distance of 1 Å above the center of each ring. **d** Calculated electronic structure of a freestanding cumulene-like bridged bisanthene polymer (**3**). **e** dI/dV scanning tunneling spectra acquired at selected site on polymer **3** and on Au(111) as indicated by stars in **b**. **f** Experimental and simulated dI/dV maps of the valence (VB) and conduction band (CB) of polymer **3**.

mechanisms. As this, we hope that our findings will stimulate new direction of both experimental and theoretical activities towards better understanding of the chemical reaction rates, especially those on-surface reactions driven by internal vibrational modes.

We envision our studies will open avenues to engineer highly demanded conjugated nanomaterials, while showing strategies to incorporate non-benzenoid moieties in polymeric science in order to steer relevant electronic phenomena of interest for molecular optoelectronics and organic solar cells. Notably, our results highlight the versatility of on-surface synthesis for designing non-benzenoid based nanomaterials featuring low bandgaps, which are of utmost interest because of their near-infrared activity and ambipolar charge transport character[44–46].

Methods

Sample preparation and experimental details. Experiments were performed in two independent custom designed ultra-high vacuum systems that host a low-temperature Omicron and a Createc scanning tunneling microscope, respectively, where the base pressure was below 5×10^{-10} mbar. STM images were acquired with electrochemically etched tungsten tips or cut and sharpened by focus ion beam (FIB) Pt/Ir tips, applying a bias (V_b) to the sample at a temperature of ~4 K. Precursor molecules were synthesized in our group following a procedure described in refs. [19–21]. The Au(111) substrate was prepared by standard cycles of Ar$^+$ sputtering (800 eV) and subsequent annealing at 723 K for 10 min. Molecular precursor were deposited by organic molecular-beam epitaxy (OMBE) from a quartz crucible maintained at 373 K (**4BrAn**) or 443 K (**4BrBiAn**) onto a clean Au (111) held at room temperature. Whenever necessary samples were annealed to the desired temperature for 20 min and subsequently transferred to the STM stage, which was maintained at 4.2 K. For the spectroscopic measurements, specific site dI/dV and dI/dV maps were acquired with conventional lock-in technique with a modulation of 5 and 10 mV, respectively. In nc-AFM imaging, a Pt/Ir tip mounted on a qplus sensor (resonance frequency ≈30 kHz; stiffness ≈ 1800 N m^{-1}) was oscillated with a constant amplitude of 50 pm. The tip apex was functionalized with

a CO-molecule, and all images were captured in constant height mode and a bias sample of 1 mV. AFM images are raw data whereas STM images were subject to standard processes. The images were processed using WSxM[47] software.

Computational details. We employed density functional theory (DFT) calculations to analyze atomic and electronic structure for freestanding infinite systems of anthracene and bisanthene polymers presented in Fig. 3 using FHI-AIMS packages[48] using B3LYP[49] exchange-correlation functionals. Systems were allowed to relax until the remaining atomic forces reached below 10^{-2} eV Å^{-1}. For all infinite systems with periodic boundary condition (PBC), a Monkhorst-Pack grid of 18 x 1 x 1 was used to sample the Brillouin zone. Theoretical dI/dV maps were calculated by FHI-AIMS with Probe Particle SPM code[50] s-like orbital tip[51]. Vibrational modes of freestanding anthracene and bisanthene polymers featuring conformation IMr1 (Supplementary Fig. S5) and consisting of four acene/periacene units were calculated using dynamical matrix approach with Fireball code[28].

To analyze the optimal reaction pathways, we used a QM/MM Fireball/Amber[29] method based on the combination of classical force-field techniques with Amber[52] and local orbital DFT with Fireball[28]. In the MM part consisting of slab (40 × 20) with three layers, we used the interface force-field[53]. In the QM region consisting of polymer and select gold atoms of surface placed under the bridging unit where the reaction took place (see Supplementary Fig. 2a, b), we used the Fireball DFT method with BLYP exchange-correlation functional[54] with D3 corrections[55] and norm-conserving pseudopotentials. We employed a basis set of optimized numerical atomic-like orbitals (NAOs)[56] with a 1 s orbital for H and sp$_3$ orbitals for C atoms. Note that Fireball DFT-BLYP calculations provide very similar atomic and electronic structure of both anthracene and bisanthene polymers as FHI-AIMS DFT-B3LYP calculations. Before energy profile calculations, we have performed a QM/MM geometry relaxation followed by a thermalization of the system from 100 to 500 K in order to equilibrate the system. The free energy profile was performed with the WHAM method[57]. In each window of WHAM, we run a QM/MM MD of 2000 steps at 650 K with a time step of 0.5 fs. Calculated NICS(1)$_{zz}$ values shown in Fig. 3c were evaluated using GIAO method[58] at spin-unrestricted ωB97X-D[59]/cc-pVDZ[60] level of theory in Gaussian09[61]. Tetrameric molecules were relaxed at the same level prior to NMR calculations.

Data availability
The data that support the findings of this study are available from the corresponding authors upon reasonable request.

References
1. Heeger, A. J. Semiconducting and metallic polymers: the fourth generation of polymeric materials (Nobel Lecture). *Angew. Chem. Int. Ed.* **40**, 2591–2611 (2001).
2. Guo, X., Baumgarten, M. & Müllen, K. Designing π-conjugated polymers for organic electronics. *Prog. Polym. Sci.* **38**, 1832–1908 (2013).
3. Facchetti, A. Π-conjugated polymers for organic electronics and photovoltaic cell applications. *Chem. Mater.* **23**, 733–758 (2011).
4. Lee, J., Kalin, A. J., Yuan, T., Al-Hashimi, M. & Fang, L. Fully conjugated ladder polymers. *Chem. Sci.* **8**, 2503–2521 (2017).
5. Tobe, Y. Quinodimethanes incorporated in non-benzenoid aromatic or antiaromatic frameworks. *Top. Curr. Chem.* **376**, 12 (2018).
6. Parkhurst, R. R. & Swager, T. M. in Polyarenes II (eds Jay S. Siegel & Yao-Ting Wu) 141–175 (Springer International Publishing, 2014).
7. Zeng, Z. et al. Pro-aromatic and anti-aromatic π-conjugated molecules: an irresistible wish to be diradicals. *Chem. Soc. Rev.* **44**, 6578–6596 (2015).
8. Frederickson, C. K., Rose, B. D. & Haley, M. M. Explorations of the indenofluorenes and expanded quinoidal analogues. *Acc. Chem. Res.* **50**, 977–987 (2017).
9. Mishra, S. et al. Tailoring bond topologies in open-shell graphene nanostructures. *ACS Nano* **12**, 11917–11927 (2018).
10. Liu, J. et al. Open-shell nonbenzenoid nanographenes containing two pairs of pentagonal and heptagonal rings. *J. Am. Chem. Soc.* **141**, 12011–12020 (2019).
11. Di Giovannantonio, M. et al. On-surface synthesis of antiaromatic and open-shell indeno[2,1-b]fluorene polymers and their lateral fusion into porous ribbons. *J. Am. Chem. Soc.* **141**, 12346–12354 (2019).
12. Mishra, S. et al. Topological defect-induced magnetism in a nanographene. *J. Am. Chem. Soc.* **142**, 1147–1152 (2020).
13. Fujii, S. et al. Highly-conducting molecular circuits based on antiaromaticity. *Nat. Commun.* **8**, 15984 (2017).
14. Fan, Q., Gottfried, J. M. & Zhu, J. Surface-catalyzed C–C covalent coupling strategies toward the synthesis of low-dimensional carbon-based nanostructures. *Acc. Chem. Res.* **48**, 2484–2494 (2015).
15. Talirz, L., Ruffieux, P. & Fasel, R. On-surface synthesis of atomically precise graphene nanoribbons. *Adv. Mater.* **28**, 6222–6231 (2016).
16. Shen, Q., Gao, H.-Y. & Fuchs, H. Frontiers of on-surface synthesis: from principles to applications. *Nano Today* **13**, 77–96 (2017).
17. Sun, Q., Zhang, R., Qiu, J., Liu, R. & Xu, W. On-surface synthesis of carbon nanostructures. *Adv. Mater.* **30**, 1705630 (2018).
18. Clair, S. & de Oteyza, D. G. Controlling a chemical coupling reaction on a surface: tools and strategies for on-surface synthesis. *Chem. Rev.* **119**, 4717–4776 (2019).
19. Cai, J. et al. Graphene nanoribbon heterojunctions. *Nat. Nanotechnol.* **9**, 896–900 (2014).
20. Steiner, C. et al. Hierarchical on-surface synthesis and electronic structure of carbonyl-functionalized one- and two-dimensional covalent nanoarchitectures. *Nat. Commun.* **8**, 14765 (2017).
21. Moreno, C. et al. Bottom-up synthesis of multifunctional nanoporous graphene. *Science* **360**, (2018).
22. Sánchez-Sánchez, C. et al. On-surface synthesis and characterization of acene-based nanoribbons incorporating four-membered rings. *Chem. Eur. J.* **25**, 12074–12082 (2019).
23. Sánchez-Grande, A. et al. On-surface synthesis of ethynylene bridged anthracene polymers. *Angew. Chem. Int. Ed.* **58**, 6559–6563 (2019).
24. Li, J. et al. Band depopulation of graphene nanoribbons induced by chemical gating with amino groups. *ACS Nano* **14**, 1895–1901 (2020).
25. Urgel, J. I. et al. On-surface synthesis of cumulene-containing polymers via two-step dehalogenative homocoupling of dibromomethylene-functionalized tribenzoazulene. *Angew. Chem. Int. Ed.* **59**, 13281–13287 (2020).
26. Galeotti, G. et al. Synthesis of mesoscale ordered two-dimensional π-conjugated polymers with semiconducting properties. *Nat. Mater.* **19**, 874–880 (2020).
27. Cirera, B. et al. Tailoring topological order and pi-conjugation to engineer quasi-metallic polymers. *Nat. Nanotechnol.* **15**, 421–423 (2020).
28. Lewis, J. P. et al. Advances and applications in the FIREBALL ab initio tight-binding molecular-dynamics formalism. *Phys. Status Solidi B* **248**, 1989–2007 (2011).
29. Mendieta-Moreno, J. I. et al. FIREBALL/AMBER: an efficient local-orbital DFT QM/MM method for biomolecular systems. *J. Chem. Theory Comput.* **10**, 2185–2193 (2014).
30. Vineyard, G. H. Frequency factors and isotope effects in solid state rate processes. *J. Phys. Chem. Solids* **3**, 121–127 (1957).
31. Crim, F. F. Chemical dynamics of vibrationally excited molecules: controlling reactions in gases and on surfaces. *Proc. Nat. Acad. Sci. USA* **105**, 12654 (2008).
32. Guo, H. & Liu, K. Control of chemical reactivity by transition-state and beyond. *Chem. Sci.* **7**, 3992–4003 (2016).
33. Polanyi, J. C. Concepts in reaction dynamics. *Acc. Chem. Res.* **5**, 161–168 (1972).
34. Truhlar, D. G., Garrett, B. C. & Klippenstein, S. J. Current status of transition-state theory. *J. Phys. Chem.* **100**, 12771–12800 (1996).
35. Bao, J. L. & Truhlar, D. G. Variational transition state theory: theoretical framework and recent developments. *Chem. Soc. Rev.* **46**, 7548–7596 (2017).
36. Glidewell, C. & Lloyd, D. MNDO study of bond orders in some conjugated bi- and tri- cyclic hydrocarbons. *Tetrahedron* **40**, 4455–4472 (1984).
37. El Bakouri, O., Poater, J., Feixas, F. & Solà, M. Exploring the validity of the Glidewell–Lloyd extension of Clar's π-sextet rule: assessment from polycyclic conjugated hydrocarbons. *Theor. Chem. Acc.* **135**, 205 (2016).
38. Gross, L., Mohn, F., Moll, N., Liljeroth, P. & Meyer, G. The chemical structure of a molecule resolved by atomic force microscopy. *Science* **325**, 1110 (2009).
39. Jelínek, P. High resolution SPM imaging of organic molecules with functionalized tips. *J. Phys: Condens. Matter* **29**, 343002 (2017).
40. Gross, L. et al. Bond-order discrimination by atomic force microscopy. *Science* **337**, 1326–1329 (2012).
41. Neaton, J. B., Hybertsen, M. S. & Louie, S. G. Renormalization of molecular electronic levels at metal-molecule interfaces. *Phys. Rev. Lett.* **97**, 216405 (2006).
42. Amy, F., Chan, C. & Kahn, A. Polarization at the gold/pentacene interface. *Org. Electron.* **6**, 85–91 (2005).
43. Cohen, A. J., Mori-Sánchez, P. & Yang, W. Insights into current limitations of density functional theory. *Science* **321**, 792 (2008).
44. Steckler, T. T. et al. Very low band gap thiadiazoloquinoxaline donor–acceptor polymers as multi-tool conjugated polymers. *J. Am. Chem. Soc.* **136**, 1190–1193 (2014).
45. Dou, L., Liu, Y., Hong, Z., Li, G. & Yang, Y. Low-bandgap near-IR conjugated polymers/molecules for organic electronics. *Chem. Rev.* **115**, 12633–12665 (2015).
46. Kawabata, K., Saito, M., Osaka, I. & Takimiya, K. Very small bandgap π-conjugated polymers with extended thienoquinoids. *J. Am. Chem. Soc.* **138**, 7725–7732 (2016).
47. Horcas, I. et al. WSxM: a software for scanning probe microscopy and a tool for nanotechnology. *Rev. Sci. Instrum.* **78**, 013705 (2007).
48. Blum, V. et al. Ab initio molecular simulations with numeric atom-centered orbitals. *Comput. Phys. Commun.* **180**, 2175–2196 (2009).
49. Becke, A. D. Density-functional thermochemistry. III. The role of exact exchange. *J. Chem. Phys.* **98**, 5648 (1998).
50. Hapala, P. et al. Mechanism of high-resolution STM/AFM imaging with functionalized tips. *Phys. Rev. B* **90**, 085421 (2014).
51. Krejčí, O., Hapala, P., Ondráček, M. & Jelínek, P. Principles and simulations of high-resolution STM imaging with a flexible tip apex. *Phys. Rev. B* **95**, 045407 (2017).
52. Case, D. A. et al. *AMBER 2018.* University of California, San Francisco (2018).
53. Heinz, H., Lin, T.-J., Kishore Mishra, R. & Emami, F. S. Thermodynamically consistent force fields for the assembly of inorganic, organic, and biological nanostructures: The INTERFACE Force Field. *Langmuir* **29**, 1754–1765 (2013).
54. Lee, C., Yang, W. & Parr, R. G. Development of the Colle-Salvetti correlation-energy formula into a functional of the electron density. *Phys. Rev. B* **37**, 785–789 (1988).
55. Grimme, S., Ehrlich, S. & Goerigk, L. Effect of the damping function in dispersion corrected density functional theory. *J. Comput. Chem.* **32**, 1456–1465 (2011).
56. Basanta, M. A., Dappe, Y. J., Jelínek, P. & Ortega, J. Optimized atomic-like orbitals for first-principles tight-binding molecular dynamics. *Comput. Mater. Sci.* **39** 759–766 (2007).
57. Kumar, S., Rosenberg, J. M., Bouzida, D., Swendsen, R. H. & Kollman, P. A. The weighted histogram analysis method for free-energy calculations on biomolecules. I. The method. *J. Comput. Chem.* **13**, 1011–1021 (1992).
58. Ditchfield, R. Self-consistent perturbation theory of diamagnetism. *Mol. Phys.* **27**, 789–807 (1974).
59. Chai, J.-D. & Head-Gordon, M. Long-range corrected hybrid density functionals with damped atom–atom dispersion corrections. *Phys. Chem. Chem. Phys.* **10**, 6615–6620 (2008).
60. Dunning, T. H. Gaussian basis sets for use in correlated molecular calculations. I. The atoms boron through neon and hydrogen. *J. Chem. Phys.* **90**, 1007–1023 (1989).
61. Gaussian 09, R. D. et al. *Gaussian, Inc.* (Wallingford, CT, 2013).

Acknowledgements

Author contributions

N.M., P.J., and D.E. conceived and designed the experiments. P.J., N.M., and D.E. supervised the project and led the collaboration efforts. B.T., A.S.-G., B.C., B.M., and D.E. carried out the experiments and obtained the data. J.S., E.R.-S., and N.M. synthesized the precursors. The experimental data were analyzed by B.T., A.M., A.S.-G., B.C., K.L., A.B., R.M., P.J., and D.E. and discussed by all the authors. A.M., J.M., S.E., M.O., M.M., and P.J. performed the calculations. The manuscript was written by B.T., N.M., P.J., and D.E. with contribution from all the authors.

Competing interests

The authors declare no competing interests.

Additional information

Supplementary information is available for this paper at https://doi.org/10.1038/s41467-020-18371-2.

Correspondence and requests for materials should be addressed to N.M., P.J. or D.Éc.

Peer review information *Nature Communications* thanks Aitor Mugarza, Magalí Lingenfelder and Oteyza Dimas G for their contribution to the peer review of this work. Peer reviewer reports are available.

Reprints and permission information is available at http://www.nature.com/reprints

Publisher's note Springer Nature remains neutral with regard to jurisdictional claims in published maps and institutional affiliations.

4.3.   Cooperative effects of sodium and silver

A three-fold symmetric molecule of hexaaxatriphenylene (HAT) was deposited on the Ag(111) surface, a 2D self-assembly was observed thereafter, and the following annealing resulted in HAT desorption without evident on-surface reactions. In the case of the co-deposition of NaCl onto Ag(111), the same self-assembly of HAT was observed together with NaCl islands. A radically different scenario occurred after the annealing step, after which covalent colinear polymers of HAT were present on the clean Ag(111) surface. Experiments showed that part of sodium atoms remained on the surface, while all Cl was desorbed during the heating as AgCl. Hence, Cl$^-$ does not contribute to the reaction, while Na$^+$ plays a crucial role in polymerization. Theoretical calculations were employed to explain the role of sodium cations in the observed OSS and to propose a reaction mechanism that leads to the colinear polymers.

4.3.1. Author's contribution to the published results

The author's task was to mainly probe and propose suitable mechanisms explaining the formation of colinear covalent HAT polymers. The key information provided by experiments highlights the necessity for the Na$^+$ ions to be present. Initial calculations comparing the binding energies of Na$^+$ and Ag with HAT molecules points to a stronger interaction with the previous. This allows the formation of noncovalent dimers (two HAT bound by Na$^+$), which withstand higher temperatures without desorbing. This first piece of new information sheds light on the importance of sodium presence for high-temperature chemical reactions. The main part of the author's calculations followed, the investigation of possible reaction pathways leading to colinear molecular chains.

In this case, the initial state of the explored reaction was the noncovalent dimer. In this structure, three symmetrically inequivalent hydrogens are present, and dissociation thereof would lead to various possible products, see Figure 7. It is noteworthy that the species binding the two polymers together is unknown. The two bidentate ligands (each HAT has two N atoms in each "pocket") together with a partial negative charge on each nitrogen offer variable binding options. The C-H dissociation was considered to be catalyzed by Ag adatoms, and the TS along the reaction steps was localized. After that, umbrella sampling MD simulations were carried out to obtain free energy profiles for a direct comparison of various paths.
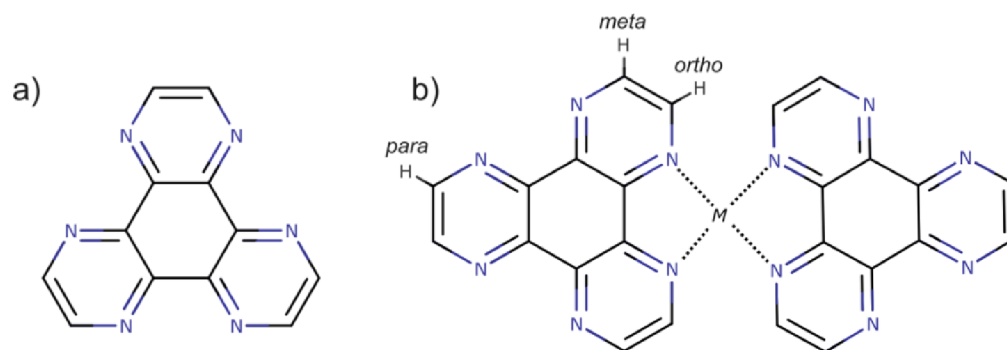
Figure 6: (a) chemical structure of HAT monomer. (b) noncovalent dimer bound together by a metal adatom in two bidentate pockets. Three inequivalent hydrogen positions are labeled. Hydrogens were omitted for clarity.

In this study, we carried out the umbrella sampling using two programs for benchmarking. More details are written either in Chapter 3.2. Methods, or in the Methods section within the attached article below. This approach was opted for due to the inclusion of Na^+ for which our group had no experience and results using the FIREBALL code. The umbrella sampling MD simulations using Amber and linked Gaussian programs required special attention to the routines generating the input and calling the Gaussian jobs due to possible wavefunction instabilities along the reaction coordinate. This issue was troubleshot and resolved, and the final free energy profile (calculation of only one reaction step due to high computation time and resources) was compared with our standard Amber/FIREBALL method. The comparison shows a nearly identical profile shape with a change in the barrier height of around 5 kcal/mol. It is important to note here that the Amber/FIREBALL results overestimate the barrier height with respect to the higher accuracy Amber/Gaussian method.

4.3.2. Article

GDCh

Communications

Angewandte
Chemie
International Edition
www.angewandte.org

Check for updates

Surface Chemistry

Exploiting Cooperative Catalysis for the On-Surface Synthesis of Linear Heteroaromatic Polymers via Selective C–H Activation

Xunshan Liu+, Adam Matej+, Tim Kratky, Jesús I. Mendieta-Moreno, Sebastian Günther,
*Pingo Mutombo, Silvio Decurtins, Ulrich Aschauer, Jascha Repp, Pavel Jelinek,**
Shi-Xia Liu, and Laerte L. Patera**

Abstract: Regiospecific C–H activation is a promising approach to achieve extended polymers with tailored structures. While a recent on-surface synthetic approach has enabled regioselective homocoupling of heteroaromatic molecules, only small oligomers have been achieved. Herein, selective C–H activation for dehydrogenative C–C couplings of hexaazatriphenylene by Scholl reaction is reported for the first time. By combining low-temperature scanning tunneling microscopy (STM) and atomic force microscopy (AFM), we revealed the formation of one-dimensional polymers with a double-chain structure. The details of the growth process are rationalized by density functional theory (DFT) calculations, pointing out a cooperative catalytic action of Na and Ag adatoms in steering the C–H selectivity for the polymerization.

The dehydrogenative coupling reaction of two arene rings and the ring-closing cyclodehydrogenation process mediated by non-oxidizing Lewis acids (Scholl reaction) as well as the analogous oxidative aromatic coupling reaction occupy a prominent place in the synthetic chemistry of polycyclic (hetero)aromatic compounds.[1–4] These synthetic protocols are particularly advantageous since biaryl linkages can be formed without any prefunctionalization of precursor molecules. Not surprisingly, the Scholl reaction proved to be

most useful for the formation of multiple fused rings to obtain polycyclic arenes and nanographene compounds.[5–9] However, the C–H activation/arylation step in the synthesis of polycyclic aromatic hydrocarbons (PAHs) generally lacks selectivity because the C–H bonds have, besides a low intrinsic reactivity, only small relative differences in their reactivity.[9,10] Complementary to the well-established Scholl reaction in solution, the analogous surface-assisted C–C coupling process exhibits stunning efficiency for the fabrication of nanographenic and other atomic-scale structures.[11–13] For the intramolecular bond formation, the cyclodehydrogenation process occurs between two arene rings in close proximity and consequently, its regioselectivity can to a large extent be controlled.[12,14–16] However, for the intermolecular case, the bond selectivity of the dehydrogenative aryl–aryl coupling cannot be predicted a priori when the molecules contain several C–H bonds.[17–19]

Recently, the selectivity in aryl–aryl coupling has been addressed by exploiting the regioselectivity of on-surface homocoupling of tetraazapolycyclic pyrazino[2,3-*f*:4,7]phenanthroline molecules (pap) on the Au(111) substrate.[20] There the C–H bond scission was reported to be clearly regiospecific, since *ortho*-hydrogen atoms of the pyrazine rings are preferentially activated over their pyridine equivalents, as clarified by scanning tunneling (STM) and noncontact atomic force microscopy (AFM)

[*] Dr. X. Liu,+ Prof. Dr. S. Decurtins, Prof. Dr. U. Aschauer,
PD Dr. S.-X. Liu
Department of Chemistry, Biochemistry and Pharmaceutical Sciences
University of Bern
3012 Bern (Switzerland)
E-mail: shi-xia.liu@unibe.ch

Dr. X. Liu+
Department of Chemistry, Zhejiang Sci-Tech University
Hangzhou (China)

A. Matej,+ Dr. J. I. Mendieta-Moreno, Dr. P. Mutombo,
Prof. Dr. P. Jelinek
Institute of Physics of Czech Academy of Sciences
16200 Prague (Czech Republic)
E-mail: jelinekp@fzu.cz

A. Matej,+ Prof. Dr. P. Jelinek
Regional Centre of Advanced Technologies and Materials
Czech Advanced Technology and Research Institute (CATRIN)
Palacký University Olomouc
78371 Olomouc (Czech Republic)

T. Kratky, Prof. Dr. S. Günther, Dr. L. L. Patera
Department of Chemistry and Catalysis Research Center
Technical University of Munich
85748 Garching (Germany)
E-mail: laerte.patera@tum.de

Prof. Dr. J. Repp, Dr. L. L. Patera
Institute of Experimental and Applied Physics
University of Regensburg
93053 Regensburg (Germany)

[+] These authors contributed equally to this work.

imaging.[20] However, the resulting covalent structures were limited in size, being restricted to small clusters, mainly composed of dimers, trimers and tetramers. While this approach allows controlling the selectivity of the Scholl reaction, novel strategies for the synthesis of extended polymers are still needed. Cooperative catalysis, where multiple catalysts and catalytic cycles work synergistically to promote single-bond formation, is an appealing approach to achieve new reaction schemes.[21–23] However, its potential in the field of on-surface synthesis has largely been unexplored.

Here, we report on a surface-assisted synthetic protocol which leads to selective C–H activation for dehydrogenative C–C couplings of hexaazatriphenylene (HAT) molecules,[24] affording linear heteroaromatic polymers in the presence of Na adatoms on a Ag(111) surface (Scheme 1). Each HAT chain is featured with contiguous bidentate N^N coordination pockets induced by cisoid conformations for catena-2,2′-(1,10-phenanthroline) skeletons along the chain. Two chains are aligned in parallel through Na coordination to N^N chelating pockets. Previously, gold–adatom coordination to a tetradentate N^N pocket was observed to steer a cisoid conformation for the formation of a dimeric pap molecule, two of which are also parallel aligned via two gold adatoms coordination to N^N pockets.[20] Similarly, a cisoid on-surface conformation of 2,2′-bipyridine triggered by metal coordination was demonstrated.[25] Notably, its chelate complex with a single Na atom is formed when a π-conjugated tetrathiafulvalene-fused dipyridophenazine molecule is adsorbed on NaCl/Cu(111).[26] In the present work, the growth of two coordinatively bonded HAT chains, which are observed to be of equal length, is inherently due to a regiospecific homocoupling of a (HAT)$_2$-Na dimer through selective activation of the C–H bonds in *meta*-positions to the N^N chelating pocket. In other words, this polymerization is initiated by complexation with Na forming a (HAT)$_2$-Na dimer while the subsequent C–H activation with high selectivity is catalyzed by individual Ag adatoms, finally leading to a double-chain structure via the dehydrogenative aryl-aryl coupling.

Deposition of the HAT molecules on the Ag(111) surface kept at ≈10 K and sequential annealing to 300 K (Figure 1a) result in extended crystals, consisting mainly of
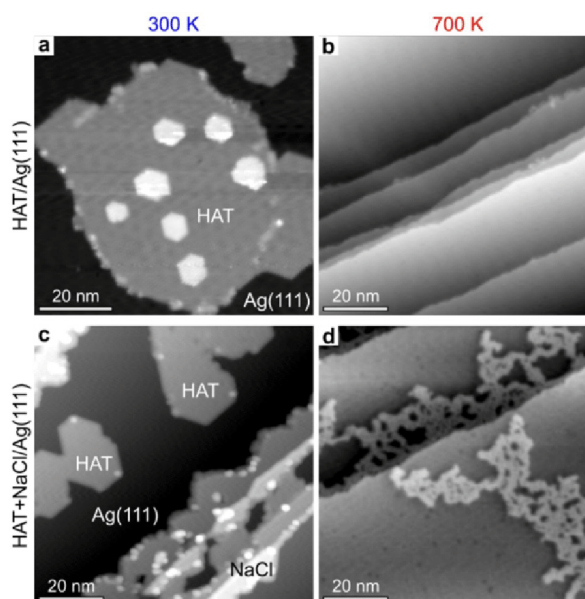

Figure 1. On-surface synthesis of heteroaromatic polymers. a, b) STM images acquired after annealing a sub-monolayer of HAT on Ag(111) to 300 K (a), showing extended self-assembled monolayers, with small bilayer islands, and to 700 K (b). c, d) STM images acquired after annealing a sub-monolayer of HAT and NaCl (0.3 ML) on Ag(111) to 300 K (c) and 700 K (d). All the images have been acquired in constant-current STM mode. a) Measurement parameters: tunneling current $I = 1.7$ pA, sample bias voltage $V = 1.0$ V. b) $I = 1.9$ pA, $V = 1.0$ V. c) $I = 1.4$ pA, $V = 1.5$ V. d) $I = 1.1$ pA, $V = 1.0$ V.

self-assembled monolayer islands.[24] Subsequent annealing to 700 K leads to the complete desorption of the molecules (Figure 1b). A different scenario is instead observed once a NaCl sub-monolayer (ML) is co-deposited together with the HAT molecules (Figure 1c). There, upon subsequent annealing to 700 K, no NaCl island has been observed, while polymers are found on the Ag surface (Figure 1d), covering the step edges, and extending on the flat terraces. A close-up at the polymers by STM imaging (Figure 2a) shows that the products are composed of linear structures (see Figure S1).
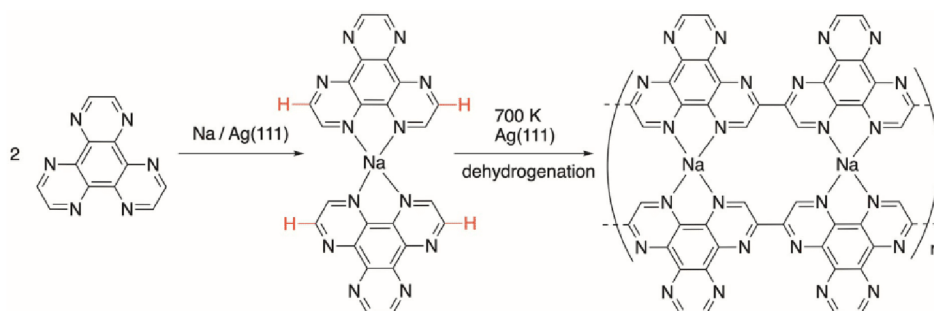
Scheme 1. A schematic illustration of the surface-assisted polymerization of HAT molecules in the presence of Na. Adjacent chains are aligned via contiguous N^N coordination pockets offering four-fold coordination sites.
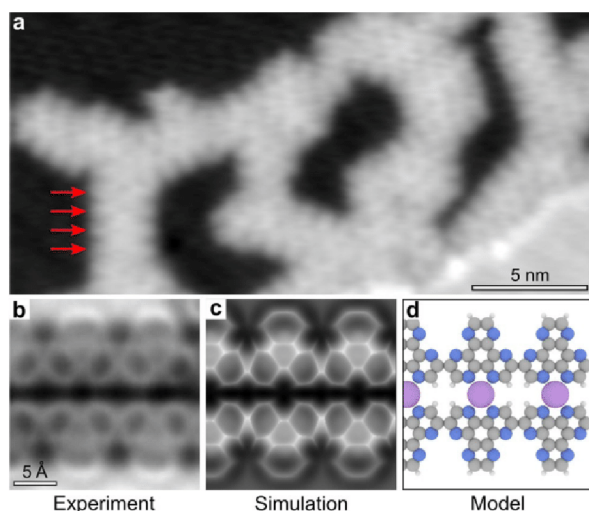
Figure 2. Linear heteroaromatic polymers. a) Constant-current STM image after annealing to 700 K of a Ag(111) surface covered by a sub-monolayer of HAT and NaCl (0.3 ML). Arrows indicate the positions of monomers in a linear chain ($I = 1.3$ pA, $V = 1.0$ V). b) Constant-height Δf AFM image acquired with a CO-functionalized tip at $\Delta z = -2.7$ Å, given with respect to an STM setpoint of ($I = 1.1$ pA, $V = 0.1$ V). AFM oscillation amplitude, $A = 0.5$ Å. c, d) Simulated AFM image and structural model, respectively. d) Grey, blue, white and violet spheres represent carbon, nitrogen, hydrogen and sodium atoms, respectively.

These experimental observations raise the point about the role of the co-deposited NaCl film in enabling a reaction pathway for the dehydrogenative C–C coupling of the HAT molecules. Upon thermal treatment of co-deposited HAT and NaCl sub-monolayers on Ag surfaces, the ionic lattice decomposes (see XPS data in Figure S2), with Cl$^-$ desorbing in form of volatile AgCl species,[27] while part of the Na remains on the surface.[28] This suggests a potential role of the Na adatoms in driving the polymerization. Spontaneous dissociation of NaCl and subsequent coordination of Na adatoms with organic molecules have been reported to occur upon surface annealing at elevated temperatures.[28–32] However, apart from simple intramolecular reactions such as tautomeric isomerization of guanine[33] and deprotonation of terephthalic acid,[34] no Na-assisted intermolecular coupling has been identified so far.

Detailed insight is provided by AFM imaging with CO-functionalized tips.[35] The contrast in the AFM frequency shift (Δf) image (Figure 2b) clarifies the formation of covalent bonds between the HAT molecules, whereby the activation of the hydrogen atoms in *meta*-positions to the chelating N atoms leads to covalently bonded linear structures (Figure 2b). Notably, each chain is coupled with a parallel one, indicating the presence of atomic species which coordinate to adjacent chelating N^N pockets. However, likely due to the lower adsorption height with respect to the molecular structures, they cannot be resolved by constant-height AFM imaging.[36,37] Since both Na and Ag adatoms could potentially coordinate with the HAT molecules, chemical identification of the atomic species is crucial. Upon deposition of the HAT molecules on the bare Ag(111) and

annealing to 300 K, high-resolution AFM imaging revealed the formation of purely H-bonded structures, without any evidence of organometallic structures involving Ag adatoms.[24] This evidence suggests that coordination of the HAT molecules with Ag adatoms is not favorable, even at rather elevated temperatures where native surface adatoms become largely available,[38] indicating the incorporation of Na adatoms in the chelating N^N pockets. This scenario is also supported by the simulated constant-height AFM image[39] in Figure 2c, obtained using fully relaxed atomic structure of HAT polymer coordinated by Na on the Ag(111) surface (Figure 2d).

We performed quantum mechanical calculations to elucidate a possible reaction mechanism and regioselectivity of HAT molecules towards one-dimensional polymers. Namely we studied first the role of Na adatoms in the formation of the chain. Therefore, to understand the importance of Na, we carried out a comparative study of the interaction of Na and Ag adatoms with the monomer and dimer of HAT molecules on the Ag(111) surface. While the calculated Hirshfeld charge of a Ag adatom ($+0.04$ e) is negligible, showing its neutral character, the Na adatom has a notable positive charge ($+0.35$ e). This indicates a cationic character of sodium adatoms on the surface (see Table S1). The calculated binding energies of Na and Ag adatoms to HAT molecules show greater binding energy with the former for both monomer and dimer complexes (see Table S2). This demonstrates that an organometallic dimer formed by two HAT molecules with a Na adatom in between is the most stable system. Figure 3 displays the calculated differential electron density ($\Delta\rho$), defined as $\Delta\rho = \rho_{all} - \rho_{complex} - \rho_{Ag(111)}$, being ρ_{all}, $\rho_{complex}$ and $\rho_{Ag(111)}$, the electron
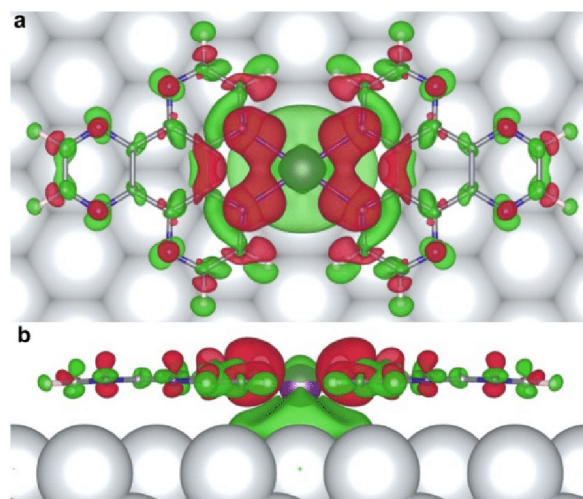
Figure 3. Calculated charge transfer between the (HAT)$_2$-Na complex and the Ag(111) surface. The differential electron density ($\Delta\rho$) is displayed at an isosurface of 0.005 e Å^{-3}. Green and red colors represent negative and positive values of $\Delta\rho$, respectively. The spatial distribution of $\Delta\rho$ indicates strong interactions between the (HAT)$_2$-Na complex and Ag(111) via a pronounced charge transfer from the HAT ligands to the Ag(111). a, b) Top and side views, respectively.

densities of the relaxed complex on the surface, of the complex in the gas phase, and of the bare Ag(111) surface, respectively. The spatial distribution of $\Delta\rho$ indicates the presence of coordination bonds between Na and N atoms of HAT molecules (see also Figure S3). The total energy DFT calculations of the dimer $(HAT)_2$-Na complex on the Ag(111) surface reveal strong interactions between them, as corroborated by a pronounced charge transfer from HAT ligands to the substrate, which enhances the binding energy (see Table S2) of the dimer on the Ag(111) substrate. Notably, the formation of the $(HAT)_2$-Na complex substantially increases the desorption temperature with respect to bare HAT molecules, allowing for higher reaction temperatures to be reached before desorption from the surface. Thus, sodium complexation enables to reach elevated annealing temperatures facilitating the condition for polymerization reaction.

It is evident that the polymerization has to be initiated through removal of hydrogen atoms to form a free radical which will facilitate intermolecular covalent coupling between HAT units. Therefore, we first analyzed the bond-dissociation energies (BDE) for three inequivalent hydrogens presented in the monomer $(HAT)_1$-Na and dimer $(HAT)_2$-Na complexes, as shown in Figure 4a, b. Calculated values of BDE indicate a preferential hydrogen removal near the Na adatom. These BDE values in both cases (95.6 kcal mol^{-1} for the monomer and 92.4 kcal mol^{-1} for the dimer) are lower than a calculated BDE value for a free HAT molecule (112.2 kcal mol^{-1}) although still too high for temperature-driven direct C–H bond scission. Thus, we considered the possibility that the C–H bond breaking is mediated by an Ag adatom acting as a catalyst. In fact, such mobile adatoms, commonly present on metal surfaces at elevated temperatures, have been recently shown to promote important reaction steps, as keto-enol tautomeric dehydrogenation,[40] and C–C coupling.[41–43] Therefore, we carried out QM/MM[44] free energy calculations with WHAM methodology[45] to explore this hypothesis. Indeed, the QM/MM simulations reveal significant reduction of activation energies by ≈ 60 kcal mol^{-1}. We found that the lowest activation energy barrier of the dehydrogenation corresponds to *meta* position, 35.4 kcal mol^{-1}, for a molecule dimer (green in Figure 4c, d). The activation energies for the *ortho* (blue in Figure 4c, d) and *para* (red in Figure 4c, d) are slightly higher, being 41.9 and 50.2 kcal mol^{-1} respectively. It is between the dimer $(HAT)_2$-Na and the monomer $(HAT)_1$-Na (55 kcal mol^{-1}, Figure S4) where we observe that the dimer is not only the most stable structure, but also has a lower activation energy by 20 kcal mol^{-1}. These results point toward kinetically driven regioselectivity with a propensity of the system toward polymerization in the direction perpendicular to the $(HAT)_2$-Na complex, creating two parallel 1D chains held together by Na in tetradentate N^N position. It is worth emphasizing that the hydrogen removal in Figure 4 is only the first reaction step toward the polymer. The resulting $(HAT)_2$-Na radical complex is highly susceptible to the formation of covalently bonded complexes with adjacent $(HAT)_2$-Na radical rather than HAT itself, due to the energetic preference of the H- removal at their

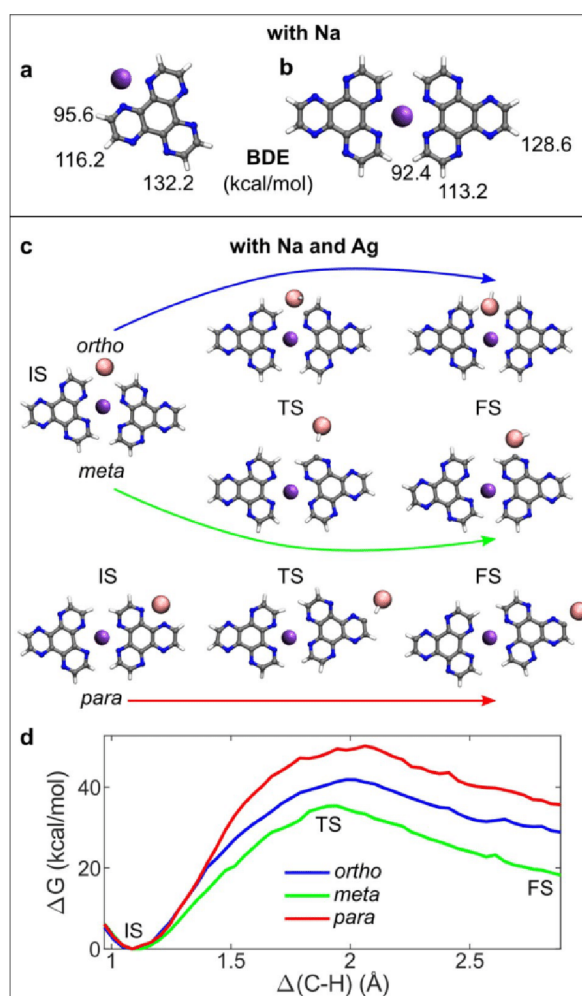**Figure 4.** HAT-Na complexes: $(HAT)_1$-Na (a) and $(HAT)_2$-Na (b). Bond-dissociation energies (BDE) for three inequivalent hydrogens are shown. Cooperative role of Na and Ag (c, d). Reaction pathways for the hydrogen removal in *ortho*, *meta* and *para* configurations (c). Corresponding free energy calculations as a function of the C–H distance (Δ) of the activated bond (d). Initial (IS), transition (TS), and final (FS) states are indicated (c, d).

meta positions. Therefore, we can assume that growth of linear polymeric structures occurs via coupling of $(HAT)_2$-Na complexes, rather than through the attachment of individual HAT radicals. This scenario is supported by the experimental observation of polymers composed of two chains of equal length, suggesting that the polymers grow directly as coupled chains, rather than by chain pairing upon cooling.

In conclusion, we investigated the on-surface polymerization of HAT molecules on Ag(111) in the presence of Na adatoms, leading to the formation of one-dimensional structures composed of coupled polymeric chains. By combining high-resolution scanning probe microscopy with DFT calculations, we elucidated the peculiar cooperative catalytic role of Na and Ag adatoms in steering both the polymerization and the regioselectivity of the Scholl reac-

tion. Our results pave the way to further studies on cooperative catalytic effects of metal adatoms in steering novel coupling reactions on surfaces.

Acknowledgements

Conflict of Interest

The authors declare no conflict of interest.

Keywords: Atomic force microscopy · Cooperative effects · On-surface synthesis · Scanning tunneling microscopy · Surface chemistry

[1] M. Grzybowski, K. Skonieczny, H. Butenschoen, D. T. Gryko, *Angew. Chem. Int. Ed.* **2013**, *52*, 9900–9930; *Angew. Chem.* **2013**, *125*, 10084–10115.

[2] A. A. Sarhan, C. Bolm, *Chem. Soc. Rev.* **2009**, *38*, 2730–2744.

[3] D. Myśliwiec, B. Donnio, P. J. Chmielewski, B. Heinrich, M. Stępień, *J. Am. Chem. Soc.* **2012**, *134*, 4822–4833.

[4] Y. Cao, X.-Y. Wang, J.-Y. Wang, J. Pei, *Synlett* **2014**, *25*, 313–323.

[5] A. Narita, X.-Y. Wang, X. Feng, K. Müllen, *Chem. Soc. Rev.* **2015**, *44*, 6616–6643.

[6] M. S. Little, S. G. Yeates, A. A. Alwattar, K. W. Heard, J. Raftery, A. C. Edwards, A. V. Parry, P. Quayle, *Eur. J. Org. Chem.* **2017**, 1694–1703.

[7] Y. Han, Z. Xue, G. Li, Y. Gu, Y. Ni, S. Dong, C. Chi, *Angew. Chem. Int. Ed.* **2020**, *59*, 9026–9031; *Angew. Chem.* **2020**, *132*, 9111–9116.

[8] M. Uryu, T. Hiraga, Y. Koga, Y. Saito, K. Murakami, K. Itami, *Angew. Chem. Int. Ed.* **2020**, *59*, 6551–6554; *Angew. Chem.* **2020**, *132*, 6613–6616.

[9] H. Ito, Y. Segawa, K. Murakami, K. Itami, *J. Am. Chem. Soc.* **2019**, *141*, 3–10.

[10] B. T. King, J. Kroulík, C. R. Robertson, P. Rempala, C. L. Hilton, J. D. Korinek, L. M. Gortari, *J. Org. Chem.* **2007**, *72*, 2279–2288.

[11] J. Cai, P. Ruffieux, R. Jaafar, M. Bieri, T. Braun, S. Blankenburg, M. Muoth, A. P. Seitsonen, M. Saleh, X. Feng, K. Müllen, R. Fasel, *Nature* **2010**, *466*, 470–473.

[12] L. Grill, S. Hecht, *Nat. Chem.* **2020**, *12*, 115–130.

[13] P. Ruffieux, S. Wang, B. Yang, C. Sánchez-Sánchez, J. Liu, T. Dienel, L. Talirz, P. Shinde, C. A. Pignedoli, D. Passerone, T. Dumslaff, X. Feng, K. Müllen, R. Fasel, *Nature* **2016**, *531*, 489–492.

[14] J. Liu, R. Berger, K. Müllen, X. Feng, *From Polyphenylenes to Nanographenes and Graphene Nanoribbons*, Springer, Heidelberg, **2017**, pp. 1–32.

[15] Q. Fan, J. M. Gottfried, J. Zhu, *Acc. Chem. Res.* **2015**, *48*, 2484–2494.

[16] S. Clair, D. G. de Oteyza, *Chem. Rev.* **2019**, *119*, 4717–4776.

[17] Q. Fan, S. Werner, J. Tschakert, D. Ebeling, A. Schirmeisen, G. Hilt, W. Hieringer, J. M. Gottfried, *J. Am. Chem. Soc.* **2018**, *140*, 7526–7532.

[18] Q. Sun, C. Zhang, H. Kong, Q. Tan, W. Xu, *Chem. Commun.* **2014**, *50*, 11825–11828.

[19] C.-X. Wang, Q. Jin, C.-H. Shu, X. Hua, Y.-T. Long, P.-N. Liu, *Chem. Commun.* **2017**, *53*, 6347–6350.

[20] N. Kocić, X. Liu, S. Chen, S. Decurtins, O. Krejčí, P. Jelínek, J. Repp, S. X. Liu, *J. Am. Chem. Soc.* **2016**, *138*, 5585–5593.

[21] K. Sonogashira, Y. Tohda, N. Hagihara, *Tetrahedron Lett.* **1975**, *16*, 4467–4470.

[22] Q. Bi, X. Huang, G. Yin, T. Chen, X. Du, J. Cai, J. Xu, Z. Liu, Y. Han, F. Huang, *ChemCatChem* **2019**, *11*, 1295–1302.

[23] G. M. Sammis, H. Danjo, E. N. Jacobsen, *J. Am. Chem. Soc.* **2004**, *126*, 9928–9929.

[24] L. L. Patera, X. Liu, N. Mosso, S. Decurtins, S.-X. Liu, J. Repp, *Angew. Chem. Int. Ed.* **2017**, *56*, 10786–10790; *Angew. Chem.* **2017**, *129*, 10926–10930.

[25] S. Freund, R. Pawlak, L. Moser, A. Hinaut, R. Steiner, N. Marinakis, E. C. Constable, E. Meyer, C. E. Housecroft, T. Glatzel, *ACS Omega* **2018**, *3*, 12851–12856.

[26] T. Meier, R. Pawlak, S. Kawai, Y. Geng, X. Liu, S. Decurtins, P. Hapala, A. Baratoff, S.-X. Liu, P. Jelínek, E. Meyer, T. Glatzel, *ACS Nano* **2017**, *11*, 8413–8420.

[27] M. Bowker, K. Waugh, *Surf. Sci.* **1983**, *134*, 639–664.

[28] C. Wäckerlin, C. Iacovita, D. Chylarecka, P. Fesser, T. A. Jung, N. Ballav, *Chem. Commun.* **2011**, *47*, 9146.

[29] T. K. Shimizu, J. Jung, H. Imada, Y. Kim, *Angew. Chem. Int. Ed.* **2014**, *53*, 13729–13733; *Angew. Chem.* **2014**, *126*, 13949–13953.

[30] K. Zhou, H. Liang, M. Wang, S. Xing, H. Ding, Y. Song, Y. Wang, Q. Xu, J.-H. He, J. Zhu, W. Zhao, Y. Ma, Z. Shi, *Nanoscale Adv.* **2020**, *2*, 2170–2176.

[31] J. Hieulle, D. Peyrot, Z. Jiang, F. Silly, *Chem. Commun.* **2015**, *51*, 13162–13165.

[32] C. Zhang, L. Wang, L. Xie, H. Kong, Q. Tan, L. Cai, Q. Sun, W. Xu, *ChemPhysChem* **2015**, *16*, 2099–2105.

[33] C. Zhang, L. Xie, L. Wang, H. Kong, Q. Tan, W. Xu, *J. Am. Chem. Soc.* **2015**, *137*, 11795–11800.

[34] D. Skomski, S. Abb, S. L. Tait, *J. Am. Chem. Soc.* **2012**, *134*, 14165–14171.

[35] L. Gross, F. Mohn, N. Moll, P. Liljeroth, G. Meyer, *Science* **2009**, *325*, 1110–1114.

[36] F. Queck, O. Krejčí, P. Scheuerer, F. Bolland, M. Otyepka, P. Jelínek, J. Repp, *J. Am. Chem. Soc.* **2018**, *140*, 12884–12889.

[37] L. L. Patera, Z. Zou, C. Dri, C. Africh, J. Repp, G. Comelli, *Phys. Chem. Chem. Phys.* **2017**, *19*, 24605–24612.

[38] Z. Yang, J. Gebhardt, T. A. Schaub, T. Sander, J. Schönamsgruber, H. Soni, A. Görling, M. Kivala, S. Maier, *Nanoscale* **2018**, *10*, 3769–3776.

[39] P. Hapala, G. Kichin, C. Wagner, F. S. Tautz, R. Temirov, P. Jelínek, *Phys. Rev. B* **2014**, *90*, 085421.

[40] H. Kong, C. Zhang, Q. Sun, X. Yu, L. Xie, L. Wang, L. Li, S. Hu, H. Ju, Y. He, J. Zhu, W. Xu, *ACS Nano* **2018**, *12*, 9033–9039.

[41] M. Fritton, D. A. Duncan, P. S. Deimel, A. Rastgoo-Lahrood, F. Allegretti, J. V. Barth, W. M. Heckl, J. Björk, M. Lackinger, *J. Am. Chem. Soc.* **2019**, *141*, 4824–4832.

[42] L. L. Patera, F. Bianchini, C. Africh, C. Dri, G. Soldano, M. M. Mariscal, M. Peressi, G. Comelli, *Science* **2018**, *359*, 1243–1246.

[43] B. de la Torre, A. Matěj, A. Sánchez-Grande, B. Cirera, B. Mallada, E. Rodríguez-Sánchez, J. Santos, J. I. Mendieta-Moreno, S. Edalatmanesh, K. Lauwaet, M. Otyepka, M.

Medveď, Á. Buendía, R. Miranda, N. Martín, P. Jelínek, D. Écija, *Nat. Commun.* **2020**, *11*, 4567.

[44] J. I. Mendieta-Moreno, R. C. Walker, J. P. Lewis, P. Gómez-Puertas, J. Mendieta, J. Ortega, *J. Chem. Theory Comput.* **2014**, *10*, 2185–2193.

[45] S. Kumar, J. M. Rosenberg, D. Bouzida, R. H. Swendsen, P. A. Kollman, *J. Comput. Chem.* **1992**, *13*, 1011–1021.

4.4. High regioselectivity of aromatic C-H bond

The reactivity and functionalization of aromatic compounds are challenging due to relatively strong C-H bonds and their ambiguity. Targeting specific bonds and ensuring high selectivity would open possibilities for cleaner and cheaper synthetic routes of numerous chemicals, including pharmaceutics, the food industry, agriculture, etc. Herein, we present an example of single gold atoms at room temperature (RT) dissociating aromatic C-H bonds and forming organometallic dimers. Most importantly, this reaction happens exclusively in one of two possible positions, rendering the observed reaction regiospecific with the marginal chemical difference between the two C-H bonds.

4.4.1. Author's contribution to the published results

A simple aromatic molecule, dicianoanthracene (DCA) was previously reported on various metallic surfaces, and formations of different self-assembly phases were observed.[82–84] In the case of depositing DCA onto a clean Ag(111) surface, a simple close-packed self-assembly is formed. The situation changes when gold atoms are co-deposited onto the silver surface. A new phase is seen, consisting of covalently bound DCA dimers with an atom binding the two molecules. Thus, organometallic dimers are formed in the presence of gold adatoms on a silver surface. What is more, the reaction is highly regioselective, offering a potential mechanism for new synthetic routes in OSS. With other theoretical calculations probing the nature of the gold adatoms, the author was again tasked with the design of the theoretical analysis and proposing a reaction mechanism that would explain the observed products.
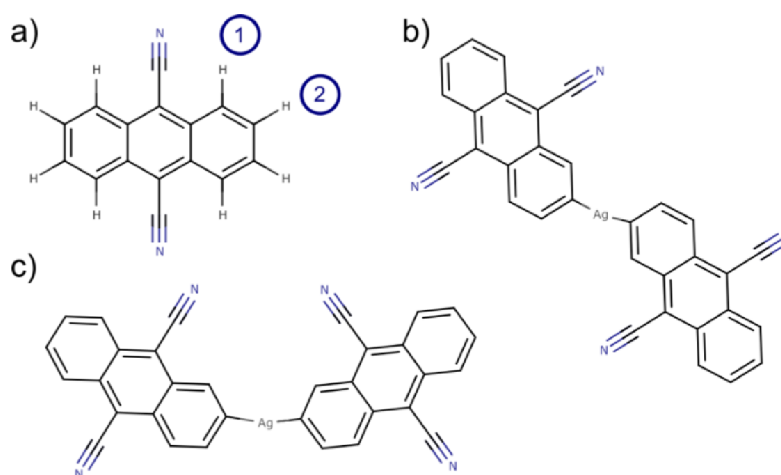
Figure 7: (a) DCA molecule with two symmetrically inequivalent hydrogens are labeled by their position. Covalently bound organometallic dimers in trans- and cis-positions are illustrated in b and c, respectively.

After finding out that the gold adatoms are in their atomic form, the analysis of the DCA molecules and possible pathways could begin. It was confirmed that the C-H bonds in positions 1 and 2 are equivalent, and no intrinsic regioselectivity is present. Dissociation onto the adatom exhibited the expected lowering of the barrier to approx. 50 kcal/mol, still too high for RT reaction and without a sign of regioselectivity. We subsequently considered the possibility of interaction of the adatoms with the edges of the DCA self-assembly islands. It was readily clear that additional lowering of the barrier was achieved by this approach to approx. 30 kcal/mol at a temperature of 0 K. By performing the MD simulations of free energy profiles at RT, we saw that the final barrier of C-H dissociation was lowered to 19 kcal/mol, already thermally accessible at RT. What is more, this reaction shows a clear preference for position 2 over position one, for which the barrier is almost twice as high due to steric hindrance and electrostatic repulsion. After a successful definition of the reaction pathway, we further analyzed the underlying mechanism for such dramatic catalytic and regioselective properties of single atom gold catalyst.

4.4.2. Article

Selective Activation of Aromatic C−H Bonds Catalyzed by Single Gold Atoms at Room Temperature

Benjamin Lowe, Jack Hellerstedt, Adam Matěj, Pingo Mutombo, Dhaneesh Kumar, Martin Ondráček, Pavel Jelinek,* and Agustin Schiffrin*

ACCESS | 📊 Metrics & More | 📄 Article Recommendations | 🆂ℹ Supporting Information

ABSTRACT: Selective activation and controlled functionalization of C−H bonds in organic molecules is one of the most desirable processes in synthetic chemistry. Despite progress in heterogeneous catalysis using metal surfaces, this goal remains challenging due to the stability of C−H bonds and their ubiquity in precursor molecules, hampering regioselectivity. Here, we examine the interaction between 9,10-dicyanoanthracene (DCA) molecules and Au adatoms on a Ag(111) surface at room temperature (RT). Characterization via low-temperature scanning tunneling microscopy, spectroscopy, and noncontact atomic force microscopy, supported by theoretical calculations, revealed the formation of organometallic DCA−Au−DCA dimers, where C atoms at the ends of the anthracene moieties are bonded covalently to single Au atoms. The formation of this organometallic compound is initiated by a regioselective cleaving of C−H bonds at RT. Hybrid quantum mechanics/molecular mechanics calculations show that this regioselective C−H bond cleaving is enabled by an intermediate metal−organic complex which significantly reduces the dissociation barrier of a specific C−H bond. Harnessing the catalytic activity of single metal atoms, this regioselective on-surface C−H activation reaction at RT offers promising routes for future synthesis of functional organic and organometallic materials.
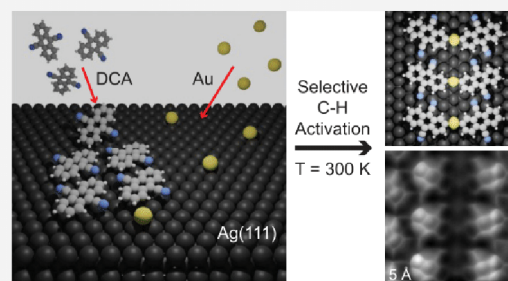
■ INTRODUCTION

The selective activation and controlled functionalization of C−H bonds in molecular precursors is one of the most important areas of synthetic organic chemistry for the design of C−C and C−heteroatom bonds in new compounds.[1−3] Controlled C−H activation reactions have enticing applications including natural gas transport,[2,4,5] polymer fabrication,[6−8] and late-stage modification of pharmaceutical products.[9−14] The high bond-dissociation enthalpy and ubiquity of C−H bonds, however, make their selective cleavage challenging.[1,15−17] In solution, enzymatic and transition metal (homogeneous) catalysis have provided avenues for the selective activation of C−H bonds.[7,18−21]

Solid metal surfaces have also been shown to exhibit (heterogeneous) catalytic activity on adsorbed molecules.[22−25] In particular, controlled activation of aromatic C−H bonds on a surface has enabled the synthesis of low-dimensional organic nanomaterials with promising electronic and magnetic properties, such as nanographenes,[26−29] graphene nanoribbons,[30−32] organic polymers,[33,34] and covalent organic frameworks.[35,36] However, broader application of on-surface C−H activation for the synthesis of functional materials remains limited due to high bond energies and poor regioselectivity.[37,38]

A common reaction used for on-surface design of aromatic C−C and C−heteroatom bonds is Ullmann-type coupling, where C−X bonds (X: halogen atom) in precursor molecules

undergo surface-catalyzed dehalogenation.[39] This approach has been successfully exploited for the fabrication of a range of different materials,[22−25,39] although the requirement for prehalogenation of targeted carbons in precursor molecules limits its applicability.

One promising approach for on-surface aromatic C−H activation consists of leveraging the catalytic activity of single metal adatoms. Single-atom catalysis yields promise for reducing the amount of precious metals used in heterogeneous catalysis.[40−43] In particular, despite its relative chemical inertness, gold has emerged as a promising single-atom catalyst (e.g., for the oxidation of carbon monoxide).[42−44] While Au surfaces have been used to catalyze the cleavage of C−H and C−X bonds,[38,45−47] sometimes resulting in the formation of organometallic C−Au bonds,[48−50] atomic-scale studies of single Au atom catalysis for C−H activation (on surfaces other than Au) have not yet been conducted.

Herein, we report the regioselective cleavage of an aromatic C−H bond of a cyano-functionalized anthracene derivative,

9,10-dicyanoanthracene (DCA; Figure 1a), activated by the interaction with single Au atoms on a Ag(111) surface at room
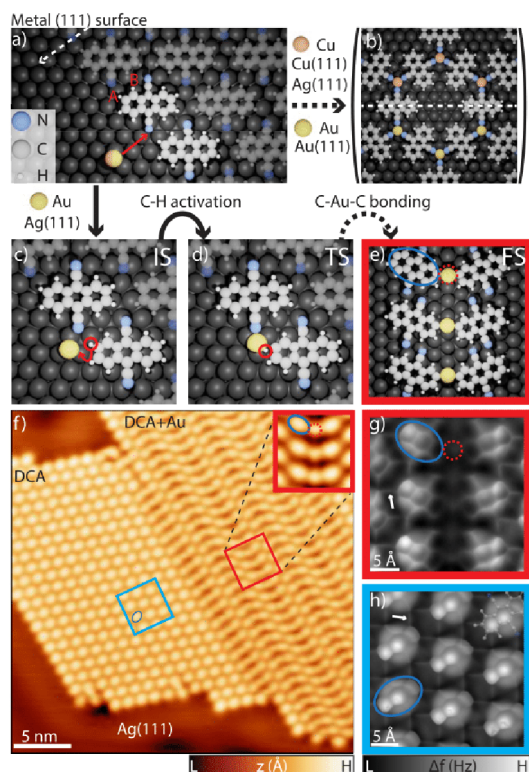

Figure 1. Interactions between noble metal adatoms and cyano-functionalized aromatic molecules on noble metal (111) surfaces: metal−cyano coordination vs covalent metal−carbon bonding. (a) Schematic of 9,10-dicyanoanthracene (DCA) molecules and metal adatoms (Cu or Au) on a (111) noble metal surface (Ag, Cu, or Au), with C−H positions A (anthracene end) and B (cyano adjacent) labeled. (b) The interaction between DCA and Cu adatoms on Ag(111) or on Cu(111), or with Au adatoms on Au(111), leads to formation of a 2D honeycomb-kagome metal−organic framework (MOF) via 3-fold rotationally symmetric metal−cyano coordination.[52−55,58] (c−e) The interaction between DCA and Au adatoms on Ag(111) gives rise to organometallic DCA−Au−DCA dimers via selective (position A) C−H activation and subsequent C−Au covalent bonding (IS: initial state, TS: transition state, FS: final state). (f) Constant-current STM image of self-assembled organic DCA-only (DCA) and DCA+Au domains featuring organometallic DCA−Au−DCA dimers on Ag(111) (V_b = −20 mV, I_t = 25 pA). Inset: high-resolution STM image (same tunneling parameters) of cis organometallic DCA−Au−DCA dimers within DCA+Au self-assembly. Solid blue ellipse: individual DCA molecule. Dashed red circle: Au adatom. (g, h) Constant-height ncAFM images (CO-tip; tip 30 pm closer to the sample with respect to STM set point V_b = 15 mV, I_t = 100 pA) of the DCA domain (blue box in f) and of three cis DCA−Au−DCA organometallic dimers in the DCA+Au domain (red box in f). White arrows indicate intermolecular N--H interactions.

temperature (RT). This selective activation of a specific C−H bond (located at the end of the anthracene group, labeled position A in Figure 1a) is mediated by the on-surface formation of an intermediate DCA−Au metal−organic complex, which subsequently enables selective dehydrogenation of the DCA molecule (Figure 1d). This results in a reactive site at the DCA anthracene extremity, which can then

covalently bond to a Au adatom and form organometallic DCA−Au−DCA dimers via a C−Au−C motif (Figure 1e). We used low-temperature scanning tunneling microscopy (STM) and spectroscopy (STS) as well as non-contact atomic force microscopy (ncAFM) to characterize the organometallic dimers at the atomic scale. The experimental findings are supported by density functional theory (DFT), ncAFM simulations, and quantum mechanics/molecular mechanics (QM/MM) calculations to shed light on the atomic structure and reaction mechanism. The low activation energy, indicated by the reaction occurring at RT, and regioselectivity of the observed C−H activation open the door to unexplored on-surface synthesis protocols based on single-atom catalysis for the development of functional and robust organic and organometallic materials.

■ RESULTS

We co-deposited DCA molecules and Au atoms from the gas phase in ultrahigh vacuum (UHV) onto a clean Ag(111) surface held at RT (see methods in the Supporting Information (SI) for further details). Figure 1f shows an STM image of a sample region following this preparation. We observe two types of well-ordered, two-dimensional (2D) periodic arrays of self-assembled adsorbates: (i) a purely organic domain (cyan box, region labeled DCA) consisting of identical elliptical protrusions (solid blue outline) corresponding to non-covalently bonded DCA molecules;[51] (ii) a domain consisting of parallel rows of pairs (red box, region labeled DCA+Au) of similar elliptical features (inset: solid blue outline) linked by circular protrusions (inset: red dashed circular outline). Based on their appearance and size, we identify the elliptical features in the DCA+Au domain as DCA molecules,[51] arranged in pairs in either cis (red box in Figure 1f) or trans configuration (see SI Figure S1). Approximately equal occurrences of cis- and trans-configuration were observed, though a quantitative statistical analysis is beyond the scope of this study.

The qualitative difference in Figure 1f between the previously reported[51] DCA domain and the DCA+Au domain consisting of ordered DCA pairs is a strong suggestion that the pairing of DCA molecules in the latter is mediated by the interaction between DCA and Au adatoms. Notably, these results are also qualitatively different from previously studied surface-supported systems where 3-fold rotationally symmetric metal−ligand coordination between DCA cyano groups and noble metal adatoms [e.g., Cu adatoms on Cu(111),[52−54] Ag(111),[55] Ir(111)-supported graphene,[56] and NbSe$_2$;[57] Au adatoms on Au(111)][58] give rise to porous, 2D honeycomb-kagome metal−organic frameworks (MOFs) as shown in Figure 1b. This is a strong indication that the interaction between DCA and Au adatoms on Ag(111) is fundamentally different than in these other systems.

We used ncAFM with a carbon monoxide (CO)-function-alized tip (see methods in the SI) to gain further insight into the intramolecular structure of the Au-mediated DCA pairs. NcAFM imaging of the DCA+Au domain, Figure 1g, and the DCA domain,[51] Figure 1h, are similar in that the submolecular structure of individual DCA molecules is clearly resolved in agreement with the overlaid chemical structure in Figure 1h, with noncovalent attractive N--H interactions (Figure 1 white arrows) between adjacent molecules (DCA) or molecule pairs (DCA+Au).[59]

In contrast with ncAFM imaging of the DCA domain in Figure 1h where the frequency shift (Δf) across each of the

DCA benzene rings is relatively uniform, individual DCA molecules in the DCA+Au domain, Figure 1g, exhibit reduced Δf at the benzene rings closest to the DCA pair center (near the location of the circular protrusion in STM imaging; red dashed circle). Such ncAFM appearance of π-conjugated rings is indicative of direct coordination between atoms of the aromatic group and a metal adatom,[60−63] further supporting the involvement of Au adatoms within the DCA+Au domain.

We conducted lateral STM manipulation to further probe the nature of the intra- and inter-DCA pair interactions within the DCA+Au assembly. Figure 2a shows an STM image of a
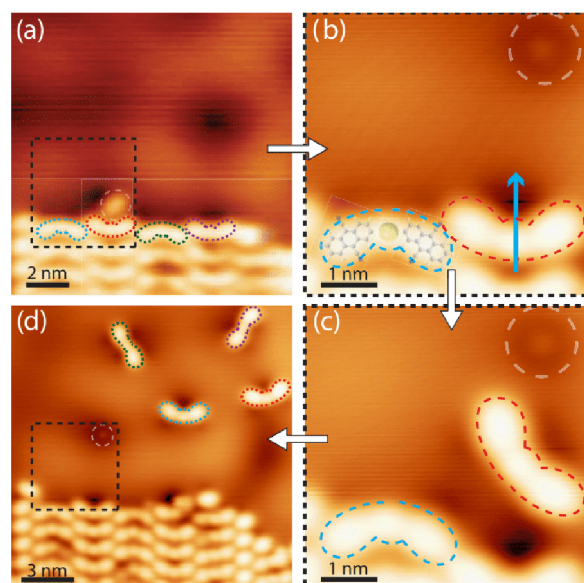

Figure 2. Deconstruction of organometallic DCA+Au self-assembly on Ag(111) via lateral STM manipulation. (a−d) Constant-current STM images showing manipulation of single DCA−Au−DCA units from the cis DCA+Au domain [images: V_b = −20 mV, I_t = 10 pA; manipulation: V_b = −10 mV, I_t = 14 nA for removal of DCA dimers from 2D film, V_b = −10 mV, I_t = 5 nA for subsequent translation on Ag(111)]. Blue arrow indicates STM tip path during manipulation. Dashed black square in (a) and (d) indicates region in (b) and (c). Dashed outlines indicate manipulated DCA−Au−DCA units. White dashed circles indicate defect adsorbate displaced during manipulation. Ball-and-stick model of DCA−Au−DCA dimer chemical structure overlaid in (b).

DCA+Au domain with cis-configuration DCA pairs. Individual DCA pairs, consisting of two elliptical features connected via a circular feature in the STM images, could be reproducibly removed from the edge of a DCA+Au domain and manipulated about the surface (Figure 2b−d). Upon manipulation, the STM appearance of the DCA pairs is unchanged, suggesting that their chemical structure is preserved.

In some instances, we observed switching from the cis- to the trans-configuration upon manipulation (dashed green and purple pairs in Figure 2). We did not, however, observe evidence of such switching under normal tunneling conditions (through, e.g., telegraph noise[64]); cis- and trans-configurations were both otherwise stable during characterization.

Within the range of STM manipulation parameters tested, we were unable to observe further breaking of the DCA pairs into their individual constituents (i.e., STM elliptical features

corresponding to DCA molecules and circular features). From this, we conclude that while lateral manipulation can overcome the strength of bonding between adjacent DCA pairs, it cannot overcome the interaction connecting the two DCA molecules within such pairs. This suggests the intrapair interaction is significantly stronger than the interpair interaction and that the Au-mediated DCA pairs are highly stable.

From these STM manipulation observations, combined with the reduced frequency shift of the benzene rings near the DCA pair center (Figures 1f, 3c), we propose that the DCA pairs
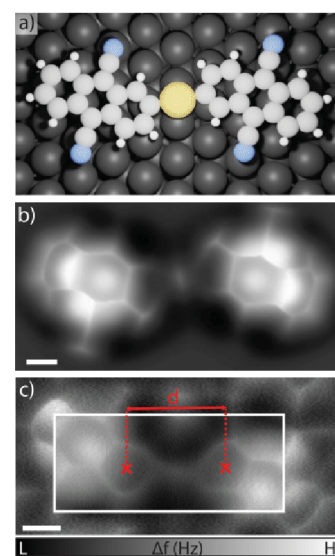
Figure 3. Experimental and theoretical submolecular structure of a trans DCA−Au−DCA pair on Ag(111). (a) Ball-and-stick model of DFT-relaxed structure. (b) Simulated ncAFM image of the optimized structure in (a). (c) Constant-height (CO-tip) ncAFM image (tip 30 pm closer to the sample with respect to STM set point V_b = 15 mV, I_t = 100 pA). Inset in white box is a higher resolution image taken with the tip 40 pm closer to the surface with respect to the same STM set point (see methods in the SI). Red arrow indicates distance, d, between the centers of the benzene rings closest to the Au atom of each DCA molecule involved in an organometallic pair. Simulated image in (b): d_{sim} = 5.72 ± 0.06 Å. Experimental image in (c): d_{exp} = 6.0 ± 0.2 Å. Scale bars: 2.5 Å.

consist of an organometallic DCA−Au−DCA motif, wherein a position A (Figure 1a) carbon atom of each of the two DCA molecules is covalently bonded to a Au atom (Figure 1e). The observation of cis- and trans-configurations can be attributed to the chemical equivalence of the two carbon atoms at the anthracene ends of the DCA molecule.

We performed DFT calculations to rationalize the proposed organometallic structure. The energetically favorable atomic structure of an organometallic trans DCA−Au−DCA dimer on Ag(111), optimized via DFT (see methods in the SI), is shown in Figure 3a. The DFT calculations revealed a negligible energy difference between the trans- and cis-configurations (see SI Figure S2), supporting the observation of the two configurations in approximately equal measure, and the cis-to-trans conversion by STM manipulation.

The simulated ncAFM image (Figure 3b; obtained via the probe-particle method[65]) corresponding to the DFT-relaxed DCA−Au−DCA dimer in Figure 3a shows strong qualitative agreement with the experimental ncAFM image (Figure 3c),

including the reduced Δf of the benzene rings closest to the C−Au−C bonding motif at the DCA pair center. The simulated and experimental image also have a similar distance d between the centers of the benzene rings closest to the Au atom (5.72 ± 0.06 Å for the simulated images and 6.0 ± 0.2 Å for the experimental images). We rule out a DCA−DCA pair with a direct covalent C−C bond between facing anthracene groups, since ncAFM simulations of this structure would result in a distance d (4.76 ± 0.06 Å) significantly shorter than that observed experimentally and would not reproduce the experimentally observed reduced Δf in the benzene rings closest to the DCA−DCA linkage (Figure S3).

We performed dI/dV STS to gain insight into the electronic structure of an individual DCA−Au−DCA dimer. The spectra in Figure 4a were acquired on the Au (orange) and outer (i.e., furthest from Au site) anthracene end (blue) sites of a trans DCA−Au−DCA dimer, removed from the 2D assembly via manipulation. Both orange and blue spectra show a step-like
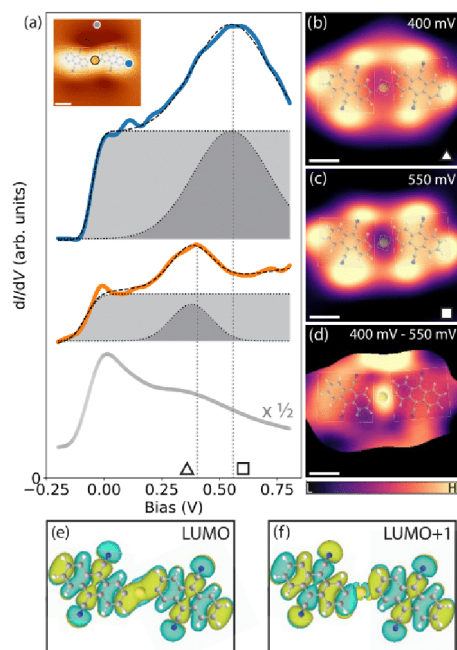
feature at ∼−66 mV and a peak at ∼376 and ∼560 mV, respectively.

We attribute the step-like feature to the Shockley surface state of Ag(111),[66] and the two peaks to intrinsic electronic states of the DCA−Au−DCA unit. Figure 4b,c show dI/dV maps associated with each of these electronic states. Both maps show significant intensity at the anthracene ends furthest from the Au site and at the cyano groups. These features are qualitatively similar to the spatial distribution of the DCA lowest unoccupied molecular orbital (LUMO).[51,67] The map in Figure 4b also shows some dI/dV intensity at the Au site, significantly more so than Figure 4c (emphasized in the difference between Figure 4b and c, displayed in Figure 4d).

Figure 4e,f show the DFT-calculated spatial distribution of the LUMO and LUMO+1 of the structurally optimized gas-phase DCA−Au−DCA dimer (see methods and Figure S4 in the SI). These DFT-calculated LUMO and LUMO+1 are separated in energy by ∼100 meV, of the same order of magnitude as the ∼184 meV energy difference between experimental dI/dV peaks in Figure 4a. Both the calculated LUMO and LUMO+1 have predominantly DCA orbital character (see Figure S4 and Figure S5), with intensity at the anthracene ends furthest from the Au site and at the cyano groups. The LUMO (Figure 4e) shows intensity at the Au atom, whereas the LUMO+1 (Figure 4f) exhibits a nodal plane at this site perpendicular to the DCA−DCA axis. The calculated LUMO and LUMO+1 are in qualitative agreement with the experimental dI/dV maps in Figure 4b and c, respectively. This agreement provides further evidence that the DCA+Au self-assembled 2D domain in Figure 1f consists of organometallic DCA−Au−DCA dimers, in which the position A carbon atoms are covalently bonded to a Au atom.

The organometallic DCA−Au−DCA structure is qualitatively different from previously observed 2D MOFs consisting of DCA molecules coordinated with metal atoms via their cyano groups.[52−58] Moreover, the formation of the organometallic DCA−Au−DCA motif requires highly regioselective cleavage of the position A aromatic C−H bonds to enable the C−Au−C covalent bonding. Such C−H bonds have large dissociation enthalpies,[60,68,69] ΔH, meaning their cleavage seldom occurs at RT,[70] and they often suffer from poor regioselectivity.[25,38,60,68,69] For a gas-phase DCA molecule for instance, we calculated ΔH values of 112.1 and 113.2 kcal/mol (4.86 and 4.91 eV) via DFT for the aromatic C−H bonds at positions A and B, respectively (see Figure 1a and SI Figure S7).

In the following, we rationalize the highly selective C−H activation reaction (and subsequent DCA−Au−DCA formation) at RT via DFT and QM/MM calculations. First, we found using DFT that Au adatoms on Ag(111) retain their neutral, atomic-like character (SI Figure S6). This contrasts with the case of Au adatoms on Au(111), where significant electronic hybridization between adatom and the surface takes place. That is, Au adatoms are less coordinated and arguably more reactive on Ag(111) than on Au(111), providing an explanation for the differences between organometallic (covalent C−Au bonding) and metal−organic[58] (N--Au) coordination complexes (Figure 1).

We then conducted QM/MM calculations of Gibbs free energy differences, ΔG, on a system composed of a single DCA molecule with a single Au adatom in proximity on Ag(111) (system 1; see Figures 5b and S7). We considered a C−H bond dissociation mechanism mediated by the direct

Figure 4. Electronic properties of the DCA−Au−DCA organometallic unit. (a) dI/dV scanning tunneling spectra obtained at sites indicated in the inset (set point: V_b = −200 mV, I_t = 20 pA). Black dashed curves: fits of experimental data consisting of an error function (step-like feature, light gray shaded area) and a Gaussian peak (dark gray). An exponential function accounting for tunneling transmission was also included in the fit for the orange curve. Silver reference spectrum (gray curve) scaled down by a factor of 2. Vertical dotted gray lines indicate bias voltages at which dI/dV maps in (b) and (c) were acquired. Inset: constant-current STM image of the DCA−Au−DCA unit (V_b = −20 mV, I_t = 50 pA). (b, c) Constant-current dI/dV maps of the DCA−Au−DCA unit (I_t = 500 pA) at V_b = 400 and 550 mV. (d) Subtraction between dI/dV maps in (b) and (c) for a region corresponding to the DCA−Au−DCA unit. DCA−Au−DCA chemical structure overlaid for reference in (a) inset and (b)−(d). Scale bars: 5 Å. We isolated the single DCA−Au−DCA unit from a DCA+Au self-assembled 2D organometallic domain via lateral STM manipulation. (e, f) Wave function isosurfaces (0.005 Å$^{-3/2}$; green: positive; blue: negative) for LUMO and LUMO+1 of the gas-phase trans DCA−Au−DCA pair calculated by DFT.
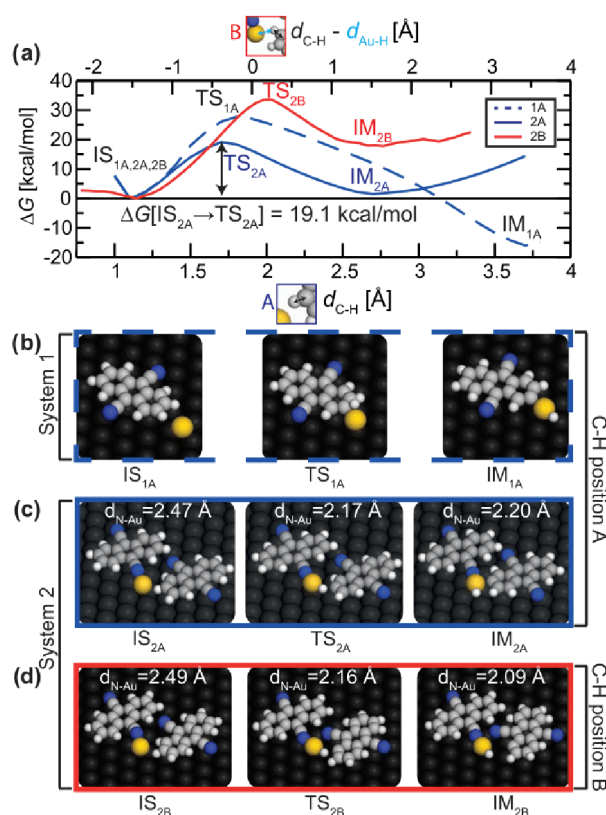
Figure 5. Pathways for Au-induced C–H cleavage of a DCA molecule on Ag(111). (a) Gibbs free energy differences, ΔG, calculated via QM/MM simulations at $T = 300$ K, for different C–H bond dissociation pathways in a system comprised of a single DCA molecule and a single Au adatom (system 1 in b; dashed curve) and in a system comprised of 2 DCA molecules and a single Au adatom (system 2 in c, d; solid curves). For position A (blue curves), we considered the C–H bond length d_{C-H} (bottom axis) as the reaction coordinate; for position B (red curve), we considered the difference $(d_{C-H} - d_{Au-H})$ (top axis) between the C–H bond length and Au–H distance as the reaction coordinate (computationally necessary for this pathway). Activation energy [ΔG between transition (TS) and initial (IS) states] for C–H bond dissociation is reduced for position A in system 2, $\Delta G[IS_{2A} \rightarrow TS_{2A}] = 19.1$ kcal/mol (0.83 eV). (b–d) Ball-and-stick models of IS, TS, and intermediate (IM) states for C–H bond (positions A and B) dissociation pathways in systems 1 (b) and 2 (c, d).

interaction between Au and H at $T = 300$ K ($\sim$RT to match our experimental conditions; see Figures S7 and S8 for calculations at $T = 0$ K). The dashed blue curve in Figure 5a shows the calculated ΔG as a function of position A C–H distance, d_{C-H}, when system 1 evolves from an initial state IS_{1A} to a transition state TS_{1A} then to an intermediate state IM_{1A} (where H becomes bonded to Au; Figure 5b). These calculations yielded an activation energy $\Delta G[IS_{1A} \rightarrow TS_{1A}] = 27.7$ kcal/mol (1.20 eV). We claim that this energy is too high to explain the dissociation of an anthracene C–H bond at RT. Note that similar calculations performed for the position B C–H bond in system 1 suggest an even higher dissociation barrier (Figure S7).

Therefore, we also considered a system composed of two DCA molecules and a single Au adatom on Ag(111) (system 2; Figures 5c and S8), with a configuration similar to that at

the edges of self-assembled DCA-only domains (Figures 1a and S14).[51] We suggest that Au atoms diffusing on the surface may encounter supramolecular DCA islands rather than isolated molecules (Figures S14 and S15). This is supported by the fact that, experimentally, we observed DCA–Au–DCA dimers both when DCA and Au were deposited sequentially (DCA first) or simultaneously (see methods in the SI). Furthermore, we did not observe any DCA+Au domains that were surrounded by DCA-only domains. Based on this, we considered the possibility that N--Au coordination could give rise to a metal–organic DCA(N)--Au complex (see initial states IS_{2A} or IS_{2B} in Figure 5c,d) at the edges of DCA-only domains and conducted QM/MM simulations to investigate whether this geometry could facilitate C–H activation at an adjacent molecule. The solid blue curve in Figure 5a shows $\Delta G(T = 300$ K) as a function of position A C–H distance, d_{C-H}, for system 2 as it evolves from IS_{2A} to an intermediate state IM_{2A} via a transition state TS_{2A} (Figure 5c). Here, we found a position A C–H activation energy $\Delta G[IS_{2A} \rightarrow TS_{2A}] = 19.1$ kcal/mol (0.83 eV), significantly smaller than $\Delta G[IS_{1A} \rightarrow TS_{1A}]$.

Similarly, the red curve in Figure 5a corresponds to $\Delta G(T = 300$ K) as a function of $d_{C-H} - d_{Au-H}$ for the position B C–H bond, for the same system 2, evolving from IS_{2B} to TS_{2B} to IM_{2B} (Figure 5d). Here, the activation barrier $\Delta G[IS_{2B} \rightarrow TS_{2B}]$ for the position B C–H bond is 33.6 kcal/mol (1.46 eV), significantly larger than $\Delta G[IS_{2A} \rightarrow TS_{2A}]$. Based on these QM/MM calculations, the dissociation barrier of the position A C–H bonds is significantly lowered via interaction with a DCA(N)--Au metal–organic complex, enabling highly regioselective C–H bond cleavage at RT.

■ DISCUSSION

To gain more insight into the regioselective lowering of the activation energy of the C–H cleavage, we analyzed the electronic structure of the DCA(N)--Au complex (present in IS_{2A}) using DFT [Figure S10b]. These calculations indicate a weak, purely electrostatic interaction between Au and the cyano group, with no evidence of strong hybridization and with an interaction energy of 4.2 kcal/mol (0.18 eV) and a N--Au distance of 2.47 Å. This interaction with the cyano group results in a local polarization around and charge redistribution within the Au atom, with an electron depletion on the outside of the Au atom along the Au–cyano axis (Figure S10d). This depleted electron density can reduce the Pauli repulsion between Au and a H atom of an adjacent DCA, facilitating the formation of a Au–H chemical bond and of a DCA(H)–Au--(N)DCA complex (see IM_{2A} in Figure 5c). This partially explains the significant lowering of the C–H bond activation energy.

Our DFT calculations also show that, in IM_{2A} (Figure 5), covalent Au–H bonding is concomitant with hybridization of Au 6s and 5d orbitals, giving rise to two hybrid sd orbitals along the N--Au–H axis (see SI Section S9, Figures S9–S13), and with electron transfer from Au to H (Figure S12). The resulting partial positive charge on Au strengthens the electrostatic interaction with the partially negatively charged cyano group (Figure S11), causing an increase in the Au--(N)DCA interaction energy of $\sim$22 kcal/mol ($\sim$0.95 eV) and a reduction of the Au--N bond length by $\sim$0.27 Å.

To understand how this change in Au--(N)DCA interaction energy influences the C–H cleavage activation barrier, it is

pertinent to consider the transition state TS_{2A} (Figure 5). Here, DFT calculations show a Au--(N)DCA interaction energy of 26.0 kcal/mol (1.13 eV) with a Au--N bond length of 2.17 Å, indicating a much stronger interaction than in IS_{2A}. This synergistic effect therefore contributes further to the significant lowering of the activation energy of the C−H cleavage at position A.

Moreover, we claim that, for the position B C−H bond (Figure 5d), this effect is offset by steric hindrance and repulsion between cyano groups of adjacent DCA molecules, contributing to a significantly larger dissociation barrier $\Delta G[IS_{2B} \rightarrow TS_{2B}]$.

For TS_{2A}, we calculated via DFT a C−H stretching mode in the direction of the C−H dissociation with an eigenfrequency of 611.5 cm^{-1}. Using this value, we calculated for position A (with a dissociation barrier of 19 kcal/mol) at RT an Arrhenius[71] C−H dissociation rate constant of 0.23 s^{-1}. By contrast, the RT Arrhenius dissociation rate constant for the position B C−H bond (with a dissociation barrier of 33.6 kcal/mol) is 1.4×10^{-12} s^{-1}. We claim that this significant difference between positions A and B explains the experimentally observed regioselectivity of the C−H dissociation. The 19 kcal/mol barrier represents a significant reduction relative to comparable C−H activation reactions with barriers of 30−40 kcal/mol (1.3−1.8 eV), experimentally occurring in a temperature window of 400−700 K.[60,68,69,72] Furthermore, other on-surface reactions with barriers of ∼20 kcal/mol (∼0.87 eV) have been observed at RT,[71,73] supporting the interpretation of our experimental results as RT C−H activation.

Although our DFT and QM/MM calculations rationalize the regioselective cleaving of position A C−H bonds at RT, they do not explain the pathway from IM_{2A} (Figure 5) to the experimentally observed organometallic DCA−Au−DCA motif (where C bonds covalently to Au). In the following, we provide a tentative, qualitative scenario for such a pathway. We propose that, at RT, the hydrogen atom in DCA(N)--Au−H in IM_{2A} (Figure 5c) is likely to detach, bind to Ag(111), and then desorb (see SI Section S10), leaving organometallic DCA(C)−Au on Ag(111), which can diffuse on the surface and potentially react with another dehydrogenated DCA$^\bullet$ radical, forming the experimentally observed DCA−Au−DCA unit. Noncovalent N--H bonds between neighboring DCA−Au−DCA dimers may contribute to stabilizing the DCA−Au−DCA dimer rows as seen in the DCA+Au domain in Figure 1f. The relatively weak and reversible DCA(N)--Au interaction, combined with the reactivity of the DCA$^\bullet$ radical, might explain why we did not experimentally observe any of the metal−organic DCA(N)--Au species such as in IS_{2A} or IM_{2A} in Figure 5. A quantitative theoretical description of this process would require the consideration of many possible reaction pathways (including, for example, surface diffusion, dynamic equilibrium of different phases) in a system composed of many DCA molecules, Au adatoms, and DCA−Au complexes; this is beyond the scope of this work.

At $T = 0$ K, QM/MM calculations suggest that the energies involved in the dissociation of a position A C−H bond in a DCA−Au−DCA dimer (by interacting with a DCA(N)---Au-H complex; see SI Figure S16) are approximately twice as large as that for a position A C−H bond in a single DCA molecule. This explains the observation of discrete DCA−Au−DCA dimers and the absence of 1D −[DCA−Au−DCA−Au]− organometallic chains.

We claim that the key difference between the previously observed DCA−Cu honeycomb-kagome MOF on Ag(111)[55] and the present study on the organometallic DCA−Au motif is the strength of the metal adatom−cyano interaction. For Cu--N, DFT calculations revealed an interaction energy of ∼18.5 kcal/mol (∼0.8 eV), significantly larger than the aforementioned value of 4.2 kcal/mol for Au−N in IS_{2A} (Figure 5c). This favors 3-fold Cu-ligand coordination and Cu-based MOF formation, preventing the reaction pathway for C−H bond activation and organometallic bonding as is the case for Au.

■ CONCLUSION

We have experimentally observed the formation of organometallic DCA−Au−DCA dimers on a Ag(111) surface at RT. In these dimers, C atoms located specifically at the extremity of the DCA molecule anthracene moiety (position A) bond covalently to a Au adatom. These observations, supported by DFT, indicate the regioselective C−H bond activation triggered by Au adatoms at RT. Our QM/MM calculations show that this reaction is mediated by the interaction with an intermediate DCA(N)--Au−H metal−organic complex, which significantly reduces the activation barrier of a specific C−H bond. Our work provides atomic-scale insight into selective C−H bond activation, catalyzed by single noble metal atoms and intermediate metal−organic complexes at RT. Our findings have the potential to contribute to addressing the large demand for the synthesis of fuel, fine chemicals, and functional organic and organometallic materials. Further investigations could explore such protocols on surfaces or host materials beyond noble metals.

■ ASSOCIATED CONTENT

ⓢ Supporting Information

The Supporting Information is available free of charge at https://pubs.acs.org/doi/10.1021/jacs.2c10154.

> Experimental and theoretical methods; structural characterization of DCA+Au domains; DFT-optimized structures; further ncAFM simulations; electronic properties of DCA+Au dimers; Au adatom character on Ag(111); QM/MM calculations at $T = 0$ K; hybridization and charge distribution across reaction pathway; tentative organometallic dimer formation pathway; secondary C−H activation QM/MM calculations (PDF)

■ AUTHOR INFORMATION

Corresponding Authors

Pavel Jelinek − *Institute of Physics, Academy of Sciences of the Czech Republic, 162 00 Prague, Czech Republic; Regional Centre of Advanced Technologies and Materials, Czech Advanced Technology and Research Institute (CATRIN), Palacký University Olomouc, 779 00 Olomouc, Czech Republic;* ⊙ orcid.org/0000-0002-5645-8542; Email: jelinekp@fzu.cz

Agustin Schiffrin − *School of Physics and Astronomy, Monash University, Clayton, Victoria 3800, Australia; ARC Centre of Excellence in Future Low-Energy Electronics Technologies, Monash University, Clayton, Victoria 3800, Australia;* ⊙ orcid.org/0000-0003-1140-8485; Email: agustin.schiffrin@monash.edu

Authors

Benjamin Lowe − *School of Physics and Astronomy, Monash University, Clayton, Victoria 3800, Australia; ARC Centre of Excellence in Future Low-Energy Electronics Technologies, Monash University, Clayton, Victoria 3800, Australia;* orcid.org/0000-0002-5157-7737

Jack Hellerstedt − *School of Physics and Astronomy, Monash University, Clayton, Victoria 3800, Australia; ARC Centre of Excellence in Future Low-Energy Electronics Technologies, Monash University, Clayton, Victoria 3800, Australia;* orcid.org/0000-0003-2282-8223

Adam Matěj − *Institute of Physics, Academy of Sciences of the Czech Republic, 162 00 Prague, Czech Republic; Regional Centre of Advanced Technologies and Materials, Czech Advanced Technology and Research Institute (CATRIN), Palacký University Olomouc, 779 00 Olomouc, Czech Republic; Department of Physical Chemistry, Faculty of Science, Palacký University Olomouc, 771 46 Olomouc, Czech Republic*

Pingo Mutombo − *Institute of Physics, Academy of Sciences of the Czech Republic, 162 00 Prague, Czech Republic*

Dhaneesh Kumar − *School of Physics and Astronomy, Monash University, Clayton, Victoria 3800, Australia; ARC Centre of Excellence in Future Low-Energy Electronics Technologies, Monash University, Clayton, Victoria 3800, Australia;* orcid.org/0000-0002-5333-6283

Martin Ondráček − *Institute of Physics, Academy of Sciences of the Czech Republic, 162 00 Prague, Czech Republic;* orcid.org/0000-0002-8808-1487

Complete contact information is available at:
https://pubs.acs.org/10.1021/jacs.2c10154

Author Contributions

B.L., J.H., and A.M. contributed equally to this work.

Notes

The authors declare no competing financial interest.

■ REFERENCES

(1) Arndtsen, B. A.; Bergman, R. G.; Mobley, T. A.; Peterson, T. H. Selective Intermolecular Carbon-Hydrogen Bond Activation by Synthetic Metal Complexes in Homogeneous Solution. *Acc. Chem. Res.* **1995**, *28*, 154−162.

(2) Labinger, J. A.; Bercaw, J. E. Understanding and exploiting C−H bond activation. *Nature* **2002**, *417*, 507−514.

(3) Godula, K.; Sames, D. C-H. Bond Functionalization in Complex Organic Synthesis. *Science* **2006**, *312*, 67−72.

(4) Crabtree, R. H. Alkane C−H activation and functionalization with homogeneous transition metal catalysts: a century of progress—a new millennium in prospect. *J. Chem. Soc., Dalton Trans.* **2001**, 2437−2450.

(5) Schwach, P.; Pan, X.; Bao, X. Direct Conversion of Methane to Value-Added Chemicals over Heterogeneous Catalysts: Challenges and Prospects. *Chem. Rev.* **2017**, *117*, 8497−8520.

(6) Blaskovits, J. T.; Leclerc, M. C-H. Activation as a Shortcut to Conjugated Polymer Synthesis. *Macromol. Rapid Commun.* **2019**, *40*, 1800512.

(7) Yang, Y.; Nishiura, M.; Wang, H.; Hou, Z. Metal-catalyzed CH activation for polymer synthesis and functionalization. *Coord. Chem. Rev.* **2018**, *376*, 506−532.

(8) Zhang, J.; Kang, L. J.; Parker, T. C.; Blakey, S. B.; Luscombe, C. K.; Marder, S. R. Recent Developments in C−H Activation for Materials Science in the Center for Selective C−H Activation. *Molecules* **2018**, *23*, 922.

(9) Dai, H.-X.; Stepan, A. F.; Plummer, M. S.; Zhang, Y.-H.; Yu, J.-Q. Divergent C−H Functionalizations Directed by Sulfonamide Pharmacophores: Late-Stage Diversification as a Tool for Drug Discovery. *J. Am. Chem. Soc.* **2011**, *133*, 7222−7228.

(10) Jana, R.; Begam, H. M.; Dinda, E. The emergence of the C-H functionalization strategy in medicinal chemistry and drug discovery. *Chem. Commun. (Camb)* **2021**, *57*, 10842−10866.

(11) Wencel-Delord, J.; Glorius, F. C−H bond activation enables the rapid construction and late-stage diversification of functional molecules. *Nat. Chem.* **2013**, *5*, 369−375.

(12) Zhang, L.; Ritter, T. A Perspective on Late-Stage Aromatic C−H Bond Functionalization. *J. Am. Chem. Soc.* **2022**, *144*, 2399−2414.

(13) Cernak, T.; Dykstra, K. D.; Tyagarajan, S.; Vachal, P.; Krska, S. W. The medicinal chemist's toolbox for late stage functionalization of drug-like molecules. *Chem. Soc. Rev.* **2016**, *45*, 546−576.

(14) Yamaguchi, J.; Yamaguchi, A. D.; Itami, K. C-H Bond Functionalization: Emerging Synthetic Tools for Natural Products and Pharmaceuticals. *Angew. Chem., Int. Ed.* **2012**, *51*, 8960−9009.

(15) Dutta, U.; Maiti, S.; Bhattacharya, T.; Maiti, D. Arene diversification through distal C(sp2)-H functionalization. *Science* **2021**, *372*, No. eabd5992.

(16) Ramadoss, B.; Jin, Y.; Asako, S.; Ilies, L. Remote steric control for undirected meta-selective C-H activation of arenes. *Science* **2022**, *375*, 658−663.

(17) Xue, X.-S.; Ji, P.; Zhou, B.; Cheng, J.-P. The Essential Role of Bond Energetics in C−H Activation/Functionalization. *Chem. Rev.* **2017**, *117*, 8622−8648.

(18) Tiwari, V. K.; Kapur, M. Catalyst-controlled positional-selectivity in C−H functionalizations. *Org. Biomol. Chem.* **2019**, *17*, 1007−1026.

(19) Shilov, A. E.; Shul'pin, G. B. Activation of C-H Bonds by Metal Complexes. *Chem. Rev.* **1997**, *97*, 2879−2932.

(20) Labinger, J. A. Platinum-Catalyzed C−H Functionalization. *Chem. Rev.* **2017**, *117*, 8483−8496.

(21) Lewis, J. C.; Coelho, P. S.; Arnold, F. H. Enzymatic functionalization of carbon−hydrogen bonds. *Chem. Soc. Rev.* **2011**, *40*, 2003−2021.

(22) Clair, S.; de Oteyza, D. G. Controlling a Chemical Coupling Reaction on a Surface: Tools and Strategies for On-Surface Synthesis. *Chem. Rev.* **2019**, *119*, 4717−4776.

(23) Fan, Q.; Gottfried, J. M.; Zhu, J. Surface-Catalyzed C−C Covalent Coupling Strategies toward the Synthesis of Low-Dimensional Carbon-Based Nanostructures. *Acc. Chem. Res.* **2015**, *48*, 2484−2494.

(24) Grill, L.; Hecht, S. Covalent on-surface polymerization. *Nat. Chem.* **2020**, *12*, 115−130.

(25) Held, P. A.; Fuchs, H.; Studer, A. Covalent-Bond Formation via On-Surface Chemistry. *Chemistry − A European Journal* **2017**, *23*, 5874−5892.

(26) Mishra, S.; Beyer, D.; Eimre, K.; Kezilebieke, S.; Berger, R.; Gröning, O.; Pignedoli, C. A.; Müllen, K.; Liljeroth, P.; Ruffieux, P.; Feng, X.; Fasel, R. Topological frustration induces unconventional magnetism in a nanographene. *Nat. Nanotechnol.* **2020**, *15*, 22–28.

(27) Mishra, S.; Beyer, D.; Eimre, K.; Ortiz, R.; Fernandez-Rossier, J.; Berger, R.; Groening, O.; Pignedoli, C. A.; Fasel, R.; Feng, X.; Ruffieux, P. Collective All-Carbon Magnetism in Triangulene Dimers. *Angew. Chem., Int. Ed.* **2020**, *59*, 12041–12047.

(28) Pavliček, N.; Mistry, A.; Majzik, Z.; Moll, N.; Meyer, G.; Fox, D. J.; Gross, L. Synthesis and characterization of triangulene. *Nat. Nanotechnol.* **2017**, *12*, 308–311.

(29) Su, J.; et al. Atomically precise bottom-up synthesis of Pi-extended [5]triangulene. *Science Advances* **2019**, *5*, 7717.

(30) Cai, J.; Ruffieux, P.; Jaafar, R.; Bieri, M.; Braun, T.; Blankenburg, S.; Muoth, M.; Seitsonen, A. P.; Saleh, M.; Feng, X.; Müllen, K.; Fasel, R. Atomically precise bottom-up fabrication of graphene nanoribbons. *Nature* **2010**, *466*, 470–473.

(31) Rizzo, D. J.; Veber, G.; Cao, T.; Bronner, C.; Chen, T.; Zhao, F.; Rodriguez, H.; Louie, S. G.; Crommie, M. F.; Fischer, F. R. Topological band engineering of graphene nanoribbons. *Nature* **2018**, *560*, 204–208.

(32) Ruffieux, P.; Wang, S.; Yang, B.; Sánchez-Sánchez, C.; Liu, J.; Dienel, T.; Talirz, L.; Shinde, P.; Pignedoli, C. A.; Passerone, D.; Dumslaff, T.; Feng, X.; Müllen, K.; Fasel, R. On-surface synthesis of graphene nanoribbons with zigzag edge topology. *Nature* **2016**, *531*, 489–492.

(33) Cirera, B.; Sánchez-Grande, A.; de la Torre, B.; Santos, J.; Edalatmanesh, S.; Rodríguez-Sánchez, E.; Lauwaet, K.; Mallada, B.; Zbořil, R.; Miranda, R.; Gröning, O.; Jelínek, P.; Martín, N.; Ecija, D. Tailoring topological order and Pi- conjugation to engineer quasi-metallic polymers. *Nat. Nanotechnol.* **2020**, *15*, 437–443.

(34) Sánchez-Grande, A.; de la Torre, B.; Santos, J.; Cirera, B.; Lauwaet, K.; Chutora, T.; Edalatmanesh, S.; Mutombo, P.; Rosen, J.; Zbořil, R.; Miranda, R.; Björk, J.; Jelínek, P.; Martín, N.; Écija, D. On-Surface Synthesis of Ethynylene-Bridged Anthracene Polymers. *Angew. Chem., Int. Ed.* **2019**, *58*, 6559–6563.

(35) Galeotti, G.; et al. Synthesis of mesoscale ordered two-dimensional Pi-conjugated polymers with semiconducting properties. *Nat. Mater.* **2020**, *19*, 874–880.

(36) Springer, M. A.; Liu, T.-J.; Kuc, A.; Heine, T. Topological two-dimensional polymers. *Chem. Soc. Rev.* **2020**, *49*, 2007–2019.

(37) Fan, Q.; Werner, S.; Tschakert, J.; Ebeling, D.; Schirmeisen, A.; Hilt, G.; Hieringer, W.; Gottfried, J. M. Precise Monoselective Aromatic C—H Bond Activation by Chemisorption of Meta-Aryne on a Metal Surface. *J. Am. Chem. Soc.* **2018**, *140*, 7526–7532.

(38) Li, Q.; Yang, B.; Lin, H.; Aghdassi, N.; Miao, K.; Zhang, J.; Zhang, H.; Li, Y.; Duhm, S.; Fan, J.; Chi, L. Surface-Controlled Mono/Diselective ortho C—H Bond Activation. *J. Am. Chem. Soc.* **2016**, *138*, 2809–2814.

(39) Lackinger, M. Surface-assisted Ullmann coupling. *Chem. Commun.* **2017**, *53*, 7872–7885.

(40) Giannakakis, G.; Flytzani-Stephanopoulos, M.; Sykes, E. C. H. Single-Atom Alloys as a Reductionist Approach to the Rational Design of Heterogeneous Catalysts. *Acc. Chem. Res.* **2019**, *52*, 237–247.

(41) Mitchell, S.; Pérez-Ramírez, J. Single atom catalysis: a decade of stunning progress and the promise for a bright future. *Nat. Commun.* **2020**, *11*, 4302.

(42) Parkinson, G. S. Single-Atom Catalysis: How Structure Influences Catalytic Performance. *Catal. Lett.* **2019**, *149*, 1137–1146.

(43) Wang, A.; Li, J.; Zhang, T. Heterogeneous single-atom catalysis. *Nat. Rev. Chem.* **2018**, *2*, 65–81.

(44) Böhme, D. K.; Schwarz, H. Gas-Phase Catalysis by Atomic and Cluster Metal Ions: The Ultimate Single-Site Catalysts. *Angew. Chem., Int. Ed.* **2005**, *44*, 2336–2354.

(45) Zhong, D.; Franke, J.-H.; Podiyanachari, S. K.; Blömker, T.; Zhang, H.; Kehr, G.; Erker, G.; Fuchs, H.; Chi, L. Linear Alkane Polymerization on a Gold Surface. *Science* **2011**, *334*, 213–216.

(46) Lafferentz, L.; Eberhardt, V.; Dri, C.; Africh, C.; Comelli, G.; Esch, F.; Hecht, S.; Grill, L. Controlling on-surface polymerization by hierarchical and substrate-directed growth. *Nature Chem.* **2012**, *4*, 215–220.

(47) Blunt, M. O.; Russell, J. C.; Champness, N. R.; Beton, P. H. Templating molecular adsorption using a covalent organic framework. *Chem. Commun.* **2010**, *46*, 7157–7159.

(48) Zhang, H.; Franke, J.-H.; Zhong, D.; Li, Y.; Timmer, A.; Arado, O. D.; Mönig, H.; Wang, H.; Chi, L.; Wang, Z.; Müllen, K.; Fuchs, H. Surface Supported Gold—Organic Hybrids: On-Surface Synthesis and Surface Directed Orientation. *Small* **2014**, *10*, 1361–1368.

(49) Xing, S.; Zhang, Z.; Fei, X.; Zhao, W.; Zhang, R.; Lin, T.; Zhao, D.; Ju, H.; Xu, H.; Fan, J.; Zhu, J.; Ma, Y.-q.; Shi, Z. Selective on-surface covalent coupling based on metal-organic coordination template. *Nat. Commun.* **2019**, *10*, 70.

(50) Karan, S.; Geng, Y.; Decurtins, S.; Liu, S.-X.; Repp, J. Gold-linked strings of donor—acceptor dyads: on-surface formation and mutual orientation. *Chem. Commun.* **2020**, *56*, 7901–7904.

(51) Kumar, D.; Krull, C.; Yin, Y.; Medhekar, N. V.; Schiffrin, A. Electric Field Control of Molecular Charge State in a Single-Component 2D Organic Nanoarray. *ACS Nano* **2019**, *13*, 11882–11890.

(52) Pawin, G.; Wong, K. L.; Kim, D.; Sun, D.; Bartels, L.; Hong, S.; Rahman, T. S.; Carp, R.; Marsella, M. A Surface Coordination Network Based on Substrate-Derived Metal Adatoms with Local Charge Excess. *Angew. Chem., Int. Ed.* **2008**, *47*, 8442–8445.

(53) Zhang, J.; Shchyrba, A.; Nowakowska, S.; Meyer, E.; Jung, T. A.; Muntwiler, M. Probing the spatial and momentum distribution of confined surface states in a metal coordination network. *Chem. Commun.* **2014**, *50*, 12289–12292.

(54) Hernández-López, L.; Piquero-Zulaica, I.; Downing, C. A.; Piantek, M.; Fujii, J.; Serrate, D.; Ortega, J. E.; Bartolomé, F.; Lobo-Checa, J. Searching for kagome multi-bands and edge states in a predicted organic topological insulator. *Nanoscale* **2021**, *13*, 5216–5223.

(55) Kumar, D.; Hellerstedt, J.; Field, B.; Lowe, B.; Yin, Y.; Medhekar, N. V.; Schiffrin, A. Manifestation of Strongly Correlated Electrons in a 2D Kagome Metal—Organic Framework. *Adv. Funct. Mater.* **2021**, *31*, 2106474.

(56) Yan, L.; Silveira, O. J.; Alldritt, B.; Krejčí, O.; Foster, A. S.; Liljeroth, P. Synthesis and Local Probe Gating of a Monolayer Metal-Organic Framework. *Adv. Funct. Mater.* **2021**, *31*, 2100519.

(57) Yan, L.; Silveira, O. J.; Alldritt, B.; Kezilebieke, S.; Foster, A. S.; Liljeroth, P. Two-Dimensional Metal—Organic Framework on Superconducting NbSe2. *ACS Nano* **2021**, *15*, 17813–17819.

(58) Yan, L.; Pohjavirta, I.; Alldritt, B.; Liljeroth, P. On-Surface Assembly of Au-Dicyanoanthracene Coordination Structures on Au(111). *ChemPhysChem* **2019**, *20*, 2297–2300.

(59) Arras, E.; Seitsonen, A. P.; Klappenberger, F.; Barth, J. V. Nature of the attractive interaction between proton acceptors and organic ring systems. *Phys. Chem. Chem. Phys.* **2012**, *14*, 15995–16001.

(60) Zhang, X.; Xue, N.; Li, C.; Li, N.; Wang, H.; Kocić, N.; Beniwal, S.; Palotás, K.; Li, R.; Xue, Q.; Maier, S.; Hou, S.; Wang, Y. Coordination-Controlled C—C Coupling Products via ortho-Site C—H Activation. *ACS Nano* **2019**, *13*, 1385–1393.

(61) Pawlak, R.; Liu, X.; Ninova, S.; D'Astolfo, P.; Drechsel, C.; Sangtarash, S.; Häner, R.; Decurtins, S.; Sadeghi, H.; Lambert, C. J.; Aschauer, U.; Liu, S.-X.; Meyer, E. Bottom-up Synthesis of Nitrogen-Doped Porous Graphene Nanoribbons. *J. Am. Chem. Soc.* **2020**, *142*, 12568–12573.

(62) Li, Q.; Yang, B.; Björk, J.; Zhong, Q.; Ju, H.; Zhang, J.; Cao, N.; Shi, Z.; Zhang, H.; Ebeling, D.; Schirmeisen, A.; Zhu, J.; Chi, L. Hierarchical Dehydrogenation Reactions on a Copper Surface. *J. Am. Chem. Soc.* **2018**, *140*, 6076–6082.

(63) Fan, D.; Sakai, Y.; Chelikowsky, J. R. Chemical and steric effects in simulating noncontact atomic force microscopy images of organic molecules on a Cu (111) substrate. *Phys. Rev. Materials* **2020**, *4*, 053802.

(64) Kumagai, T.; Hanke, F.; Gawinkowski, S.; Sharp, J.; Kotsis, K.; Waluk, J.; Persson, M.; Grill, L. Controlling intramolecular hydrogen transfer in a porphycene molecule with single atoms or molecules located nearby. *Nature Chem.* **2014**, *6*, 41−46.

(65) Hapala, P.; Kichin, G.; Wagner, C.; Tautz, F. S.; Temirov, R.; Jelínek, P. Mechanism of high-resolution STM/AFM imaging with functionalized tips. *Phys. Rev. B* **2014**, *90*, 085421.

(66) Li, J.; Schneider, W.-D.; Berndt, R. Local density of states from spectroscopic scanning-tunneling-microscope images: Ag(111). *Phys. Rev. B* **1997**, *56*, 7656−7659.

(67) Liljeroth, P.; Swart, I.; Paavilainen, S.; Repp, J.; Meyer, G. Single-Molecule Synthesis and Characterization of Metal-Ligand Complexes by Low-Temperature STM. *Nano Lett.* **2010**, *10*, 2475−2479.

(68) Liu, X.; Matej, A.; Kratky, T.; Mendieta-Moreno, J. I.; Günther, S.; Mutombo, P.; Decurtins, S.; Aschauer, U.; Repp, J.; Jelinek, P.; Liu, S.-X.; Patera, L. L. Exploiting Cooperative Catalysis for the On-Surface Synthesis of Linear Heteroaromatic Polymers via Selective C−H Activation. *Angew. Chem., Int. Ed.* **2022**, *61*, No. e202112798.

(69) Sun, Q.; Zhang, C.; Kong, H.; Tan, Q.; Xu, W. On-surface aryl−aryl coupling via selective C−H activation. *Chem. Commun.* **2014**, *50*, 11825−11828.

(70) Liu, J.; Chen, Q.; He, Q.; Zhang, Y.; Fu, X.; Wang, Y.; Zhao, D.; Chen, W.; Xu, G. Q.; Wu, K. Bromine adatom promoted C−H bond activation in terminal alkynes at room temperature on Ag(111). *Phys. Chem. Chem. Phys.* **2018**, *20*, 11081−11088.

(71) Telychko, M.; Su, J.; Gallardo, A.; Gu, Y.; Mendieta-Moreno, J. I.; Qi, D.; Tadich, A.; Song, S.; Lyu, P.; Qiu, Z.; Fang, H.; Koh, M. J.; Wu, J.; Jelínek, P.; Lu, J. Strain-Induced Isomerization in One-Dimensional Metal−Organic Chains. *Angew. Chem., Int. Ed.* **2019**, *58*, 18591−18597.

(72) Han, D.; Tao, Z.; Wang, T.; Feng, L.; Li, X.; Zeng, Z.; Zhu, J. Sequential Activation of Aromatic C-H Bonds on Cu(111). *J. Phys. Chem. C* **2022**, *126*, 5541−5549.

(73) Zeng, Z.; Guo, D.; Wang, T.; Chen, Q.; Matěj, A.; Huang, J.; Han, D.; Xu, Q.; Zhao, A.; Jelínek, P.; de Oteyza, D. G.; McEwen, J.-S.; Zhu, J. Chemisorption-Induced Formation of Biphenylene Dimer on Ag(111). *J. Am. Chem. Soc.* **2022**, *144*, 723−732.

5. Conclusion

This thesis serves as a comprehensive presentation of the author's research on the topic of on-surface synthesis (OSS), with a specific focus on the theoretical investigation of reaction mechanisms. This work aims to highlight the author's unique findings and contributions to the field.

The thesis begins by introducing the methodology of OSS, and the integration of scanning probe microscopy techniques, which enable the manipulation and characterization of these surface reactions. Furthermore, the thesis provides an assessment of the achievements and limitations of OSS, offering insights into the current state of the field. Together with the background of theoretical chemistry methods including quantum and molecular mechanics, the selection of methodologies utilized in the research is presented, offering readers a deeper understanding of the computational tools and techniques employed. The author's results and contributions to the findings throughout his Ph.D. studies are highlighted by the selection of published articles in high-impact peer-reviewed journals.

The primary objective of the first project was to investigate the reaction mechanism of intrapolymeric cyclization in two chemically similar polymers. The focus was on understanding why this cyclization occurs only in one of the polymers, despite both having similar chemical properties. To unravel this mystery, the free energy profiles of various reaction pathways and individual reaction steps were analyzed. The initial analysis revealed that the reaction barriers alone do not determine which pathway the polymer will take. If one were to simply follow the path with the lowest reaction barrier, both polymers would form pentalene-bridged polymers. However, it was evident that other factors came into play. In considering the reaction rate at a constant temperature, it became apparent that the exponential prefactor, in addition to the activation energy, influences the reaction rate according to the Arrhenius equation. In ultra-high vacuum conditions, where the reaction occurs intramolecularly, the collision theory is not applicable. Instead, the prefactor provides information about the attempt frequency based on the vibrational modes of the molecule. To gain insights into these vibrational modes and their impact on the relevant atoms during the cyclization reaction step, vibrational calculations were performed. Significant differences were observed between the two polymers. The bisanthene polymer exhibited several vibration modes in which the relevant carbon atoms involved in forming new bonds vibrated in phase. Moreover, the overlap of these vibrations with the initial (IS) to transition state (TS) transition was remarkable. On the other hand, the anthracene polymer lacked these specific vibration modes. Although some vibrations of the relevant carbon atoms were present, the two carbons involved in bond formation vibrated out of phase, thus not contributing to the attempt frequency. The observed differences in vibrations were attributed to a change in π-conjugation between the two polymers. Therefore, while bisanthene would form the

pentalene linkers, anthracene undergoes two subsequential dehydrogenation steps, which ultimately lead through a distinct TS to defects, in agreement with experimental observations. This work showcases the importance of π-conjugation in the context of aromatic-quinoid transition in conjugated hydrocarbons, as it can unlock new reaction pathways.

The second research project in this thesis focused on investigating the role of sodium atoms in the formation of colinear polymers. Initially, experimental observations indicated that one-dimensional polymerization did not occur in the absence of sodium, as the HAT (hexaazatriphenylene) molecules desorbed at elevated temperatures. The goal of this project was to understand the underlying mechanisms that enable the formation of linear polymers in the presence of sodium. Calculations were conducted to explore the effect of sodium cations binding to HAT monomers, forming noncovalent organometallic dimers. These dimers exhibited stronger molecule-substrate interactions, which helped hold the molecules on the surface even at higher temperatures. The binding of HAT monomers to the sodium cations facilitated C-H cleavage, catalyzed by the Ag(111) surface native adatoms. This C-H cleavage step was essential for polymerization to occur. By performing calculations on the bond dissociation energies (BDEs) of the dimers, it was observed that the three inequivalent C-H positions displayed variations, with the BDE increasing as the C-H distance from the sodium cation increased. However, the calculated free energy profiles revealed that the second position had the lowest energy barrier. This finding indicated that polymerization would occur by formally appending further dimers to the growing chain. This mechanism elucidated the formation of two colinear polymers as observed experimentally. Furthermore, the coordinated sodium atom in each tetradentate coordination pocket of two HAT molecules played a crucial role in holding the polymers together. The presence of sodium facilitated the on-surface reaction and enabled the formation of linear polymers.

The third and final research project presented in this thesis focused on investigating the effect of codepositing gold adatoms on the Ag(111) surface. By depositing DCA (dicyanoanthracene) molecules on various coinage metals with native or deposited metallic adatoms, different self-assemblies of DCA were formed. In this particular study, the goal was to understand the regioselective activation of aromatic C-H bonds at room temperature and the formation of organometallic dimers by codepositing DCA with gold on a silver surface. Initially, calculations were performed to clarify the nature of the gold adatoms on the Ag(111) surface. The results revealed that the gold adatoms had low hybridization and exhibited atomic-like characteristics. Subsequent calculations on the DCA molecules, aimed at probing the regioselectivity of C-H dissociation, did not yield successful outcomes. To explore the possible reaction mechanism, the diffusion of free gold adatoms on the surface towards the edges of the DCA self-assembly was considered. It was observed that the interaction between the gold atom and the nitrogen atom positioned the gold close to the

targeted C-H bond within a noncovalently bound DCA dimer. Calculations of the transition state indicated a significant reduction in the activation energy of C-H dissociation in this complex. Further simulations of free energy profiles solidified these findings by demonstrating a reduction in the energy barrier to a mere 19 kcal/mol at room temperature. Importantly, this reaction step was found to be regiospecific. Other C-H dissociation barriers were higher due to factors such as steric hindrance, electrostatic repulsion, or a lack of interaction between the gold and nitrogen atoms. The key effect in reducing the barrier was the hybridization of gold's s and d orbitals, which mitigated repulsion with nitrogen. This research project showcased the promising potential of combining various metallic adatoms and surfaces in OSS protocols. Moreover, it demonstrated the significant effect of self-assembly and adatom interactions, resulting in regiospecific bond scission at room temperature. The findings of this study highlight the prospects for manipulating surface reactions through the controlled use of metallic adatoms and provide valuable insights for the design of novel OSS methodologies.

In summary, the author's Ph.D. studies encompassed multiple research projects focused on investigating reaction mechanisms in OSS protocols. These studies involved the application of various theoretical methods, allowing for direct comparisons with experimental findings. The author's research aimed to elucidate the key effects of OSS observed in SPM experiments and propose reaction mechanisms that explain the formation of specific products.

6. Závěr

Tato práce slouží jako ucelená prezentace autorova výzkumu na téma syntézy na povrchu (OSS) se zvláštním zaměřením na teoretické zkoumání reakčních mechanismů. Cílem této práce je vyzdvihnout autorovy jedinečné poznatky a přínosy v této oblasti.

Práce začíná představením metodologie OSS a integrací technik mikroskopie skenovací sondou, které umožňují manipulaci a charakterizaci těchto povrchových reakcí. Dále práce poskytuje hodnocení úspěchů a omezení OSS a nabízí pohled na současný stav oboru. Spolu s pozadím teoretických chemických metod včetně kvantové a molekulové mechaniky je představen výběr metodik využitých ve výzkumu, který čtenářům nabízí hlubší pochopení použitých výpočetních nástrojů a technik. Výsledky a přínos autora k poznatkům v průběhu jeho doktorského studia jsou zdůrazněny výběrem publikovaných článků ve vysoce impaktovaných recenzovaných časopisech.

Hlavním cílem prvního projektu bylo prozkoumat reakční mechanismus intrapolymerní cyklizace u dvou chemicky podobných polymerů. Důraz byl kladen na pochopení, proč k této cyklizaci dochází pouze v jednom z polymerů, přestože oba mají podobné chemické vlastnosti. K odhalení této záhady byly analyzovány profily volné energie různých reakčních drah a jednotlivých reakčních kroků. Počáteční analýza odhalila, že samotné reakční bariéry neurčují, kterou cestou se polymer vydá. Pokud bychom jednoduše sledovali cestu s nejnižší reakční bariérou, oba polymery by tvořily polymery s pentalenovým můstkem. Bylo však zřejmé, že do hry vstupují další faktory. Při zvažování rychlosti reakce při konstantní teplotě se ukázalo, že kromě aktivační energie ovlivňuje rychlost reakce podle Arrheniovy rovnice také exponenciální prefaktor. V podmínkách ultravysokého vakua, kde reakce probíhá intramolekulárně, se srážková teorie neuplatňuje. Místo toho poskytuje prefaktor informaci o frekvenci pokusu na základě vibračních módů molekuly. Aby bylo možné získat přehled o těchto vibračních módech a jejich vlivu na příslušné atomy během kroku cyklizační reakce, byly provedeny výpočty vibrací. Mezi oběma polymery byly pozorovány významné rozdíly. Polymer bisanthenu vykazoval několik vibračních módů, v nichž příslušné atomy uhlíku podílející se na tvorbě nových vazeb vibrovaly ve fázi. Navíc bylo pozorováno značné překrývání těchto vibrací s přechodem z počátečního (IS) do přechodného stavu (TS). Naproti tomu polymer anthracenu tyto specifické vibrační módy postrádal. Ačkoli některé vibrace příslušných atomů uhlíku byly přítomny, dva uhlíky zapojené do tvorby vazby vibrovaly mimo fázi, a nepřispívaly tak k frekvenci pokusu. Pozorované rozdíly ve vibracích byly připsány změně π-konjugace mezi oběma polymery. Zatímco by tedy bisanthen tvořil pentalenové vazby, anthracen prochází dvěma následnými dehydrogenačními kroky, které nakonec vedou přes odlišný TS k defektům, což je v souladu s experimentálními pozorováními. Tato práce ukazuje důležitost π-

konjugace v kontextu aromaticko-chinoidního přechodu v konjugovaných uhlovodících, protože může odemknout nové reakční cesty.

Druhý výzkumný projekt této práce se zaměřil na zkoumání úlohy atomů sodíku při tvorbě kolineárních polymerů. Zpočátku experimentální pozorování ukázala, že k jednorozměrné polymeraci nedochází v nepřítomnosti sodíku, protože molekuly HAT (hexaazatrifenylen) při zvýšené teplotě desorbují. Cílem tohoto projektu bylo pochopit základní mechanismy, které umožňují tvorbu lineárních polymerů v přítomnosti sodíku. Byly provedeny výpočty, které zkoumaly vliv sodíkových kationtů vázajících se na monomery HAT za vzniku nekovalentních organokovových dimerů. Tyto dimery vykazovaly silnější interakce mezi molekulami a substrátem, což pomáhalo udržet molekuly na povrchu i při vyšších teplotách. Vazba monomerů HAT na sodné kationty usnadnila štěpení C-H, které katalyzovaly nativní adatomy povrchu Ag(111). Tento krok štěpení C-H byl nezbytný pro průběh polymerace. Provedením výpočtů vazebných disociačních energií (BDE) dimerů bylo zjištěno, že tři neekvivalentní polohy C-H vykazují změny, přičemž BDE se zvyšují s rostoucí vzdáleností C-H od sodného kationtu. Vypočtené profily volné energie však ukázaly, že druhá poloha má nejnižší energetickou bariéru. Toto zjištění naznačuje, že polymerace probíhá formálním připojováním dalších dimerů k rostoucímu řetězci. Tento mechanismus objasnil vznik dvou kolineárních polymerů, jak bylo pozorováno experimentálně. Kromě toho hrál koordinovaný atom sodíku v každé tetradentátní koordinační kapse dvou molekul HAT klíčovou roli při udržování polymerů pohromadě. Přítomnost sodíku usnadnila reakci na povrchu a umožnila vznik lineárních polymerů.

Třetí a poslední výzkumný projekt prezentovaný v této práci se zaměřil na zkoumání vlivu kodepozice adatomů zlata na povrch Ag(111). Depozicí molekul DCA (dikyanoantracenu) na různé mincovní kovy s nativními nebo deponovanými kovovými adatomy byla vytvořena různá samouspořádání DCA. V této konkrétní studii bylo cílem pochopit regioselektivní aktivaci aromatických C-H vazeb při pokojové teplotě a tvorbu organokovových dimerů kodepozicí DCA se zlatem na povrch stříbra. Nejprve byly provedeny výpočty k objasnění povahy adatomů zlata na povrchu Ag(111). Výsledky ukázaly, že adatomy zlata mají nízkou hybridizaci a vykazují atomární vlastnosti. Následné výpočty na molekulách DCA, zaměřené na zkoumání regioselektivity disociace C-H, nepřinesly úspěšné výsledky. Pro zkoumání možného reakčního mechanismu byla zvažována difúze volných adatomů zlata na povrchu směrem k okrajům samouspořádání DCA. Bylo zjištěno, že interakce mezi atomem zlata a atomem dusíku umisťuje zlato do blízkosti cílové vazby C-H v nekovalentně vázaném dimeru DCA. Výpočty přechodového stavu ukázaly významné snížení aktivační energie disociace C-H v tomto komplexu. Následné simulace profilů volné energie potvrdily tato zjištění tím, že prokázaly snížení energetické bariéry na pouhých 19 kcal/mol při pokojové teplotě. Důležité je, že tento reakční krok je regiospecifický. Ostatní bariéry disociace C-

H byly vyšší v důsledku faktorů, jako jsou sterické bránění, elektrostatické odpuzování nebo nedostatek interakcí mezi atomy zlata a dusíku. Klíčovým efektem při snižování bariéry byla hybridizace *s* a *d* orbitalů zlata, která zmírnila odpuzování s dusíkem. Tento výzkumný projekt ukázal slibný potenciál kombinace různých kovových adatomů a povrchů v protokolech OSS. Navíc prokázal významný vliv samouspořádání a interakcí adatomů, což vedlo k regiospecifickému štěpení vazeb při pokojové teplotě. Výsledky této studie zdůrazňují vyhlídky na manipulaci s povrchovými reakcemi prostřednictvím řízeného použití kovových adatomů a poskytují cenné poznatky pro návrh nových metodik OSS.

Souhrnně lze říci, že doktorské studium autora zahrnovalo několik výzkumných projektů zaměřených na zkoumání reakčních mechanismů v protokolech OSS. Tyto studie zahrnovaly použití různých teoretických metod, což umožnilo přímé srovnání s experimentálními zjištěními. Cílem autorova výzkumu bylo objasnit klíčové efekty v OSS pozorované při SPM experimentech a navrhnout reakční mechanismy, které vysvětlují vznik konkrétních produktů.

7. Outlook

Looking forward, the research presented in this thesis opens up exciting possibilities for future studies in the field of on-surface synthesis. The findings and methodologies developed by the author provide a solid foundation for further investigations and advancements. Here are some potential avenues for future research:

1) Elucidating the role of other adatoms: Building upon the research investigating the effects of sodium and gold adatoms, future studies could explore the impact of other adatoms on surface reactions. Investigating different metallic species and their interactions with specific molecules could lead to the discovery of novel catalytic systems and reaction pathways.

2) Extending the scope of reactions: While the presented projects focused on specific reactions and systems, numerous other on-surface reactions remain to be explored. We can investigate a wider range of substrates, molecules, and adatoms to expand our understanding of the underlying mechanisms and expand the toolbox of on-surface synthesis.

3) Exploring new theoretical approaches: While the author employed various theoretical methods, including DFT and molecular mechanics, there is always room for further improvement and innovation. We can explore using advanced computational techniques, such as machine learning and post-HF, to tackle more complex systems and provide more accurate predictions.

4) Designing functional materials: The knowledge gained from understanding reaction mechanisms in on-surface synthesis can be applied to the design and synthesis of functional materials with tailored properties. By manipulating the reaction conditions, adatom interactions, and molecular structures, we can aim to achieve specific functionalities and properties in surface-confined materials, leading to applications in areas such as electronics, catalysis, and energy storage.

In conclusion, the research presented in this thesis represents a significant contribution to the field of on-surface synthesis. The author's findings, published in high-impact scientific journals, demonstrate the quality and importance of the research conducted. The outlined outlook provides a roadmap for future investigations, enabling further advancements and breakthroughs in on-surface synthesis and its applications.

8. References

1. Stuyver, T. *et al.* Enhancing the conductivity of molecular electronic devices. *J. Chem. Phys.* **146**, 092310 (2016).

2. Müllen, K. & Rabe, J. P. Nanographenes as Active Components of Single-Molecule Electronics and How a Scanning Tunneling Microscope Puts Them To Work. *Acc. Chem. Res.* **41**, 511–520 (2008).

3. Shen, Y. & Chen, C.-F. Helicenes: Synthesis and Applications. *Chem. Rev.* **112**, 1463–1535 (2012).

4. Chen, W., Yu, F., Xu, Q., Zhou, G. & Zhang, Q. Recent Progress in High Linearly Fused Polycyclic Conjugated Hydrocarbons (PCHs, n > 6) with Well-Defined Structures. *Adv. Sci.* **7**, 1903766 (2020).

5. Zhang, L. *et al.* Unconventional, Chemically Stable, and Soluble Two-Dimensional Angular Polycyclic Aromatic Hydrocarbons: From Molecular Design to Device Applications. *Acc. Chem. Res.* **48**, 500–509 (2015).

6. Facchetti, A. π-Conjugated Polymers for Organic Electronics and Photovoltaic Cell Applications. *Chem. Mater.* **23**, 733–758 (2011).

7. González-Herrero, H. *et al.* Atomic Scale Control and Visualization of Topological Quantum Phase Transition in π-Conjugated Polymers Driven by Their Length. *Adv. Mater.* **33**, 2104495 (2021).

8. Kertesz, M., Choi, C. H. & Yang, S. Conjugated Polymers and Aromaticity. *Chem. Rev.* **105**, 3448–3481 (2005).

9. Rizzo, D. J. *et al.* Topological band engineering of graphene nanoribbons. *Nature* **560**, 204–208 (2018).

10. Sun, Z., Zeng, Z. & Wu, J. Zethrenes, Extended p-Quinodimethanes, and Periacenes with a Singlet Biradical Ground State. *Acc. Chem. Res.* **47**, 2582–2591 (2014).

11. Abe, M. Diradicals. *Chem. Rev.* **113**, 7011–7088 (2013).

12. Pavliček, N. *et al.* Synthesis and characterization of triangulene. *Nat. Nanotechnol.* **12**, 308–311 (2017).

13. Grill, L. *et al.* Nano-architectures by covalent assembly of molecular building blocks. *Nat. Nanotechnol.* **2**, 687–691 (2007).

14. Narita, A., Wang, X.-Y., Feng, X. & Müllen, K. New advances in nanographene chemistry. *Chem. Soc. Rev.* **44**, 6616–6643 (2015).

15. Ashworth, C. Super on-surface synthesis. *Nat. Rev. Chem.* **6**, 241–241 (2022).

16. Sánchez-Grande, A. *et al.* On-Surface Synthesis of Ethynylene-Bridged Anthracene Polymers. *Angew. Chem. Int. Ed.* **58**, 6559–6563 (2019).

17. Biswas, K. *et al.* On-surface synthesis of doubly-linked one-dimensional pentacene ladder polymers. *Chem. Commun.* **56**, 15309–15312 (2020).

18. Di Giovannantonio, M. & Fasel, R. On-surface synthesis and atomic scale characterization of unprotected indenofluorene polymers. *J. Polym. Sci.* **60**, 1814–1826 (2022).

19. Lawrence, J. *et al.* Circumventing the stability problems of graphene nanoribbon zigzag edges. *Nat. Chem.* **14**, 1451–1458 (2022).

20. Merino-Díez, N. *et al.* Width-Dependent Band Gap in Armchair Graphene Nanoribbons Reveals Fermi Level Pinning on Au(111). *ACS Nano* **11**, 11661–11668 (2017).

21. Barrena, E., de Oteyza, D. G., Dosch, H. & Wakayama, Y. 2D Supramolecular Self-Assembly of Binary Organic Monolayers. *ChemPhysChem* **8**, 1915–1918 (2007).

22. Wang, Q. H. & Hersam, M. C. Room-temperature molecular-resolution characterization of self-assembled organic monolayers on epitaxial graphene. *Nat. Chem.* **1**, 206–211 (2009).

23. Binnig, G., Rohrer, H., Gerber, Ch. & Weibel, E. Surface Studies by Scanning Tunneling Microscopy. *Phys. Rev. Lett.* **49**, 57–61 (1982).

24. Jelínek, P. High resolution SPM imaging of organic molecules with functionalized tips. *J. Phys. Condens. Matter* **29**, 343002 (2017).

25. Gross, L., Mohn, F., Moll, N., Liljeroth, P. & Meyer, G. The Chemical Structure of a Molecule Resolved by Atomic Force Microscopy. *Science* **325**, 1110–1114 (2009).

26. Gross, L. Recent advances in submolecular resolution with scanning probe microscopy. *Nat. Chem.* **3**, 273–278 (2011).

27. Temirov, R., Soubatch, S., Neucheva, O., Lassise, A. C. & Tautz, F. S. A novel method achieving ultra-high geometrical resolution in scanning tunnelling microscopy. *New J. Phys.* **10**, 053012 (2008).

28. Hapala, P. *et al.* Mechanism of high-resolution STM/AFM imaging with functionalized tips. *Phys. Rev. B* **90**, 085421–085421 (2014).

29. Krejčí, O., Hapala, P., Ondráček, M. & Jelínek, P. Principles and simulations of high-resolution STM imaging with a flexible tip apex. *Phys. Rev. B* **95**, 045407–045407 (2017).

30. Hohenberg, P. & Kohn, W. Inhomogeneous Electron Gas. *Phys. Rev.* **136**, B864–B871 (1964).

31. Koch, W. & Holthausen, M. C. *A Chemist ' s Guide to Density Functional Theory*. vol. 3 306 (2001).

32. Sholl, D. S. & Steckel, J. A. Density Functional Theory: A Practical Introduction. *Am. J. Phys.* **68**, 69–69 (2009).

33. Kohn, W. & Sham, L. J. Self-Consistent Equations Including Exchange and Correlation Effects. *Phys. Rev.* **140**, A1133–A1138 (1965).

34. Parr, R. G. & Young, W. Density-functional theory of atoms and molecules. *Int. J. Quantum Chem.* **47**, (1993).

35. Perdew, J. P., Burke, K. & Ernzerhof, M. Generalized Gradient Approximation Made Simple. *Phys. Rev. Lett.* **77**, 3865–3868 (1996).

36. Becke, A. D. A new mixing of Hartree–Fock and local density-functional theories. *J. Chem. Phys.* **98**, 1372–1377 (1993).

37. Becke, A. D. Density-functional thermochemistry. III. The role of exact exchange. *J. Chem. Phys.* **98**, 5648–5652 (1993).

38. Jacquemin, D., Wathelet, V., Perpète, E. A. & Adamo, C. Extensive TD-DFT Benchmark: Singlet-Excited States of Organic Molecules. *J. Chem. Theory Comput.* **5**, 2420–2435 (2009).

39. Weintraub, E., Henderson, T. M. & Scuseria, G. E. Long-Range-Corrected Hybrids Based on a New Model Exchange Hole. *J. Chem. Theory Comput.* **5**, 754–762 (2009).

40. Iikura, H., Tsuneda, T., Yanai, T. & Hirao, K. A long-range correction scheme for generalized-gradient-approximation exchange functionals. *J. Chem. Phys.* **115**, 3540–3544 (2001).

41. Wang, J., Wolf, R. M., Caldwell, J. W., Kollman, P. A. & Case, D. A. Development and testing of a general amber force field. *J. Comput. Chem.* **25**, 1157–1174 (2004).

42. Warshel, A. & Levitt, M. Theoretical studies of enzymic reactions: Dielectric, electrostatic and steric stabilization of the carbonium ion in the reaction of lysozyme. *J. Mol. Biol.* **103**, 227–249 (1976).

43. Yamaguchi, K. *Self-Consistent Field: Theory and Applications.* 727 (Elsevier: Amsterdam, 1990).

44. Grimme, S. & Hansen, A. A Practicable Real-Space Measure and Visualization of Static Electron-Correlation Effects. *Angew. Chem. Int. Ed.* **54**, 12308–12313 (2015).

45. Kumar, S., Rosenberg, J. M., Bouzida, D., Swendsen, R. H. & Kollman, P. A. THE weighted histogram analysis method for free-energy calculations on biomolecules. I. The method. *J. Comput. Chem.* **13**, 1011–1021 (1992).

46. Kumar, S., Rosenberg, J. M., Bouzida, D., Swendsen, R. H. & Kollman, P. A. Multidimensional free-energy calculations using the weighted histogram analysis method. *J. Comput. Chem.* **16**, 1339–1350 (1995).

47. Case, D. A. *et al.* Amber20. (2021).

48. Frisch, M. J. *et al.* Gaussian16 Revision C.01. (2016).

49. Lewis, J. P. *et al.* Advances and applications in the FIREBALL ab initio tight-binding molecular-dynamics formalism. *Phys. Status Solidi B* **248**, 1989–2007 (2011).

50. Dapprich, S., Komáromi, I., Byun, K. S., Morokuma, K. & Frisch, M. J. A new ONIOM implementation in Gaussian98. Part I. The calculation of energies, gradients, vibrational frequencies and electric field derivatives1Dedicated to Professor Keiji Morokuma in celebration of his 65th birthday.1. *J. Mol. Struct. THEOCHEM* **461–462**, 1–21 (1999).

51. Heinz, H., Lin, T.-J., Kishore Mishra, R. & Emami, F. S. Thermodynamically Consistent Force Fields for the Assembly of Inorganic, Organic, and Biological Nanostructures: The INTERFACE Force Field. *Langmuir* **29**, 1754–1765 (2013).

52. Chai, J.-D. & Head-Gordon, M. Long-range corrected hybrid density functionals with damped atom–atom dispersion corrections. *Phys. Chem. Chem. Phys.* **10**, 6615–6615 (2008).

53. Weigend, F. & Ahlrichs, R. Balanced basis sets of split valence, triple zeta valence and quadruple zeta valence quality for H to Rn: Design and assessment of accuracy. *Phys. Chem. Chem. Phys.* **7**, 3297–3305 (2005).

54. Hellweg, A., Hättig, C., Höfener, S. & Klopper, W. Optimized accurate auxiliary basis sets for RI-MP2 and RI-CC2 calculations for the atoms Rb to Rn. *Theor. Chem. Acc.* **117**, 587–597 (2007).

55. Lee, C., Yang, W. & Parr, R. G. Development of the Colle-Salvetti correlation-energy formula into a functional of the electron density. *Phys. Rev. B* **37**, 785–789 (1988).

56. Vosko, S. H., Wilk, L. & Nusair, M. Accurate spin-dependent electron liquid correlation energies for local spin density calculations: a critical analysis. *Can. J. Phys.* **58**, 1200–1211 (1980).

57. Adamo, C. & Barone, V. Toward reliable density functional methods without adjustable parameters: The PBE0 model. *J. Chem. Phys.* **110**, 6158–6170 (1999).

58. Neese, F. The ORCA program system. *WIREs Comput. Mol. Sci.* **2**, 73–78 (2012).

59. Neese, F. Software update: the ORCA program system, version 4.0. *WIREs Comput. Mol. Sci.* **8**, (2018).

60. Clair, S. & de Oteyza, D. G. Controlling a Chemical Coupling Reaction on a Surface: Tools and Strategies for On-Surface Synthesis. *Chem. Rev.* **119**, 4717–4776 (2019).

61. Shen, Q., Gao, H.-Y. & Fuchs, H. Frontiers of on-surface synthesis: From principles to applications. *Nano Today* **13**, 77–96 (2017).

62. Biswas, K. *et al.* Steering Large Magnetic Exchange Coupling in Nanographenes near the Closed-Shell to Open-Shell Transition. *J. Am. Chem. Soc.* **145**, 2968–2974 (2023).

63. Mishra, S. *et al.* Large magnetic exchange coupling in rhombus-shaped nanographenes with zigzag periphery. *Nat. Chem.* **13**, 581–586 (2021).

64. Mishra, S. *et al.* Synthesis and Characterization of π-Extended Triangulene. *J. Am. Chem. Soc.* **141**, 10621–10625 (2019).

65. Mishra, S. *et al.* Topological frustration induces unconventional magnetism in a nanographene. *Nat. Nanotechnol.* **15**, 22–28 (2020).

66. Mishra, S. *et al.* Nonbenzenoid High-Spin Polycyclic Hydrocarbons Generated by Atom Manipulation. *ACS Nano* **16**, 3264–3271 (2022).

67. Biswas, K. *et al.* Synthesis and Characterization of peri-Heptacene on a Metallic Surface. *Angew. Chem. Int. Ed.* **61**, e202114983 (2022).

68. Mendieta-Moreno, J. I. *et al.* Unusual Scaffold Rearrangement in Polyaromatic Hydrocarbons Driven by Concerted Action of Single Gold Atoms on a Gold Surface. *Angew. Chem. Int. Ed.* **61**, (2022).

69. Zhang, Z., Perepichka, D. F. & Khaliullin, R. Z. Adatoms in the Surface-Confined Ullmann Coupling of Phenyl Groups. *J. Phys. Chem. Lett.* **12**, 11061–11069 (2021).

70. Held, P. A. *et al.* On-Surface Domino Reactions: Glaser Coupling and Dehydrogenative Coupling of a Biscarboxylic Acid To Form Polymeric Bisacylperoxides. *Angew. Chem. Int. Ed.* **55**, 9777–9782 (2016).

71. Kalashnyk, N. *et al.* The Orientation of Silver Surfaces Drives the Reactivity and the Selectivity in Homo-Coupling Reactions. *ChemPhysChem* **19**, 1802–1808 (2018).

72. Cirera, B. *et al.* Tailoring topological order and π-conjugation to engineer quasi-metallic polymers. *Nat. Nanotechnol.* **15**, 437–443 (2020).

73. Stetsovych, O. *et al.* From helical to planar chirality by on-surface chemistry. *Nat. Chem.* **9**, 213–218 (2017).

74. Wäckerlin, C. *et al.* On-Surface Hydrogenation of Buckybowls: From Curved Aromatic Molecules to Planar Non-Kekulé Aromatic Hydrocarbons. *ACS Nano* **14**, 16735–16742 (2020).

75. Irziqat, B. *et al.* Stereospecific on-Surface Cyclodehydrogenation of Bishelicenes: Preservation of Handedness from Helical to Planar Chirality. *Chem. – Eur. J.* **27**, 13523–13526 (2021).

76. Voigt, J. *et al.* Unbalanced 2D Chiral Crystallization of Pentahelicene Propellers and Their Planarization into Nanographenes. *Chem. – Eur. J.* **27**, 10251–10254 (2021).

77. Mishra, S. *et al.* Observation of fractional edge excitations in nanographene spin chains. *Nature* **598**, 287–292 (2021).

78. Cai, J. *et al.* Atomically precise bottom-up fabrication of graphene nanoribbons. *Nature* **466**, 470–473 (2010).

79. de Oteyza, D. G. *et al.* Substrate-Independent Growth of Atomically Precise Chiral Graphene Nanoribbons. *ACS Nano* **10**, 9000–9008 (2016).

80. Mielke, J., Martínez-Blanco, J., Peters, M. V., Hecht, S. & Grill, L. Observing single-atom diffusion at a molecule-metal interface. *Phys. Rev. B* **94**, 035416 (2016).

81. Björk, J. *et al.* The Role of Metal Adatoms in a Surface-Assisted Cyclodehydrogenation Reaction on a Gold Surface. *Angew. Chem.* **134**, e202212354 (2022).

82. Zhang, J. *et al.* Probing the spatial and momentum distribution of confined surface states in a metal coordination network. *Chem. Commun.* **50**, 12289–12292 (2014).

83. Pawin, G. *et al.* A Surface Coordination Network Based on Substrate-Derived Metal Adatoms with Local Charge Excess. *Angew. Chem. Int. Ed.* **47**, 8442–8445 (2008).

84. Yan, L., Pohjavirta, I., Alldritt, B. & Liljeroth, P. On-Surface Assembly of Au-Dicyanoanthracene Coordination Structures on Au(111). *ChemPhysChem* **20**, 2297–2300 (2019).

About the Author

EDUCATION:

2019-present	Ph.D. in Nanomaterial Chemistry at the Department of Physical Chemistry, Palacký University Olomouc; supervisor Doc. Ing. Pavel Jelínek, Ph.D.
2016-2019	Mgr. Physical chemistry at the Department of Physical Chemistry, Palacký University Olomouc (Master's thesis: Structure and electronic properties at the α-Fe_2O_3/Pt interface; supervisor Piotr Blonski, Ph.D.)
2013-2016	Bc. Nanomaterial chemistry at the Department of Physical Chemistry, Palacký University Olomouc (Bachelor's thesis: Adsorption of Biomolecules on Graphene and Fluorinated Graphenes; supervisor Mgr. František Karlický, Ph.D.)

INTERNSHIPS & TRAINING:

2022(Sep-Dec)	3-month research internship with Prof. Hans Lischka, TTU, Lubbock, TX, USA
2021(Sep)	Light-Surface-Polymerization workshop, Karl Franzens Universität Graz
2019(Sep)	2-week stay at the University of Alicante, prof. Juan-Carlos Sancho-Garcia
2018(Feb & Oct)	Lectures on "Optical Spectroscopy of Conjugated Organic Materials", Tübingen, given by Dr. Johannes Gierschner
2016(Sep)-2017(Jun)	Université de Mons, Belgium, group of Dr. David Beljonne
2016(Jan)	PRACE Winter School 2016, AV SR, Bratislava, Slovakia

CONFERENCES

2022-Poster	WATOC2022 3-9th July. Poster title: *"Theoretical description of topologically protected high-spin arrangements in non-benzenoid polycyclic hydrocarbons"*.
2021-Presentation	ICN+T conference (online) 12-15th July. Presentation title: *"Tailoring π-conjugation and vibrational modes to steer on-surface synthesis of pentalene-bridged ladder polymers"*.
2021-Poster	DPG Spring meeting, Surface Science (online) 1-4th March. Poster title: *"Theoretical analysis of chemical transformation of π-conjugated polymers steered by internal vibrational modes"*.
2020-Presentation	Workshop on Low Dimensional Materials 8-11th September, Liblice. Presentation title: *"Tailoring π-conjugation and vibrational modes to steer on-surface synthesis of pentalene-bridged ladder polymers"*.
2020-Poster	Computing π-Conjugated Compounds symposium 30th January – 1st February, Zagreb, Croatia. Poster title: *"Tailoring π-conjugation and*

vibrational modes to steer on-surface synthesis of pentalene-bridged ladder polymers".

2015-Poster   Nanocon conference 14-16th October, Brno. Poster title: *"The Adsorption of Biomolecules on Graphene and Fluorinated Graphenes"*.

RESEARCH FOCUS

He is skilled in a wide range of theoretical methods allowing for a complex and accurate description of the studied problem. Density functional theory (DFT) methods allow for fast and reliable relaxation of medium-sized systems together with the description of electronic structure and molecular properties. His skills in analyzing the ground state electronic structure of polycyclic aromatic hydrocarbons (PAHs) together with searching for reaction mechanisms resulted in several manuscripts published in high-impact peer-reviewed journals. In the domain of on-surface synthesis, he acquired the QM/MM methodology combining DFT with molecular mechanics and molecular dynamics to obtain precise free energy profiles along the studied reactions. In PAHs, one of the key information is the resulting π-conjugation and aromaticity in the prepared molecules. For this reason, he employs several techniques for analyzing aromaticity and conjugation.

In the rapidly progressing field of synthesis of open-shell PAHs, classical DFT methods often fail to describe the highly correlated electrons in such molecules and therefore he expands his portfolio of computational methods to ab-initio many-body calculations for multireference systems. These include for example complete active space self-consistent field (CASSCF) with further corrections for dynamic correlation.

Overall, he combines methodologies of various accuracy and speed for the proper description of the studied problem. For a direct connection with experiments and justification of the used theory, he acquired methods of calculating experimental images from the theoretical models. This approach has proven to be beneficial for model justification and explanation of observed properties.

TEACHING ACTIVITIES

During his Ph.D., he participated in departmental teaching activities, leading laboratory techniques and chemical seminars. Since November 2022, he supervises a bachelor's thesis studying molecules on solid surfaces.